Performance Assessment of Low Ductility Reinforced Concrete Shear Walls Retrofitted by Carbon Fiber Sheets under Cyclic Loading

（炭素繊維で補強された低靭性鉄筋コンクリート造耐震壁の繰り返し載荷における性能評価）

July, 2016

Doctor of Engineering

Roy Ericksen REYNA SALAZAR

Toyohashi University of Technology

DEDICATION

I dedicate this thesis to my parents Baldomero and Elizabeth as well as to my beloved little brother Josue for encouraging me all the time. I hope this achievement will fill you with happiness as well as I am.

ACKNOWLEDGMENT

I would like to express my deepest gratitude to my academic supervisor, Professor Taiki Saito, for his enthusiastic guidance, valuable suggestions, constructive criticism, friendly discussions and persistent supervision, which were indispensable for completion of this dissertation. Also, I would like to express my sincere gratitude to Associate Professor Tomoya Matsui and Assistant Professor Kazuhiro Hayashi for their kind support and collaboration during the experimental tests.

Sincere thanks to the Japan Science Technology Agency (JST) through the Science and Technology Research Partnership for Sustainable Development (SATREPS) for providing me the Monbukagakusho scholarship.

I will always be grateful to Professor Carlos Zavala and Professor Miguel Estrada from National University of Engineering in Peru for their support and trust during these years.

Last but not least, to the students of Toyohashi University of Technology, Uchimura K., Kawai H. and Sakai T. for their valuable support during the experimental test, as well as to the members of Saito-Matsui Lab.

ABSTRACT

Earthquakes are caused by a sudden release of energy from the movement between tectonic plates; besides geological faults and volcanism. As Peru is located in a high seismic hazard zone, it is necessary to improve the seismic response of buildings against earthquakes. In addition, in recent years, large scale construction of medium-rise building that use low ductility reinforced concrete (LDRC) walls has become commonplace in Peru. These walls do not have boundary columns but instead have a small quantity of reinforcing bars at each end and therefore expected to fail in flexural mode.

LDRC walls do not have a large deformation capacity in comparison with conventional RC walls, whereby, to improve seismic response of buildings composed by LDRC walls against earthquakes, might be possible by increasing its deformation capacity through carbon fiber sheet (CFS) confinement method.

Two verification tests were conducted by using CFS as a retrofitting method in Toyohashi University of Technology (TUT), Japan. The first test was conducted over three LDRC walls (Without CFS, full wall retrofitted with CFS and edges retrofitted with CFS). The second test was conducted over another three similar walls following the same retrofitted pattern of the first experiment but with a partial height retrofitted with CFS. From those tests, it was verified that carbon fiber sheets delay the concrete crushing of the wall base that occurs during flexural failure and that deformation performance was improved.

To verify the confinement effect of CFS, a third experiment was conducted using concrete samples with CFS by changing the size, shape and number of CFS layers. In total, 39 concrete samples (Circular shape: 8-ϕ150x300mm, Square shape: 9-150x150x300mm, 2-150x150x450mm, Rectangular shape: 4-150x300x300mm, 2-150x300x450mm, 5-100x300x200mm, 2-100x300x300mm, 5-100x400x200mm, 2-100x400x300mm) were tested under compressive loading (monotonic and cyclic). From the experiment, it was confirmed that deformation performance was improved and the strength of the concrete was increased due to the confinement provided by the CFS. However the stress-strain relationship of concrete with CFS depends on the geometry of the concrete sample.

A model of stress-strain relationship of concrete with or without CFS confinement was proposed and compared with the experimental results. The proposed model for the stress-strain relationship of unconfined concrete under cyclic loading is based on Darwin & Pecknold's

model, Noguchi's model, Naganuma's model, Lam & Teng's model and Nakatsuka's model. This model takes into consideration three linear functions after reaching the maximum strength of the concrete. Besides, this model considers the plastic strain deformation during the unloading path and the inner loop during the compressive stage.

Regarding to the monotonic stress-strain relationship of concrete with CFS confinement, the proposed model is based on Nakatsuka's model which has two linear functions after reaching B-point up to the rupture of the CFS. Considering the influence of the parameters which affects the stress-strain relationship of the concrete confined with CFS, such as sample shape, aspect ratio and effective confinement ratio of the section, modified Nakatsuka's model is introduced for the monotonic stress-strain relationship of concrete with CFS confinement.

For the cyclic hysteresis rules of concrete with CFS confinement, the proposed model for unconfined concrete was used by using the monotonic stress-strain relationship of concrete with CFS confinement, and following the same rules to generate the hysteresis loops. By using the proposed model, a uniaxial test simulation over the samples of the third experiment was conducted in order to validate the model. Both, monotonic and cyclic simulations gave a good match with the experimental results.

A software of Finite Element Method, STERA_FEM, was developed taking consideration: 4 nodes isoparametric planar element, incompatible element, 9 Gaussian points, the proposed model for concrete with or without CFS confinement, equivalent uniaxial strain of concrete for each principal direction considering the bi-axial stress-strain relationship of concrete by using the maximum stress surface of concrete, smeared crack model with the Menegotto-Pinto hysteresis model for reinforcing steel and an elastic-brittle model for CFS.

Finally, a pushover analysis were conducted and compared with the experimental results of the six walls (retrofitted with CFS and non-retrofitted).

Further studies on the shape coefficients for circular, square and rectangular shaped are suggested to improve the non-linear hysteresis of concrete retrofitted with CFS, by increasing the data with a large range of concrete types, using different amount of CFS as a confinement method and considering the effective confinement ratio of the section.

TABLE OF CONTENTS

LIST OF TABLES

LIST OF FIGURES

CHAPTER 1

INTRODUCTION

CHAPTER 1 : INTRODUCTION

1.1 General background

Earthquakes are caused by a sudden release of energy from the movement between tectonic plates; besides geological faults and volcanism. As Peru is located in a high seismic hazard zone, it is necessary to improve the seismic response of buildings against earthquakes. In addition, in recent years, large scale construction of medium-rise building that use low ductility reinforced concrete (LDRC) wall has become commonplace in Peru, with rectangular cross-sections, reinforced with wire mesh and additionally vertical reinforcing bars at boundary ends [43]. These walls do not have boundary columns but instead have a small quantity of reinforcing bars at each end and therefore expected to fail in flexural mode.

It is well known that the capacity of any building to resist the seismic forces from a certain earthquake is due to the energy dissipation; this energy dissipation can be generated through inelastic deformations of the structure, which means a structural damage that is allowed by the structural design codes. The principle of the seismic-resistance design is to prevent the collapse of the structure after an earthquake but is allowed that the building may suffer some level of structural damage.

Recent experiences such as the Chile Earthquake occurred in February 27, 2010 with moment magnitude M_w 8.8 drew a huge uncertainty regarded to the response behavior of medium-rise buildings that use LDRC walls as is shown in Figure 1-1 and Figure 1-2.

Figure 1-1 Damage in a 13 story height building that use LDRC wall

Figure 1-2 Damage in a 22 story height residential building that use LDRC wall

Nowadays in Peru, many buildings have been constructed using LDRC wall, mainly for residential buildings as is illustrated in Figure 1-3.

Figure 1-3 Buildings in Peru that use LDRC wall

1.2 Problem statement

Buildings that use reinforced concrete (RC) walls, has a typical configuration which includes boundary columns, those walls may have one or two reinforcing steel layers over the wall span as is shown in Figure 1-4. On the other hand, buildings that use LDRC do not have boundary columns but instead have a small quantity of reinforcing bars at each end and therefore expected to fail in flexural mode; those walls may have one or two reinforcing steel layers over the wall span as well as is shown in Figure 1-5.

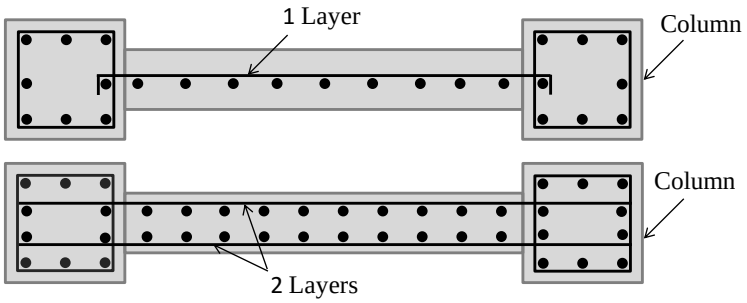

Figure 1-4 Typical RC wall

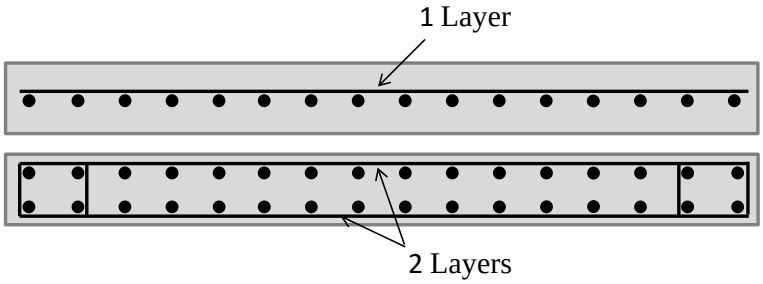

Figure 1-5 Typical RC wall

The expected behavior of RC walls and LDRC wall is shown in Figure 1-6. Where, RC walls are expected to have higher maximum strength and larger deformation capacity in comparison with LDRC wall. This expected behavior it is confirmed by several experimental reports. [20][21][43]

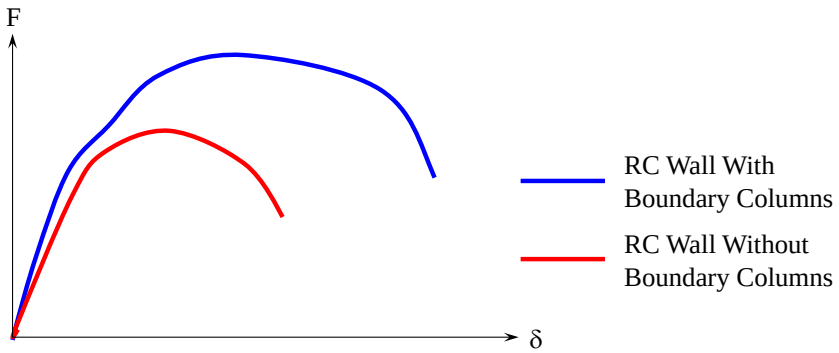

Figure 1-6 Typical RC wall

The earthquake force induced in the structure is transformed into elastic energy of movement and deformation, and energy dissipated. From the principle of the energy conservation, an energetic equilibrium between the input energy and the sum of elastic energy and dissipated energy must exist. At the same time, the elastic energy of the structure is composed of potential energy of elastic deformation and energy of movement.

On the other hand, the structure can dissipate energy through the damping of the structure and hysteretic energy. The damping of the structure is inherent to its structural characteristics, while the hysteretic energy is coming from inelastic deformations or structural damage that the structure suffers during the earthquake.

How to improve the response of buildings that use LDRC walls?. Taking into consideration that LDRC walls may fail in flexural mode. Therefore, by increasing its deformation capacity will improve its hysteretic energy dissipation. However, how to improve the deformation capacity of LDRC wall that already exist?. This investigation will focus on the retrofitting method by using CFS.

1.3 Objective and scope of the study

1.3.1 Objectives of the study

The overall goals of this investigation are outlined as follow:

1. To assess the performance of low ductility reinforced concrete walls retrofitted with carbon fiber sheet under cyclic loading.
2. To propose a formulation to predict the non-linear response of concrete under cyclic loading.
3. To develop a non-linear finite element software to model the behavior of reinforced concrete under cyclic loading.

The objectives of this study are drawn below:

1. To verify the deformation capacity improvement of low ductility reinforced concrete walls retrofitted with carbon fiber sheet.
2. To investigate the confinement effect of concrete with carbon fiber sheet reinforcement.
3. To develop a non-linear stress-strain relationship for concrete with or without carbon fiber sheet reinforcement.
4. To implement a non-linear finite element software with the proposed model.
5. To validate the proposed models by comparing the experimental result with the proposed model.

1.3.2 Scope of the study

Deformation capacity of LDRC walls under cyclic loading can be improved by using different types of retrofitting methods, such us using carbon fiber sheet to confine the concrete section of the wall. The effectiveness of the retrofitting depends on the retrofitting method used, and this investigation will focus in the retrofitting with carbon fiber sheet. Two ways of retrofitting with carbon fiber sheet are used.

Since medium-rise building that use LDRC walls my fail in flexural mode, the retrofitting method applied is expected to improve the deformation capacity, while the maximum strength should not be affected.

A model of stress-strain relationship of concrete with or without CFS confinement is proposed and compared with the experimental results. Parameters which affect the stress-strain relationship are discussed, such as: sample shape, confinement ratio, etc. Then, the software of Finite Element Method, STERA_FEM, was developed adapting this new model. STERA_FEM takes into consideration: four nodes isoparametric elements, 9 Gaussian points, incompatible element, the modified Darwin and Pecknold hysteresis model for reinforced concrete including confinement effect of CFS, smeared model and Menegotto-Pinto hysteresis model for reinforcing steel; and an elastic-brittle model for CFS. The analysis of the wall specimen in the first and second experiments was conducted using STERA_FEM and compared with test results.

1.4 Outline of the dissertation

The dissertation is organized in eight chapters. Some statements of the expected performance of LDRC walls and problems related to its behavior are described in the present chapter. Besides, objectives, scope and outline of this study are listed in the current chapter. The rest of the chapters are outlined as follow:

Chapter 2: Literature review. This chapter presents the theoretical background of the material components of the LDRC wall retrofitted with CFS, such as concrete, reinforcing steel and carbon fiber sheet. Besides, this chapter reviews researches about the stress-strain relationship for concrete, reinforcing steel and carbon fiber sheet.

Chapter 3: Finite element method – Elastic theory. This chapter summarized the elastic theory of the finite element method used in this study. Important definitions are presented in this chapter such us: Interpolation function, Gaussian quadrature rule, Isoparametric element, Stress and strain at Gaussian points and Incompatible element.

Chapter 4: Experimental tests. This chapter summarizes the three experiments conducted: LDRC wall retrofitted with full height of CFS under cyclic loading, LDRC wall retrofitted with partial height of CFS under cyclic loading and confinement effect of concrete with CFS reinforcement as a retrofitting method under monotonic and cyclic loading.

Chapter 5: Monotonic stress-strain relationship of concrete with CFS confinement. This chapter review researches about the monotonic stress-strain relationship of concrete with carbon fiber sheet confinement under compressive loading by comparing with the experimental result presented in the previous chapter. Besides, a modified Nakatsuka's model is presented in this study by changing its shape coefficients.

Chapter 6: Stress-strain relationship of concrete with or without CFS confinement under cyclic loading. A proposed stress-strain relationship for concrete with or without CFS confinement is presented in this study; this model is based on Darwin & Pecknold, Noguchi, Naganuma and Lam & Teng's model. Moreover a comparison with experimental results presented in the Chapter 4 is carried out.

Chapter 7: Nonlinear finite element analysis. This chapter presents the theoretical formulation to conduct a non-linear finite element analysis of reinforced concrete based in the formulation presented in Chapter 3, taking into account a four nodes isoparametric element, incompatible element and nine Gaussian points. Besides, biaxial stress-strain relationship of concrete is considered. This chapter also shows the comparison of experimental wall presented in Chapter 4 and nonlinear finite element analysis.

Chapter 8: Conclusions and Recommendations. This chapter provides some conclusions from the experimental and the analytical results obtained in this research, and some recommendation for further researches.

CHAPTER 2

LITERATURE REVIEWED

CHAPTER 2 : LITERATURE REVIEW

2.1 Material overview

2.1.1 Concrete

Reinforce concrete is the major medium of construction throughout the world. While in service, reinforce concrete structures are subjected to many cycles of load. In case of structures located in seismic zones, whereby subjected to seismic loads, the cycles may be of large magnitude. [9]

Cervanka [6] and Yuzugullu & Schnobrich [42] conducted several test on reinforce concrete elements such as shear walls, shear panels and flexural member; they modeled those elements as elasto-plastic materials. From the experimental test, it was determined that the steel remains elastic and the concrete behaves as an elastic-brittle material. Hence the concrete behaves in a highly nonlinear manner in uniaxial compression, but in uniaxial tension can be idealized as a linear, elastic and brittle material. (See Figure 2-1) [9]

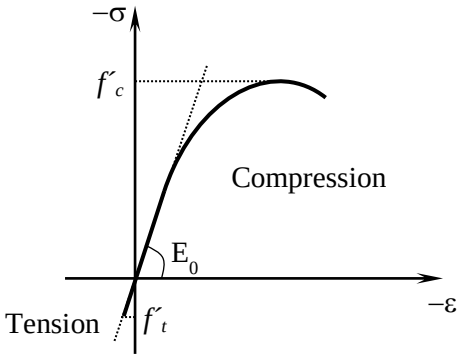

Figure 2-1 Typical Stress-Strain Curve for Plain Concrete under Uniaxial Deformation

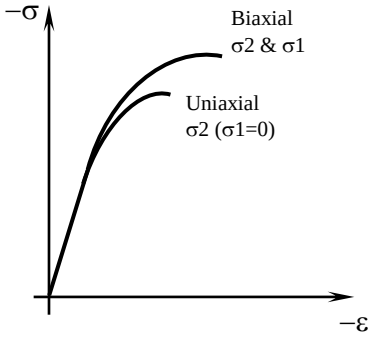

Figure 2-2 Effect of Biaxial Stress State on Behavior for Plain Concrete

The effect of biaxial stresses on the stress-strain behavior and on the strength of plain concrete is shown in Figure 2-2. Besides, under cyclic loading test, the hysteresis curves and its envelope curve (Skeleton Curve) are shown in the Figure 2-3. The area enclosed by each loop represents energy dissipated during each cycle. [12][39]

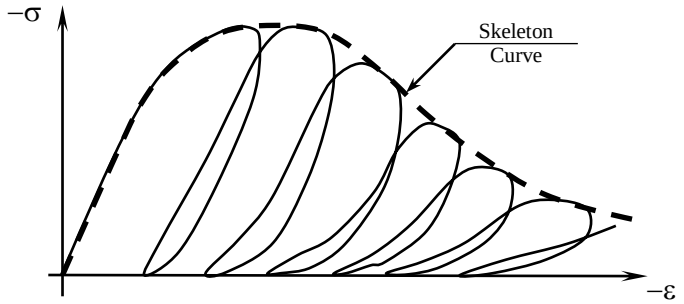

Figure 2-3 Behavior of Concrete Sample under Cycles of Compressive Loading

2.1.2 Reinforcing steel

On the other hand, regarding to the Reinforce Concrete, reinforcing steel behaves as a linear elastic material until reaches its yielding strength, after that, steel behaves in the plastic range, then strain hardening occurs, and finally failure (See Figure 2-4). However, Aktan et al. [3] and Singh et al. [38] found in their investigations, that steel behaves quite different under cycles of loading (See Figure 2-5). [9]

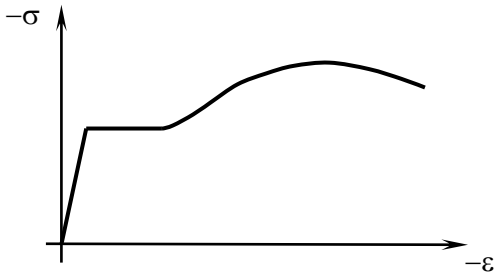

Figure 2-4 Typical Stress-Strain Curve of Steel under Monotonic Load

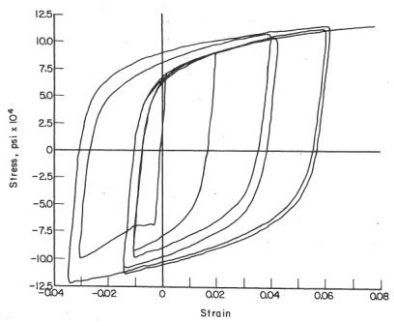

Figure 2-5 Behavior of Steel under Cyclic Loads

2.1.3 Carbon fiber sheet

Carbon fiber sheet (CFS) is formed by laying out fibers made of carbon, in a single or multiple directions and embedding them with a protective epoxy resin (See Figure 2-6). CFS has a higher strength, stiffness, corrosion and fatigue resistance whiting reasonable cost in comparison with other material such as glass or aramid. An advantage of using CFS is the negligible increase of the dead load due to its light weight. [19]

Figure 2-6 Carbon fiber sheet

CFS has a very high unidirectional tensile strength. Typical values are between 2500~4600 MPa for tensile strength and 235~260 GPa for Young's modulus. Essentially, CFS behavior is linear elastic up to the tensile strength limit where CFS rupture occurs. Once it reaches the tensile strength, CFS fails suddenly in a perfect brittle mode (Figure 2-7). Fibers are assumed to have strength and stiffness in the fiber direction but no resistance perpendicular to the fiber direction is considered. [19]

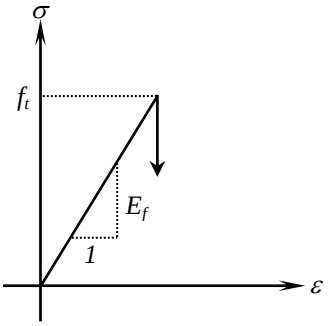

Figure 2-7 Linear-brittle model of CFS

2.2 Stress-strain relationship

Considering an isotropic element (3D or 2D element), which has the same properties in all analysis directions (See Figure 2-8), the strain-stress relationship is proportional to the Young Modulus (E) of the material as is given by: [4][8][31]

$$\sigma = E\varepsilon \tag{2-1}$$

Where the stress and strain tensor, in case of 3D element, are defined as follow:

$$\sigma = \begin{bmatrix} \sigma_{11} & \sigma_{12} & \sigma_{13} \\ \sigma_{21} & \sigma_{22} & \sigma_{23} \\ \sigma_{31} & \sigma_{32} & \sigma_{33} \end{bmatrix} \quad , \quad \varepsilon = \begin{bmatrix} \varepsilon_{11} & \varepsilon_{12} & \varepsilon_{13} \\ \varepsilon_{21} & \varepsilon_{22} & \varepsilon_{23} \\ \varepsilon_{31} & \varepsilon_{32} & \varepsilon_{33} \end{bmatrix}$$

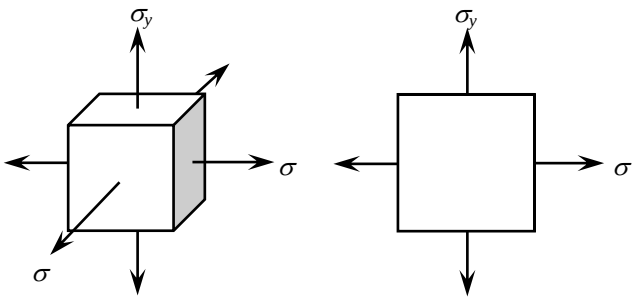

Figure 2-8 3D and 2D element

2.2.1 Constitutive equation

From the Equation (2-2), and applying volumetric deformation to each principal direction and considering Poisson ratio effect over the strain deformation, the following equations are given:

$$\left.\begin{aligned} \varepsilon_{xx} &= \frac{\sigma_{xx}}{E} - \nu\frac{\sigma_{yy}}{E} - \nu\frac{\sigma_{zz}}{E} = \frac{1}{E}\left(\sigma_{xx} - \nu\left(\sigma_{yy} + \sigma_{zz}\right)\right) \\ \varepsilon_{yy} &= -\nu\frac{\sigma_{xx}}{E} + \frac{\sigma_{yy}}{E} - \nu\frac{\sigma_{zz}}{E} = \frac{1}{E}\left(\sigma_{yy} - \nu(\sigma_{xx} + \sigma_{zz})\right) \\ \varepsilon_{zz} &= -\nu\frac{\sigma_{xx}}{E} - \nu\frac{\sigma_{yy}}{E} + \frac{\sigma_{zz}}{E} = \frac{1}{E}\left(\sigma_{zz} - \nu\left(\sigma_{xx} + \sigma_{yy}\right)\right) \end{aligned}\right\} \tag{2-2}$$

Besides, shear strain γ, is defined as follow:

$$\left.\begin{aligned} \gamma_{xy} = \gamma_{yx} &= \varepsilon_{xy} + \varepsilon_{yx} = {}^{\tau_{xy}}/_{G} \\ \gamma_{yz} = \gamma_{zy} &= \varepsilon_{yz} + \varepsilon_{zy} = {}^{\tau_{yz}}/_{G} \\ \gamma_{zx} = \gamma_{xz} &= \varepsilon_{zx} + \varepsilon_{xz} = {}^{\tau_{zx}}/_{G} \end{aligned}\right\} \tag{2-3}$$

In the same way, Equations (2-2) and (2-3) can be applied for a planar element, neglecting the third direction.

$$\left.\begin{aligned} \varepsilon_{xx} &= \frac{\sigma_{xx}}{E} - \nu\frac{\sigma_{yy}}{E} = \frac{1}{E}\left(\sigma_{xx} - \nu\sigma_{yy}\right) \\ \varepsilon_{yy} &= -\nu\frac{\sigma_{xx}}{E} + \frac{\sigma_{yy}}{E} = \frac{1}{E}\left(\sigma_{yy} - \nu\sigma_{xx}\right) \\ \gamma_{xy} = \gamma_{yx} &= \varepsilon_{xy} + \varepsilon_{yx} = {}^{\tau_{xy}}/_{G} \end{aligned}\right\} \tag{2-4}$$

2.2.2 Shear modulus

Considering a planar element subjected under pure shear state stress as is shown in Figure 2-9.

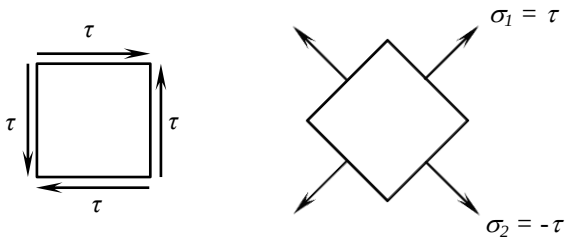

Figure 2-9 Pure shear on planar element

Where G is the Shear Modulus and the relationship between G, E and ν, using Equation (2-4) as follows:

$$\varepsilon_1 = \frac{\sigma_1}{E} - \nu\frac{\sigma_2}{E} = \frac{\tau}{E}(1+\nu)$$

$$\varepsilon_2 = -\nu\frac{\sigma_1}{E} + \frac{\sigma_2}{E} = -\frac{\tau}{E}(1+\nu)$$

$$\gamma = \frac{|\varepsilon_1| + |\varepsilon_2|}{2} = \frac{\varepsilon_1 - \varepsilon_2}{2} = \frac{2(1+\nu)}{E}\tau$$

$$\tau = G\gamma$$

$$G = \frac{E}{2(1+\nu)} \tag{2-5}$$

2.2.3 Shear strain

Figure 2-10 shows the shear strain deformation of a planar element.

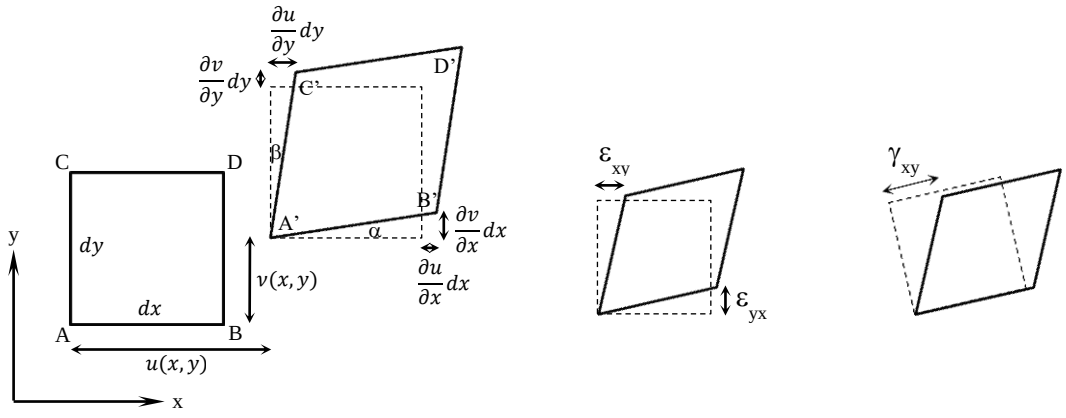

Figure 2-10 Shear strain deformation

Where: $\overline{AB} = dx$, is the original dimension of the planar element, and $\overline{A'B'}$ is the final dimension after the strain deformation.

$$\overline{A'B'} = \sqrt{\left(dx + \frac{\partial u}{\partial x}dx\right)^2 + \left(\frac{\partial v}{\partial x}dx\right)^2} \tag{2-6}$$

Taking into consideration very small displacements gradients, $\frac{\partial v}{\partial x}$ can be neglected, thus Equation (2-6) can be written as follows:

$$\overline{A'B'} = dx + \frac{\partial u}{\partial x}dx \tag{2-7}$$

Thus, strain deformation in x-direction and y-direction, ε_x and ε_y respectively, can be defined as the ratio of variation of the original longitude over the original longitude as follow:

$$\varepsilon_x = \frac{\overline{A'B'} - \overline{AB}}{\overline{AB}} = \frac{dx + \frac{\partial u}{\partial x}dx - dx}{dx}$$

$$\varepsilon_x = \frac{\partial u}{\partial x}$$

$$\varepsilon_y = \frac{\partial v}{\partial y} \tag{2-8}$$

Introducing shear strain as the summation of rotational deformation as follow:

$$\gamma_{xy} = \alpha + \beta$$

$$tan\alpha = \frac{\frac{\partial v}{\partial x}dx}{dx + \frac{\partial u}{\partial x}dx} = \frac{\frac{\partial v}{\partial x}}{1 + \frac{\partial u}{\partial x}}$$

$$tan\beta = \frac{\frac{\partial u}{\partial y}dy}{dy + \frac{\partial v}{\partial y}dy} = \frac{\frac{\partial u}{\partial y}}{1 + \frac{\partial v}{\partial y}}$$

For small displacement: $\frac{\partial u}{\partial x} \ll 1$ and $\frac{\partial v}{\partial y} \ll 1$

For small rotations α and β; thus $tan\alpha = \alpha$ and $tan\beta = \beta$

$$\alpha = \frac{\partial v}{\partial x} \quad , \quad \beta = \frac{\partial u}{\partial y}$$

$$\gamma_{xy} = \gamma_{yx} = \frac{\partial v}{\partial x} + \frac{\partial u}{\partial y} \tag{2-9}$$

Similarly, we can obtain the shear strain for y-z and z-x planes.

$$\left.\begin{aligned}\gamma_{yz} = \gamma_{zy} = \frac{\partial v}{\partial z} + \frac{\partial w}{\partial y}\\ \gamma_{zx} = \gamma_{xz} = \frac{\partial w}{\partial x} + \frac{\partial u}{\partial z}\end{aligned}\right\} \tag{2-10}$$

Going back to Equation (2-1):

$$\sigma = E\varepsilon \tag{2-11}$$

Where:

$$\varepsilon = \begin{bmatrix}\varepsilon_{11} & \varepsilon_{12} & \varepsilon_{13}\\ \varepsilon_{21} & \varepsilon_{22} & \varepsilon_{23}\\ \varepsilon_{31} & \varepsilon_{32} & \varepsilon_{33}\end{bmatrix} = \begin{bmatrix}\varepsilon_{xx} & \frac{\gamma_{xy}}{2} & \frac{\gamma_{xz}}{2}\\ \frac{\gamma_{yx}}{2} & \varepsilon_{yy} & \frac{\gamma_{yz}}{2}\\ \frac{\gamma_{zx}}{2} & \frac{\gamma_{zy}}{2} & \varepsilon_{zz}\end{bmatrix}$$

$$\sigma = \begin{bmatrix}\sigma_{11} & \sigma_{12} & \sigma_{13}\\ \sigma_{21} & \sigma_{22} & \sigma_{23}\\ \sigma_{31} & \sigma_{32} & \sigma_{33}\end{bmatrix} = \begin{bmatrix}\sigma_{xx} & \tau_{xy} & \tau_{xz}\\ \tau_{yx} & \sigma_{yy} & \tau_{yz}\\ \tau_{zx} & \tau_{zy} & \sigma_{zz}\end{bmatrix}$$

For isotropic materials, means that its physical properties are the same in each direction, therefore:

$$\left.\begin{aligned}\varepsilon_{xy} = \varepsilon_{yx} = {}^{\tau_{xy}}/_{2G}\\ \varepsilon_{yz} = \varepsilon_{zy} = {}^{\tau_{yz}}/_{2G}\\ \varepsilon_{zx} = \varepsilon_{xz} = {}^{\tau_{zx}}/_{2G}\end{aligned}\right\} \tag{2-12}$$

2.2.4 Strain and stress vector

From Equation (2-2) and (2-3), strain vector can be defined as follows:

$$\begin{Bmatrix}\varepsilon_{xx}\\ \varepsilon_{yy}\\ \varepsilon_{zz}\\ \gamma_{xy}\\ \gamma_{yz}\\ \gamma_{zx}\end{Bmatrix} = \begin{bmatrix}{}^{1}/_{E} & -{}^{\nu}/_{E} & -{}^{\nu}/_{E} & 0 & 0 & 0\\ -{}^{\nu}/_{E} & {}^{1}/_{E} & -{}^{\nu}/_{E} & 0 & 0 & 0\\ -{}^{\nu}/_{E} & -{}^{\nu}/_{E} & {}^{1}/_{E} & 0 & 0 & 0\\ 0 & 0 & 0 & {}^{1}/_{G} & 0 & 0\\ 0 & 0 & 0 & 0 & {}^{1}/_{G} & 0\\ 0 & 0 & 0 & 0 & 0 & {}^{1}/_{G}\end{bmatrix} \begin{Bmatrix}\sigma_{xx}\\ \sigma_{yy}\\ \sigma_{zz}\\ \tau_{xy}\\ \tau_{yz}\\ \tau_{zx}\end{Bmatrix} \tag{2-13}$$

Taking the inverse matrix, stress vector is given by:

$$\begin{Bmatrix}\sigma_{xx}\\ \sigma_{yy}\\ \sigma_{zz}\\ \tau_{xy}\\ \tau_{yz}\\ \tau_{zx}\end{Bmatrix}=\begin{bmatrix}2G+\lambda & \lambda & \lambda & 0 & 0 & 0\\ \lambda & 2G+\lambda & \lambda & 0 & 0 & 0\\ \lambda & \lambda & 2G+\lambda & 0 & 0 & 0\\ 0 & 0 & 0 & G & 0 & 0\\ 0 & 0 & 0 & 0 & G & 0\\ 0 & 0 & 0 & 0 & 0 & G\end{bmatrix}\begin{Bmatrix}\varepsilon_{xx}\\ \varepsilon_{yy}\\ \varepsilon_{zz}\\ \gamma_{xy}\\ \gamma_{yz}\\ \gamma_{zx}\end{Bmatrix} \tag{2-14}$$

Where λ is the Lame's first parameter defined as follows:

$$\lambda=\frac{\nu E}{(1+\nu)(1-2\nu)} \tag{2-15}$$

2.3 Stress and strain definitions

Basic definitions are introduced for the better understanding of the strain-stress relationship. [4][8][31]

2.3.1 Volumetric strain

The Volumetric Strain is defined as the total strain in the principal directions:

$$\varepsilon_{vol}=\varepsilon_{xx}+\varepsilon_{yy}+\varepsilon_{zz} \tag{2-16}$$

$$\varepsilon_{vol}=\frac{1}{E}\big(\sigma_{xx}-\nu\big(\sigma_{yy}+\sigma_{zz}\big)\big)+\frac{1}{E}\big(\sigma_{yy}-\nu(\sigma_{xx}+\sigma_{zz})\big)+\frac{1}{E}\big(\sigma_{zz}-\nu\big(\sigma_{xx}+\sigma_{yy}\big)\big)$$

$$\varepsilon_{vol}=\frac{1}{E}\Big(\big(\sigma_{xx}+\sigma_{yy}+\sigma_{zz}\big)-2\nu\big(\sigma_{xx}+\sigma_{yy}+\sigma_{zz}\big)\Big)$$

$$\varepsilon_{vol}=\big(\sigma_{xx}+\sigma_{yy}+\sigma_{zz}\big)\frac{(1-2\nu)}{E} \tag{2-17}$$

2.3.2 Hydrostatic strain and stress

Introducing the terms: Hydrostatic Strain ε_m and Hydrostatic Stress σ_m, both of them are defined as the average value of the principal strain and stress respectively as follow:

$$\left.\begin{aligned}\sigma_m&=\frac{\sigma_{xx}+\sigma_{yy}+\sigma_{zz}}{3}\\ \varepsilon_m&=\frac{\varepsilon_{xx}+\varepsilon_{yy}+\varepsilon_{zz}}{3}\end{aligned}\right\} \tag{2-18}$$

2.3.3 *Bulk modulus*

Using Equation (2-18) into the Equation (2-17):

$$\varepsilon_{vol} = 3\sigma_m \frac{(1-2\nu)}{E} \tag{2-19}$$

Where the ratio between σ_m and ε_{vol} is called Bulk Modulus (K):

$$K = \frac{\sigma_m}{\varepsilon_{vol}} = \frac{E}{3(1-2\nu)} \tag{2-20}$$

Therefore:

$$K = \frac{\sigma_m}{3\varepsilon_m} \tag{2-21}$$

2.3.4 *Deviatoric strain and deviatoric stress*

Deviatoric strain e_{ij} and deviatoric stress s_{ij}, is defined as follow (matrix notation):

$$\left.\begin{aligned} e_{ij} &= \varepsilon_{ij} - \delta_{ij}\varepsilon_m \\ s_{ij} &= \sigma_{ij} - \delta_{ij}\sigma_m \end{aligned}\right\} \tag{2-22}$$

Where δ_{ij}, called Kronecker Delta is defined as follow:

$$\delta_{ij} = \begin{cases} 0 \rightarrow i \neq j \\ 1 \rightarrow i = j \end{cases} \tag{2-23}$$

Therefore, going back to the Equation (2-11):

$$e = \begin{bmatrix} \varepsilon_{xx} - \varepsilon_m & \gamma_{xy}/2 & \gamma_{xz}/2 \\ \gamma_{yx}/2 & \varepsilon_{yy} - \varepsilon_m & \gamma_{yz}/2 \\ \gamma_{zx}/2 & \gamma_{zy}/2 & \varepsilon_{zz} - \varepsilon_m \end{bmatrix} \quad , \quad s = \begin{bmatrix} \sigma_{xx} - \sigma_m & \tau_{xy} & \tau_{xz} \\ \tau_{yx} & \sigma_{yy} - \sigma_m & \tau_{yz} \\ \tau_{zx} & \tau_{zy} & \sigma_{zz-\sigma_m} \end{bmatrix}$$

Then, from Equation (2-22):

$$e_{xx} = \varepsilon_{xx} - \varepsilon_m$$

$$e_{xx} = \frac{1}{E}\Big(\sigma_{xx} - \nu\big(\sigma_{yy} + \sigma_{zz}\big)\Big) - (1-2\nu)\frac{\sigma_m}{E}$$

$$e_{xx} = \frac{1}{E}\big(\sigma_{xx} - \nu\big(\sigma_{yy} + \sigma_{zz}\big) - (1-2\nu)\sigma_m\big)$$

$$e_{xx} = \frac{1}{E}\left(\sigma_{xx} - \sigma_m - \nu\left(\sigma_{yy} - \sigma_m + \sigma_{zz} - \sigma_m\right)\right)$$

$$e_{xx} = \frac{1}{E}\left(s_{xx} - \nu\left(s_{yy} + s_{zz}\right)\right) \tag{2-24}$$

Now replacing Equation (2-22) into Equation (2-18):

$$\frac{\sigma_{xx} + \sigma_{yy} + \sigma_{zz}}{3} = \sigma_m$$

$$s_{xx} = \sigma_{xx} - \sigma_m \quad , \quad s_{yy} = \sigma_{yy} - \sigma_m \quad , \quad s_{zz} = \sigma_{zz} - \sigma_m$$

$$s_{xx} + s_{yy} + s_{zz} = \sigma_{xx} + \sigma_{yy} + \sigma_{zz} - 3\sigma_m$$

$$s_{xx} + s_{yy} + s_{zz} = 0$$

Thus, going back to the Equation (2-24):

$$e_{xx} = \frac{1+\nu}{E} s_{xx} = \frac{s_{xx}}{2G} \tag{2-25}$$

Similarly:

$$\left.\begin{aligned} e_{yy} &= \frac{s_{yy}}{2G} \\ e_{zz} &= \frac{s_{zz}}{2G} \end{aligned}\right\} \tag{2-26}$$

Now strain can be expressed in function of deviatoric strain and hydrostatic strain as follow:

$$\varepsilon_{xx} = \varepsilon_m + e_{ij}$$

Using Equation (2-21) and Equation (2-25):

$$\varepsilon_{xx} = \frac{\sigma_m}{3K} + \frac{s_{xx}}{2G}$$

In the same way using Equation (2-26):

$$\varepsilon_{yy} = \frac{\sigma_m}{3K} + \frac{s_{yy}}{2G}$$

$$\varepsilon_{zz} = \frac{\sigma_m}{3K} + \frac{s_{zz}}{2G}$$

Writing in matrix notation:

$$\left.\begin{aligned} \varepsilon_{ij} &= \delta_{ij}\varepsilon_m + e_{ij} \\ \varepsilon_{ij} &= \delta_{ij}\frac{\sigma_m}{3K} + \frac{s_{ij}}{2G} \end{aligned}\right\} \tag{2-27}$$

2.3.5 Octahedral normal and shear strain and stress

The octahedral normal stress and strain is defined by hydrostatic components as follows:

$$\left.\begin{aligned}\sigma_o &= \frac{\sigma_1+\sigma_2+\sigma_3}{3}\\ \varepsilon_o &= \frac{\varepsilon_1+\varepsilon_2+\varepsilon_3}{3}\end{aligned}\right\} \tag{2-28}$$

The octahedral shear stress and strain in terms of principal stress and strain respectively is given by:

$$\left.\begin{aligned}\tau_o &= \frac{1}{3}\sqrt{(\sigma_1-\sigma_2)^2+(\sigma_2-\sigma_3)^2+(\sigma_3-\sigma_1)^2}\\ \gamma_o &= \frac{1}{3}\sqrt{(\varepsilon_1-\varepsilon_2)^2+(\varepsilon_2-\varepsilon_3)^2+(\varepsilon_3-\varepsilon_1)^2}\end{aligned}\right\} \tag{2-29}$$

For a biaxial strain-stress state, $\sigma_3 = 0$ is considered.

$$\begin{aligned}\sigma_o &= \frac{\sigma_1+\sigma_2}{3}\\ \tau_o &= \frac{\sqrt{2}}{3}\sqrt{{\sigma_1}^2-\sigma_1\sigma_2+{\sigma_2}^2}\end{aligned} \tag{2-30}$$

Similarly than Equation (2-21):

$$K = \frac{\sigma_o}{3\varepsilon_o} \tag{2-31}$$

And,

$$G = \frac{\tau_o}{2\gamma_o} \tag{2-32}$$

2.3.6 Invariants of stress tensor

Considering a 3D element as is shown in Figure 2-11, the relationship between the stress vector $\{\sigma\}$ on the surface of the 3D element and the stress vector $\{t\}$ on an inclined plane with a unit-length direction vector $\{n\}$ is expressed as follows:

$$\begin{Bmatrix}t_x\\ t_y\\ t_z\end{Bmatrix} = \begin{bmatrix}\sigma_x & \tau_{xy} & \tau_{xz}\\ \tau_{yx} & \sigma_y & \tau_{yz}\\ \tau_{zx} & \tau_{zy} & \sigma_z\end{bmatrix}\begin{Bmatrix}n_x\\ n_y\\ n_z\end{Bmatrix} \tag{2-33}$$

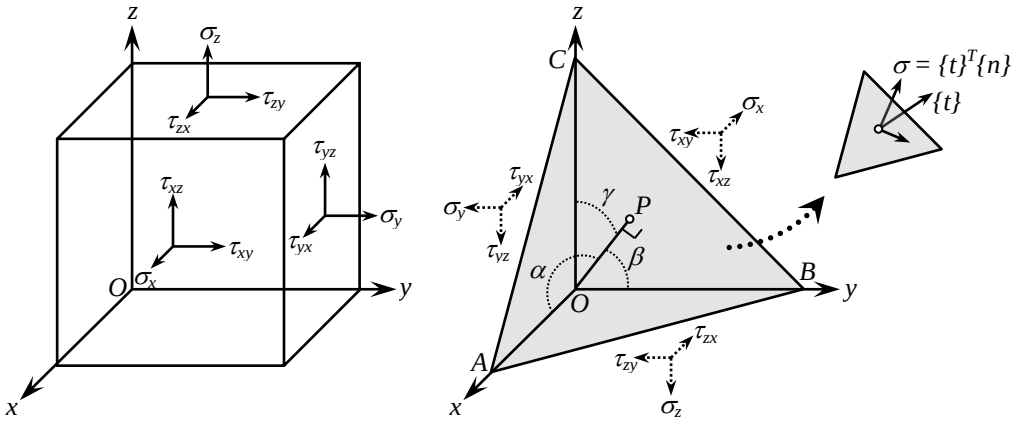

Figure 2-11 3D element and inclined plane

The relationship shown in Equation (2-33) is called "Cauchy stress tensor". From Figure 2-11, considering an inclined plane, where $\{t\}$ is a normal σ with zero shear stress, then:

$$\begin{Bmatrix} t_x \\ t_y \\ t_z \end{Bmatrix} = \begin{bmatrix} \sigma_x & \tau_{xy} & \tau_{xz} \\ \tau_{yx} & \sigma_y & \tau_{yz} \\ \tau_{zx} & \tau_{zy} & \sigma_z \end{bmatrix} \begin{Bmatrix} n_x \\ n_y \\ n_z \end{Bmatrix} = \sigma \begin{Bmatrix} n_x \\ n_y \\ n_z \end{Bmatrix}$$

or

$$\begin{bmatrix} \sigma_x - \sigma & \tau_{xy} & \tau_{xz} \\ \tau_{yx} & \sigma_y - \sigma & \tau_{yz} \\ \tau_{zx} & \tau_{zy} & \sigma_z - \sigma \end{bmatrix} \begin{Bmatrix} n_x \\ n_y \\ n_z \end{Bmatrix} = \begin{Bmatrix} 0 \\ 0 \\ 0 \end{Bmatrix} \tag{2-34}$$

To have a non-trivial solution, the determinant of the matrix shown above must be zero.

$$\begin{vmatrix} \sigma_x - \sigma & \tau_{xy} & \tau_{xz} \\ \tau_{yx} & \sigma_y - \sigma & \tau_{yz} \\ \tau_{zx} & \tau_{zy} & \sigma_z - \sigma \end{vmatrix} = 0$$

or

$$\sigma^3 - I_1\sigma^2 - I_2\sigma - I_3 = 0 \tag{2-35}$$

Where, I_1, I_2 and I_3 are called the "Invariants of the stress tensor" and are defined as follows:

$$\left.\begin{aligned} I_1 &= \sigma_x + \sigma_y + \sigma_z \\ I_2 &= \sigma_x\sigma_y + \sigma_y\sigma_z + \sigma_z\sigma_x - {\tau_{xy}}^2 - {\tau_{yz}}^2 - {\tau_{zx}}^2 \\ I_3 &= \sigma_x\sigma_y\sigma_z + 2\tau_{xy}\tau_{yz}\tau_{zx} - \sigma_x{\tau_{yz}}^2 - \sigma_y{\tau_{zx}}^2 - \sigma_z{\tau_{xy}}^2 \end{aligned}\right\} \tag{2-36}$$

The solution of Equation (2-35) has three answers $\{\sigma_1, \sigma_2, \sigma_3\}$ which are called the "Principle Stresses". Since the principle stresses also satisfy the Equation (2-35), the invariants of the stress tensor can be expressed by the following equation:

$$\left.\begin{array}{c} I_1 = \sigma_1 + \sigma_2 + \sigma_3 = 3\sigma_m \\ I_2 = \sigma_1\sigma_2 + \sigma_2\sigma_3 + \sigma_3\sigma_1 \\ I_3 = \sigma_1\sigma_2\sigma_3 \end{array}\right\} \quad (2\text{-}37)$$

Where σ_m is the hydrostatic stress. Besides it is known that the hydrostatic stress has no relation with yielding condition for metals, so it is convenient to define the deviatoric stress as follows:

$$\left.\begin{array}{l} {\sigma_1}' = \sigma_1 - \sigma_m \\ {\sigma_2}' = \sigma_2 - \sigma_m \\ {\sigma_3}' = \sigma_3 - \sigma_m \end{array}\right\} \quad (2\text{-}38)$$

Now by using Equation (2-38), the invariants of the deviatoric stress tensor are defined as follows:

$$\left.\begin{array}{c} J_1 = {\sigma_x}' + {\sigma_y}' + {\sigma_z}' = {\sigma_1}' + {\sigma_2}' + {\sigma_3}' = 0 \\ J_2 = \frac{1}{2}\left(\left({\sigma_x}'^2 + {\sigma_y}'^2 + {\sigma_z}'^2\right) + 2\left({\tau_{xy}}^2 + {\tau_{yz}}^2 + {\tau_{zx}}^2\right)\right) \\ J_2 = -({\sigma_1}'{\sigma_2}' + {\sigma_2}'{\sigma_3}' + {\sigma_3}'{\sigma_1}') = \frac{1}{2}({\sigma_1}'^2 + {\sigma_2}'^2 + {\sigma_3}'^2) \\ J_2 = \frac{1}{6}\left(\left(\sigma_x - \sigma_y\right)^2 + \left(\sigma_y - \sigma_z\right)^2 + (\sigma_z - \sigma_x)^2 + 6\left({\tau_{xy}}^2 + {\tau_{yz}}^2 + {\tau_{zx}}^2\right)\right) \\ J_2 = \frac{1}{6}((\sigma_1 - \sigma_2)^2 + (\sigma_2 - \sigma_3)^2 + (\sigma_3 - \sigma_1)^2) \\ J_2 = \frac{1}{3}\left({I_1}^3 - 3I_2\right) \\ J_3 = \sigma_x\sigma_y\sigma_z + 2\tau_{xy}\tau_{yz}\tau_{zx} - \sigma_x{\tau_{yz}}^2 - \sigma_y{\tau_{zx}}^2 - \sigma_z{\tau_{xy}}^2 \end{array}\right\} \quad (2\text{-}39)$$

CHAPTER 3

FINITE ELEMENT METHOD

ELASTIC THEORY

CHAPTER 3 : FINITE ELEMENT ANALYSIS – ELASTIC THEORY

3.1 Plane analysis

Considering a triangular element for plane analysis, the problem is to obtain the nodal deformations of the element shown in Figure 3-1. The deform shape of the triangular element has infinite of variations of deformation patterns as is schematized in Figure 3-2. [4][8][31]

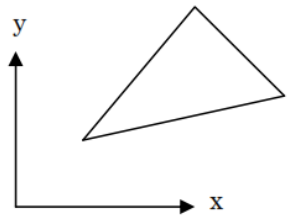

Figure 3-1 Triangular element

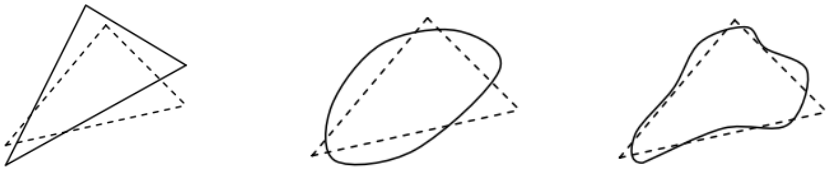

Figure 3-2 Deform shape of triangular element

Assuming a linear function to represent the deform shape of the triangular element shown in Figure 3-2 and the deform shape functions are described below:

$$\left.\begin{aligned} u_{(x,y)} &= \alpha_1 + \alpha_2 x + \alpha_3 y \\ v_{(x,y)} &= \alpha_4 + \alpha_5 x + \alpha_6 y \end{aligned}\right\} \tag{3-1}$$

In matrix notation:

$$\begin{Bmatrix} u \\ v \end{Bmatrix} = \begin{bmatrix} 1 & x & y & 0 & 0 & 0 \\ 0 & 0 & 0 & 1 & x & y \end{bmatrix} \begin{Bmatrix} \alpha_1 \\ \alpha_2 \\ \alpha_3 \\ \alpha_4 \\ \alpha_5 \\ \alpha_6 \end{Bmatrix} \tag{3-2}$$

The relation between nodal displacement and element deformation by using Equation (3-2) are expressed as follows:

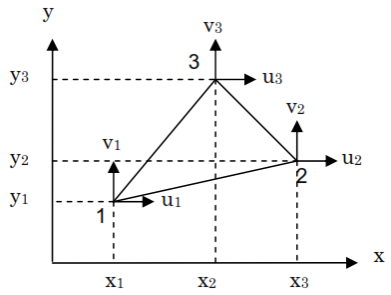

Figure 3-3 Coordinates of triangular element

$$\begin{Bmatrix} u_1 \\ u_2 \\ u_3 \\ v_1 \\ v_2 \\ v_3 \end{Bmatrix} = \begin{bmatrix} 1 & x_1 & y_1 & 0 & 0 & 0 \\ 1 & x_2 & y_2 & 0 & 0 & 0 \\ 1 & x_3 & y_3 & 0 & 0 & 0 \\ 0 & 0 & 0 & 1 & x_1 & y_1 \\ 0 & 0 & 0 & 1 & x_2 & y_2 \\ 0 & 0 & 0 & 1 & x_3 & y_3 \end{bmatrix} \begin{Bmatrix} \alpha_1 \\ \alpha_2 \\ \alpha_3 \\ \alpha_4 \\ \alpha_5 \\ \alpha_6 \end{Bmatrix} \tag{3-3}$$

$$U = A \alpha$$

From the above equation, coefficients $\alpha_1, \alpha_2, \cdots, \alpha_6$ can be obtained as follows:

$$\alpha = A^{-1} U \tag{3-4}$$

Substituting Equation (3-4) into Equation (3-2), the relation between nodal displacement and element deformation is described as below:

$$\begin{Bmatrix} u \\ v \end{Bmatrix} = \begin{bmatrix} 1 & x & y & 0 & 0 & 0 \\ 0 & 0 & 0 & 1 & x & y \end{bmatrix} A^{-1} \begin{Bmatrix} u_1 \\ u_2 \\ u_3 \\ v_1 \\ v_2 \\ v_3 \end{Bmatrix} \tag{3-5}$$

$$u_{(x,y)} = H_{(x,y)} U$$

The constitutive equation at the nodes can be obtained between the nodal force and the nodal displacement, for example, by using the “Principle of Virtual Work Method”.

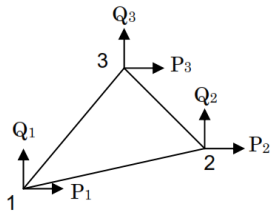

Figure 3-4 Coordinates of triangular element

$$\begin{Bmatrix} P_1 \\ P_2 \\ P_3 \\ Q_1 \\ Q_2 \\ Q_3 \end{Bmatrix} = K \begin{Bmatrix} u_1 \\ u_2 \\ u_3 \\ v_1 \\ v_2 \\ v_3 \end{Bmatrix} \tag{3-6}$$

$$F = K\,U$$

The process is summarized as follows:

(1) Translate external forces into equivalent nodal force:

$$F = \{P_1, P_2, P_3, Q_1, Q_2, Q_3\}^T$$

(2) Calculate the nodal displacements from the constitutive equation. Where K is called the stiffness matrix:

$$U = K^{-1}F$$

(3) Obtain the element deformation from the nodal displacement:

$$u_{(x,y)} = H_{(x,y)}U$$

3.2 Stiffness matrix for planar element

Stiffness matrix in Equation (3-6) can be obtained from the "Principle of Virtual Work Method" [4][8][31] which is expressed as follows:

$$\int_V \bar{\varepsilon}^T \sigma dv = \bar{U}^T F \tag{3-7}$$

Where, $\bar{\varepsilon}$ is the virtual strain vector, σ is the stress vector, $\bar{U}$ is the virtual displacement vector and F is the load vector.

In case if a plane element, the strain ε is defined as:

$$\begin{Bmatrix} \varepsilon_x \\ \varepsilon_y \\ \gamma_{xy} \end{Bmatrix} = \begin{Bmatrix} \dfrac{\partial u}{\partial x} \\ \dfrac{\partial v}{\partial x} \\ \dfrac{\partial u}{\partial x} + \dfrac{\partial v}{\partial x} \end{Bmatrix} \tag{3-8}$$

Substituting Equation (3-5) into Equation (3-8), the strain vector is calculated from the nodal displacement vector as follows:

$$\begin{Bmatrix}\varepsilon_x\\ \varepsilon_y\\ \gamma_{xy}\end{Bmatrix} = \begin{Bmatrix}\dfrac{\partial u}{\partial x}\\ \dfrac{\partial v}{\partial x}\\ \dfrac{\partial u}{\partial x}+\dfrac{\partial v}{\partial x}\end{Bmatrix} = \begin{bmatrix}0 & 1 & 0 & 0 & 0 & 0\\ 0 & 0 & 0 & 0 & 0 & 1\\ 0 & 0 & 1 & 0 & 1 & 0\end{bmatrix} A^{-1} \begin{Bmatrix}u_1\\ u_2\\ u_3\\ v_1\\ v_2\\ v_3\end{Bmatrix} \tag{3-9}$$

$$\varepsilon \quad = \qquad\qquad B \qquad\qquad U$$

In the plane stress problem, the stress-strain relationship is expressed as:

$$\begin{Bmatrix}\sigma_x\\ \sigma_y\\ \tau_{xy}\end{Bmatrix} = \frac{\mathrm{E}}{1-\nu^2}\begin{bmatrix}1 & \nu & 0\\ \nu & 0 & 0\\ 0 & 0 & \dfrac{1-\nu}{2}\end{bmatrix}\begin{Bmatrix}\varepsilon_x\\ \varepsilon_y\\ \gamma_{xy}\end{Bmatrix} \tag{3-10}$$

$$\sigma \quad = \qquad D \qquad \varepsilon$$

Substituting Equation (3-9) into Equation (3-10),

$$\sigma = DBU \tag{3-11}$$

From the Principle of the Virtual Work Method,

$$\int_V \left(B\overline{U}\right)^T (DBU)dv = \overline{U}^T\left(\int_V B^T DBdv\right)U = \overline{U}^T F \tag{3-12}$$

Therefore, the constitutive equation is obtained as follows:

$$F = KU \quad , \quad K = \int_V B^T DBdv \tag{3-13}$$

3.3 Interpolation function

Considering one dimensional element under loading, a linear function for the deformation pattern after loading is assumed as is shown in Figure 3-5. [4][8][31]

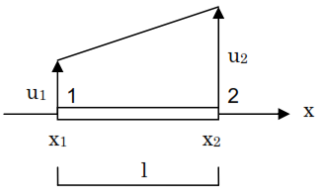

Figure 3-5 One dimensional element

$$u_{(x)} = a_0 + a_1 x$$
$$u_{(x)} = (0 \quad 1)\begin{pmatrix} a_0 \\ a_1 \end{pmatrix} \tag{3-14}$$

The next step is to obtain the coefficients, a_0 and a_1, from the nodal displacements from the following relations:

$$u_1 = a_0 + a_1 x_1$$
$$u_2 = a_0 + a_1 x_2$$

Writing in matrix notation:

$$\begin{pmatrix} a_0 \\ a_1 \end{pmatrix} = \begin{pmatrix} 1 & x_1 \\ 1 & x_2 \end{pmatrix}\begin{pmatrix} a_0 \\ a_1 \end{pmatrix}$$
$$U = A\alpha \tag{3-15}$$

The coefficients are obtained as $\alpha = A^{-1}U$. Then, the relation between the deformation and the nodal displacements is,

$$u_{(x)} = (1 \quad x)A^{-1}\begin{pmatrix} u_1 \\ u_2 \end{pmatrix} \tag{3-16}$$

Instead of previous procedure, an interpolation function is introduced to express the deformation directly from the nodal displacements:

$$u_{(x)} = h_{1(x)}u_1 + h_{2(x)}u_2 \tag{3-17}$$

The interpolation functions h_1 and h_2 has the following characteristics:

$$h_{1(x)} = \begin{cases} 1 & , \quad x = u_1 \\ 0 & , \quad x \neq u_1 \end{cases} \qquad h_{2(x)} = \begin{cases} 1 & , \quad x = u_2 \\ 0 & , \quad x \neq u_2 \end{cases} \tag{3-18}$$

From Equation (3-18), interpolation functions are described below:

$$h_{1(x)} = \frac{x_2 - x}{l} \qquad h_{2(x)} = \frac{x_2 - x}{l} \tag{3-19}$$

The advantage of using an interpolation function is to reduce the burden to calculate the inverse matrix A in Equation (3-16). In the same manner, by introducing a second order interpolation function for the deformation patter, the deformation can be directly express following Equation (3-20). A schematic representation of the first order and second order interpolation function is shown in Figure 3-6.

$$u_{(x)} = h_{1(x)}u_1 + h_{2(x)}u_2 + h_{3(x)}u_3 \tag{3-20}$$

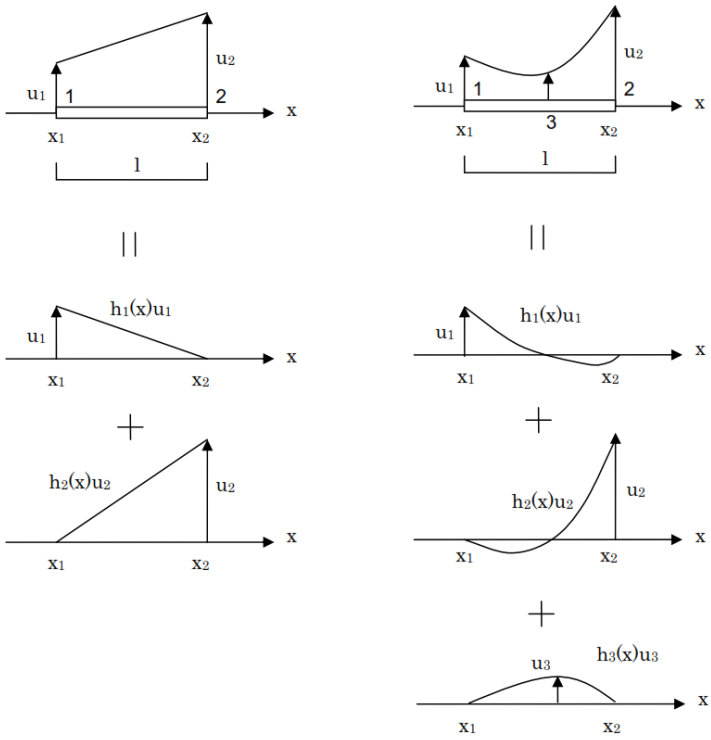

Figure 3-6 Schematic explanation of interpolation function

3.4 Natural coordinate

For an easy understanding, let's consider the measure of the total weight of the pencil shown in Figure 3-7, by using two coordinate scales, x-coordinate and t-coordinate. [4][8][31]

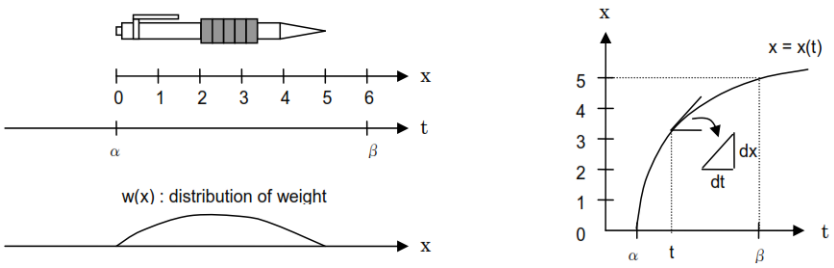

Figure 3-7 Natural coordinate relationship

The total weight can be express as follows:

$$W = \int_0^5 w_{(x)} dx \tag{3-21}$$

The relationship between x-coordinate and t-coordinated for the global relationship and the local relationship are described in Equations (3-22) and (3-23) respectively:

$$x = x_{(t)} \tag{3-22}$$

$$dx = \frac{dx_{(t)}}{dt} dt \tag{3-23}$$

Where $\mathrm{d}x_{(t)}/\mathrm{dt}$ represents the first derivative of $x_{(t)}$ by the variable t, which correspond to the slope of $x_{(t)}$ at t. Substituting Equations (3-22) and (3-23) into (3-21), the total weight can be expressed in t-axis as.

$$W = \int_{\alpha}^{\beta} w_{(x_{(t)})} \frac{dx_{(t)}}{dt} dt \tag{3-24}$$

By setting $\alpha = -1$ and$\beta = 1$, Equation (3-24) can be written as follows:

$$W = \int_{-1}^{1} f_{(t)} dt \quad , \quad f_{(t)} = w_{(x_{(t)})} \frac{dx_{(t)}}{dt} \tag{3-25}$$

3.5 Gaussian quadrature rule

Considering an integration range [-1,1], the integration can be evaluated approximately by n-point Gaussian quadrature rule [4][8][31], which is generally expressed as follows:

$$\int_{-1}^{1} f_{(t)} dt \approx w_1 f_{(t_1)} + w_2 f_{(t_2)} + \cdots + w_n f_{(t_n)} \tag{3-26}$$

Where, $w_1, w_2, \cdots, w_n$ are the weighting coefficients. This formula requires a limited number of functions values, $f_{(t_1)}, f_{(t_2)}, \cdots, f_{(t_n)}$, at the sampling points, $t_1, t_2, \cdots, t_n$, to evaluate the integration.

This study will use 3 point Gaussian quadrature rule as is shown in Figure 3-8, and the corresponding weighting coefficients are described below:

$$\int_{-1}^{1} f_{(t)} dt = w_1 f_{(t_1)} + w_2 f_{(t_2)} + w_3 f_{(t_3)}$$

$$\int_{-1}^{1} f_{(t)} dt = 0.5556 f_{(-0.7746)} + 0.8889 f_{(0)} + 0.5556 f_{(0.7746)}$$

Where:

$$w_1 = \frac{5}{9} = 0.5556 \quad , \quad w_2 = \frac{8}{9} = 0.8889 \quad , \quad w_3 = \frac{5}{9} = 0.5556$$

$$t_1 = -\sqrt{0.6} = -0.7746 \quad , \quad t_2 = 0 \quad , \quad t_3 = \sqrt{0.6} = 0.7746$$

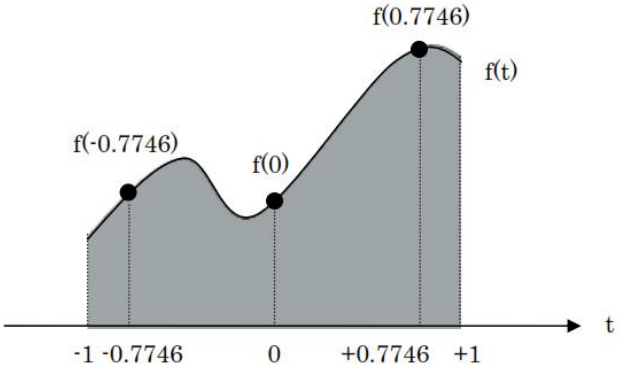

Figure 3-8 3 point Gaussian quadrature rule

3.6 Isoparametric element

Considering on dimensional element as is shown in Figure 3-9, the natural coordinate in introduced to this element. [4][8][31]

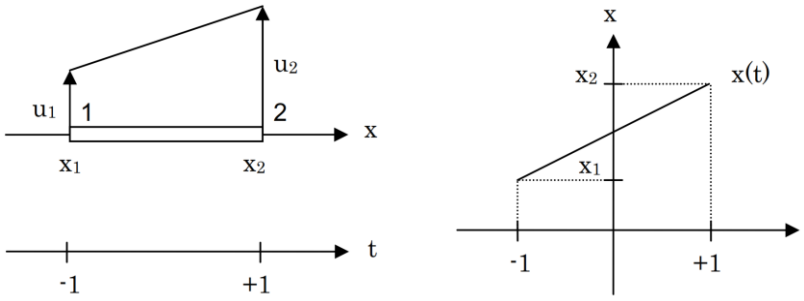

Figure 3-9 One dimensional element

By assuming the linear transfer function $x_{(t)}$ between x-axis and t-axis, $x_{(t)}$ can be expressed as follows:

$$x_{(t)} = h_{1(t)}x_1 + h_{2(t)}x_2 \tag{3-27}$$

Where:

$$h_{1(t)} = \frac{1}{2}(1-t) \quad , \quad h_{2(t)} = \frac{1}{2}(1+t) \tag{3-28}$$

Equations (3-27) and (3-28) satisfies that $x_{(-1)} = x_1$ and $x_{(1)} = x_2$.

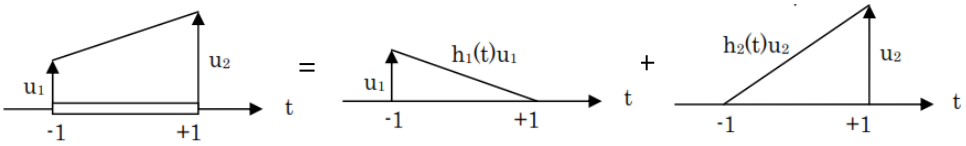

Figure 3-10 Deformation of one dimensional element

From Figure 3-10, the deformation of one dimensional element can be obtained by using the interpolation functions $h_{1(t)}$ and $h_{2(t)}$ as is shown in Equation (3-29).

$$u_{(t)} = h_{1(t)}u_1 + h_{2(t)}u_2 \tag{3-29}$$

The element where both, the coordinate transfer function $x_{(t)}$ and the deformation function $u_{(t)}$, are expressed using the same interpolation functions on the natural coordinates called “Isoparametric element”.

The advantages of using isoparametric elements are described below:

(1) The relation $u_{(t)} = \sum_{i=1}^{n} h_{i(t)}u_i$ does not require the calculation of inverse matrix.
(2) The relation $x_{(t)} = \sum_{i=1}^{n} h_{i(t)}x_i$ enables to use the numerical integration method.
(3) Both functions $u_{(t)}$ and $x_{(t)}$ are expressed using the same interpolation functions.

3.7 Stiffness matrix for isoparametric element

Taking into consideration 4-nodes two dimensional isoparametric element (see Figure 3-11), the coordinate transfer function and the deformation function are expressed using the interpolation function as is shown in Equations (3-30) and (3-31) respectively. [4][8][31]

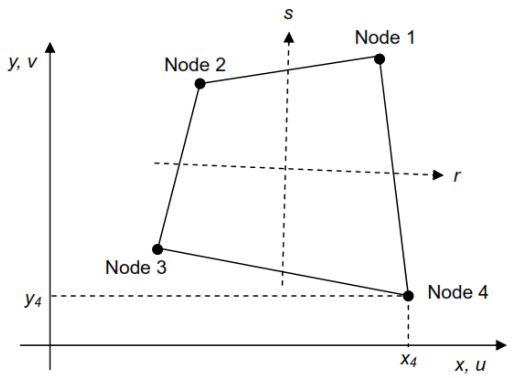

Figure 3-11 4-nodes isoparametric element

$$x_{(r,s)} = \sum_{i=1}^{4} h_{i(r,s)} x_i \quad , \quad y_{(r,s)} = \sum_{i=1}^{4} h_{i(r,s)} y_i$$

$$\begin{aligned} x_{(r,s)} &= \tfrac{1}{4}(1+r)(1+s)x_1 + \tfrac{1}{4}(1-r)(1+s)x_2 + \tfrac{1}{4}(1-r)(1-s)x_3 + \tfrac{1}{4}(1+r)(1-s)x_4 \\ y_{(r,s)} &= \tfrac{1}{4}(1+r)(1+s)y_1 + \tfrac{1}{4}(1-r)(1+s)y_2 + \tfrac{1}{4}(1-r)(1-s)y_3 + \tfrac{1}{4}(1+r)(1-s)y_4 \end{aligned} \tag{3-30}$$

$$u_{(r,s)} = \sum_{i=1}^{4} h_{i(r,s)} u_i \quad , \quad v_{(r,s)} = \sum_{i=1}^{4} h_{i(r,s)} v_i$$

$$\begin{aligned} u_{(r,s)} &= \tfrac{1}{4}(1+r)(1+s)u_1 + \tfrac{1}{4}(1-r)(1+s)u_2 + \tfrac{1}{4}(1-r)(1-s)u_3 + \tfrac{1}{4}(1+r)(1-s)u_4 \\ v_{(r,s)} &= \tfrac{1}{4}(1+r)(1+s)v_1 + \tfrac{1}{4}(1-r)(1+s)v_2 + \tfrac{1}{4}(1-r)(1-s)v_3 + \tfrac{1}{4}(1+r)(1-s)v_4 \end{aligned} \tag{3-31}$$

Expressing Equation (3-31) in matrix notation:

$$\begin{Bmatrix} u_{(r,s)} \\ v_{(r,s)} \end{Bmatrix} = \begin{bmatrix} h_{1(r,s)} & 0 & h_{2(r,s)} & 0 & h_{3(r,s)} & 0 & h_{4(r,s)} & 0 \\ 0 & h_{1(r,s)} & 0 & h_{2(r,s)} & 0 & h_{3(r,s)} & 0 & h_{4(r,s)} \end{bmatrix} \begin{Bmatrix} u_1 \\ v_1 \\ u_2 \\ v_2 \\ u_3 \\ v_3 \\ u_4 \\ v_4 \end{Bmatrix} \tag{3-32}$$

$$u_{(r,s)} = \qquad H_{(r,s)} \qquad U$$

Stiffness matrix can be obtained from the Principle of Virtual Work Method, which is expressed in the following form:

$$\int_V \bar{\varepsilon}^T \sigma dv = \bar{U}^T F \tag{3-33}$$

Where, $\bar{\varepsilon}$ is the virtual strain vector, σ is the stress vector, $\bar{U}$ is the virtual displacement vector and F is the load vector respectively. In case of the 4 nodes two dimensional isoparametric element, the strain vector ε is defined as follows:

$$\begin{Bmatrix} \varepsilon_x \\ \varepsilon_y \\ \gamma_{xy} \end{Bmatrix} = \begin{Bmatrix} \dfrac{\partial u}{\partial x} \\ \dfrac{\partial v}{\partial x} \\ \dfrac{\partial u}{\partial x} + \dfrac{\partial v}{\partial x} \end{Bmatrix} \tag{3-34}$$

Substituting Equation (3-31) into Equation (3-34), the strain vector is calculated as:

$$\begin{Bmatrix} \varepsilon_x \\ \varepsilon_y \\ \gamma_{xy} \end{Bmatrix} = \begin{Bmatrix} \dfrac{\partial u}{\partial x} \\ \dfrac{\partial v}{\partial y} \\ \dfrac{\partial u}{\partial y} + \dfrac{\partial v}{\partial x} \end{Bmatrix} = \begin{Bmatrix} \displaystyle\sum_{i=1}^{4} \frac{\partial h_i}{\partial x} u_i \\ \displaystyle\sum_{i=1}^{4} \frac{\partial h_i}{\partial y} v_i \\ \displaystyle\sum_{i=1}^{4} \frac{\partial h_i}{\partial y} u_i + \sum_{i=1}^{4} \frac{\partial h_i}{\partial x} v_i \end{Bmatrix}$$

$$\begin{Bmatrix} \varepsilon_x \\ \varepsilon_y \\ \gamma_{xy} \end{Bmatrix} = \begin{bmatrix} \dfrac{\partial h_1}{\partial x} & 0 & \dfrac{\partial h_2}{\partial x} & 0 & \dfrac{\partial h_3}{\partial x} & 0 & \dfrac{\partial h_4}{\partial x} & 0 \\ 0 & \dfrac{\partial h_1}{\partial y} & 0 & \dfrac{\partial h_2}{\partial y} & 0 & \dfrac{\partial h_3}{\partial y} & 0 & \dfrac{\partial h_4}{\partial y} \\ \dfrac{\partial h_1}{\partial y} & \dfrac{\partial h_1}{\partial x} & \dfrac{\partial h_2}{\partial y} & \dfrac{\partial h_2}{\partial x} & \dfrac{\partial h_3}{\partial y} & \dfrac{\partial h_3}{\partial x} & \dfrac{\partial h_4}{\partial y} & \dfrac{\partial h_4}{\partial x} \end{bmatrix} \begin{Bmatrix} u_1 \\ v_1 \\ u_2 \\ v_2 \\ u_3 \\ v_3 \\ u_4 \\ v_4 \end{Bmatrix} \tag{3-35}$$

$$\varepsilon = B U$$

In the plane stress problem, the stress-strain relationship is expressed as follows:

$$\begin{Bmatrix} \sigma_x \\ \sigma_y \\ \tau_{xy} \end{Bmatrix} = \frac{\mathrm{E}}{1-\nu^2} \begin{bmatrix} 1 & \nu & 0 \\ \nu & 0 & 0 \\ 0 & 0 & \dfrac{1-\nu}{2} \end{bmatrix} \begin{Bmatrix} \varepsilon_x \\ \varepsilon_y \\ \gamma_{xy} \end{Bmatrix} \tag{3-36}$$

$$\sigma = D \varepsilon$$

Substituting Equation (3-35) into Equation (3-36),

$$\sigma = DBU \tag{3-37}$$

From the Principle of Virtual Work Method:

$$\int_V \left(B\overline{U}\right)^T (DBU) dv = \overline{U}^T \left(\int_V B^T D B dv \right) U = \overline{U}^T F \tag{3-38}$$

Therefore, the constitutive equation is obtained as follows:

$$F = KU \quad , \quad K = \int_V B^T DB dv \tag{3-39}$$

By assuming a constant thickness t of the isoparametric element,

$$K = t \int_{V(x,y)} B^T DB dx dy \tag{3-40}$$

The following relationship is also derived from Equation (3-38)

$$\int_V \left(B\overline{U}\right)^T \{\sigma\} dv = \overline{U}^T \left(\int_V B^T \{\sigma\} dv \right) U = \overline{U}^T F \tag{3-41}$$

Therefore, the relationship between stress vector and nodal force is as follows:

$$F = \int_V B^T \{\sigma\} dv \tag{3-42}$$

Since this integration is defined in x-y coordinates, we must transfer the coordinate into r-s coordinate to use the numerical integration method. Introducing the Jacobian Matrix, J:

$$J = \begin{bmatrix} \frac{\partial x}{\partial r} & \frac{\partial y}{\partial r} \\ \frac{\partial x}{\partial s} & \frac{\partial x}{\partial s} \end{bmatrix} \tag{3-43}$$

Now, Equation (3-40) can be expressed in r-s coordinates as follows:

$$K = t \int_{-1}^{1} \int_{-1}^{1} B_{(x(r,s),y(r,s))}{}^T DB_{(x(r,s),y(r,s))} \frac{\partial(x,y)}{\partial(r,s)} dr ds \tag{3-44}$$

Where:

$$\frac{\partial(x,y)}{\partial(r,s)} = \begin{vmatrix} \frac{\partial x}{\partial r} & \frac{\partial y}{\partial r} \\ \frac{\partial x}{\partial s} & \frac{\partial x}{\partial s} \end{vmatrix} \tag{3-45}$$

Summarizing the process:

(1) Evaluation of Jacobian Matrix:

$$J = \begin{bmatrix} \frac{\partial x}{\partial r} & \frac{\partial y}{\partial r} \\ \frac{\partial x}{\partial s} & \frac{\partial y}{\partial s} \end{bmatrix} = \begin{bmatrix} \sum_{i=1}^{4} \frac{\partial h_i}{\partial r} x_i & \sum_{i=1}^{4} \frac{\partial h_i}{\partial r} y_i \\ \sum_{i=1}^{4} \frac{\partial h_i}{\partial s} x_i & \sum_{i=1}^{4} \frac{\partial h_i}{\partial s} y_i \end{bmatrix} \tag{3-46}$$

(2) Evaluation of B matrix:

From Equation (3-35):

$$B = \begin{bmatrix} \frac{\partial h_1}{\partial x} & 0 & \frac{\partial h_2}{\partial x} & 0 & \frac{\partial h_3}{\partial x} & 0 & \frac{\partial h_4}{\partial x} & 0 \\ 0 & \frac{\partial h_1}{\partial y} & 0 & \frac{\partial h_2}{\partial y} & 0 & \frac{\partial h_3}{\partial y} & 0 & \frac{\partial h_4}{\partial y} \\ \frac{\partial h_1}{\partial y} & \frac{\partial h_1}{\partial x} & \frac{\partial h_2}{\partial y} & \frac{\partial h_2}{\partial x} & \frac{\partial h_3}{\partial y} & \frac{\partial h_3}{\partial x} & \frac{\partial h_4}{\partial y} & \frac{\partial h_4}{\partial x} \end{bmatrix} \tag{3-47}$$

Where the derivatives $\frac{\partial h_1}{\partial x}, \cdots, \frac{\partial h_4}{\partial x}, \frac{\partial h_1}{\partial y}, \cdots, \frac{\partial h_4}{\partial y}$ are calculated as:

$$\begin{aligned} \frac{\partial h_1}{\partial x} &= \frac{\partial h_1}{\partial r}\frac{\partial r}{\partial x} + \frac{\partial h_1}{\partial s}\frac{\partial s}{\partial x} \quad ,\cdots, \quad \frac{\partial h_4}{\partial x} = \frac{\partial h_4}{\partial r}\frac{\partial r}{\partial x} + \frac{\partial h_4}{\partial s}\frac{\partial s}{\partial x} \\ \frac{\partial h_1}{\partial y} &= \frac{\partial h_1}{\partial r}\frac{\partial r}{\partial y} + \frac{\partial h_1}{\partial s}\frac{\partial s}{\partial y} \quad ,\cdots, \quad \frac{\partial h_4}{\partial y} = \frac{\partial h_4}{\partial r}\frac{\partial r}{\partial y} + \frac{\partial h_4}{\partial s}\frac{\partial s}{\partial y} \end{aligned}$$

In matrix notation,

$$\begin{bmatrix} \frac{\partial h_1}{\partial x} & \frac{\partial h_2}{\partial x} & \frac{\partial h_3}{\partial x} & \frac{\partial h_4}{\partial x} \\ \frac{\partial h_1}{\partial y} & \frac{\partial h_2}{\partial y} & \frac{\partial h_3}{\partial y} & \frac{\partial h_4}{\partial y} \end{bmatrix} = \begin{bmatrix} \frac{\partial r}{\partial x} & \frac{\partial s}{\partial x} \\ \frac{\partial r}{\partial y} & \frac{\partial s}{\partial y} \end{bmatrix} \begin{bmatrix} \frac{\partial h_1}{\partial r} & \frac{\partial h_2}{\partial r} & \frac{\partial h_3}{\partial r} & \frac{\partial h_4}{\partial r} \\ \frac{\partial h_1}{\partial s} & \frac{\partial h_2}{\partial s} & \frac{\partial h_3}{\partial s} & \frac{\partial h_4}{\partial s} \end{bmatrix} = J^{-1} \begin{bmatrix} \frac{\partial h_1}{\partial r} & \frac{\partial h_2}{\partial r} & \frac{\partial h_3}{\partial r} & \frac{\partial h_4}{\partial r} \\ \frac{\partial h_1}{\partial s} & \frac{\partial h_2}{\partial s} & \frac{\partial h_3}{\partial s} & \frac{\partial h_4}{\partial s} \end{bmatrix}$$

(3) Evaluation of partial derivatives of the interpolation functions:

$$\left.\begin{aligned} \frac{\partial h_1}{\partial r} &= \frac{1}{4}(1+s) & \frac{\partial h_1}{\partial s} &= \frac{1}{4}(1+r) \\ \frac{\partial h_2}{\partial r} &= -\frac{1}{4}(1+s) & \frac{\partial h_2}{\partial s} &= \frac{1}{4}(1+r) \\ \frac{\partial h_3}{\partial r} &= -\frac{1}{4}(1-s) & \frac{\partial h_3}{\partial s} &= -\frac{1}{4}(1-r) \\ \frac{\partial h_4}{\partial r} &= \frac{1}{4}(1-s) & \frac{\partial h_4}{\partial s} &= -\frac{1}{4}(1-r) \end{aligned}\right\} \tag{3-48}$$

(4) Numerical integration:

By using 3 points Gaussian quadrature rule, the stiffness matrix is calculated numerically as follows:

$$K = t \int_{-1}^{1} \int_{-1}^{1} B_{(x(r,s),y(r,s))}{}^{T} D B_{(x(r,s),y(r,s))} \frac{\partial(x,y)}{\partial(r,s)} drds$$

$$K = t \int_{-1}^{1} \int_{-1}^{1} F_{(r,s)} drds$$

$$K = t \sum_{i=1}^{3} \sum_{j=1}^{3} w_i w_j F_{(r_i,s_j)} \tag{3-49}$$

Where:

$$F_{(r,s)} = B_{(x(r,s),y(r,s))}{}^{T} D B_{(x(r,s),y(r,s))} \frac{\partial(x,y)}{\partial(r,s)}$$

$$w_1 = \frac{5}{9} = 0.5556 \quad , \quad w_2 = \frac{8}{9} = 0.8889 \quad , \quad w_3 = \frac{5}{9} = 0.5556$$

$$r_1 = s_1 = -\sqrt{3/5} = -0.7746 \quad , \quad r_2 = s_2 = 0 \quad , \quad r_3 = s_3 = \sqrt{3/5} = 0.7746$$

(5) Assemble of finite element:

The total stiffness matrix can be obtained assembling the stiffness matrix over the area of all finite elements.

$$K = \sum_{m} K_m \tag{3-50}$$

Where m denotes the m-th element.

3.8 Stress and strain at Gaussian points

The process to calculate the stress and strain at Gaussian points [4][8][31] is summarized below:

(1) Stress and strain t Gaussian points:

By using 3-points Gaussian Integration Method in a single 4-nodes isoparametric element, there are 9 Gaussian points as is shown in Figure 3-12.

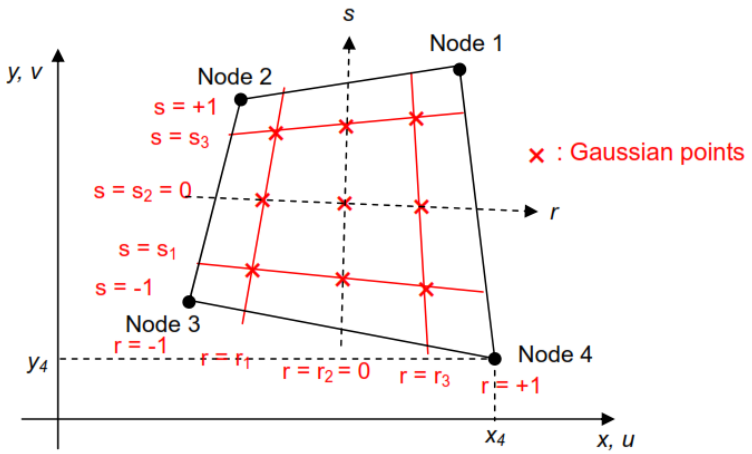

Figure 3-12 4-nodes isoparametric element with 9 Gaussian points

The stress and strain at the Gaussian points, (r_i, s_j), is obtained from Equation (3-34) and Equation (3-36) as follows:

$$\left.\begin{aligned} \sigma_{ij} &= \begin{Bmatrix} \sigma_x \\ \sigma_y \\ \tau_{xy} \end{Bmatrix}_{ij} = DB_{ij}U \\ \varepsilon_{ij} &= \begin{Bmatrix} \varepsilon_x \\ \varepsilon_y \\ \gamma_{xy} \end{Bmatrix}_{ij} = B_{ij}U \end{aligned}\right\} \tag{3-51}$$

(2) Principal stress at Gaussian points:

$$\left.\begin{aligned} \sigma_1 &= \frac{\sigma_x + \sigma_y}{2} + \sqrt{\left(\frac{\sigma_x - \sigma_y}{2}\right)^2 + {\tau_{xy}}^2} \\ \sigma_2 &= \frac{\sigma_x + \sigma_y}{2} - \sqrt{\left(\frac{\sigma_x - \sigma_y}{2}\right)^2 + {\tau_{xy}}^2} \\ \theta_p &= \frac{1}{2} arctan\left(\frac{2\tau_{xy}}{\sigma_x - \sigma_y}\right) \end{aligned}\right\} \tag{3-52}$$

Case 1: $\tau_{xy} > 0$ and $\sigma_x > \sigma_y$ (See Figure 3-13). For this case, the range of arctan is [-π/2, π/2], and $2\theta_p$ is in this range.

Case 2: $\tau_{xy} < 0$ and $\sigma_x > \sigma_y$ (See Figure 3-14). For this case, the range of arctan is [-π/2, π/2], and $2\theta_p$ is in this range.

Case 3: $\tau_{xy} > 0$ and $\sigma_x < \sigma_y$ (See Figure 3-15). For this case, the range of arctan is [-π/2, π/2], and $2\theta_p$ is not in this range. So the angle must be $2\theta_p = \pi - |arctan|$.

Case 4: $\tau_{xy} < 0$ and $\sigma_x < \sigma_y$ (See Figure 3-16). For this case, the range of arctan is [-π/2, π/2], and $2\theta_p$ is not in this range. So the angle must be $2\theta_p = |arctan| - \pi$.

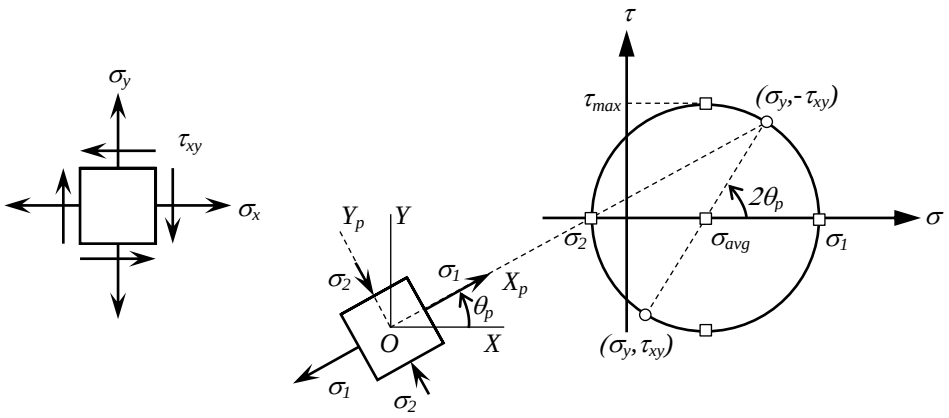

Figure 3-13 Case 1: $\tau_{xy} > 0$ and $\sigma_x > \sigma_y$

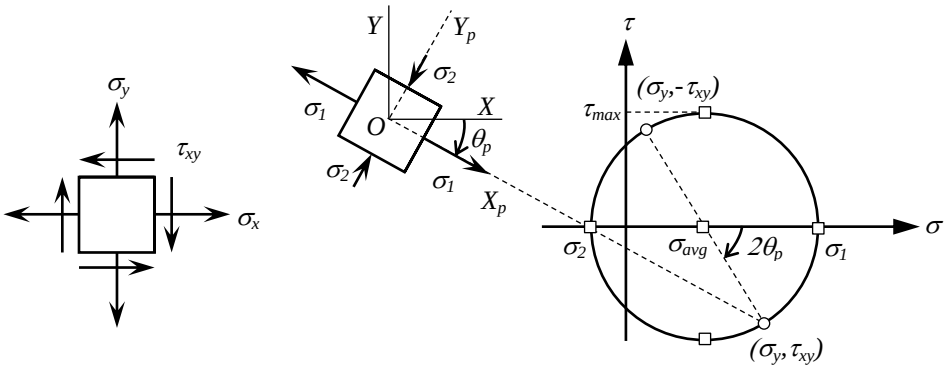

Figure 3-14 Case 2: $\tau_{xy} < 0$ and $\sigma_x > \sigma_y$

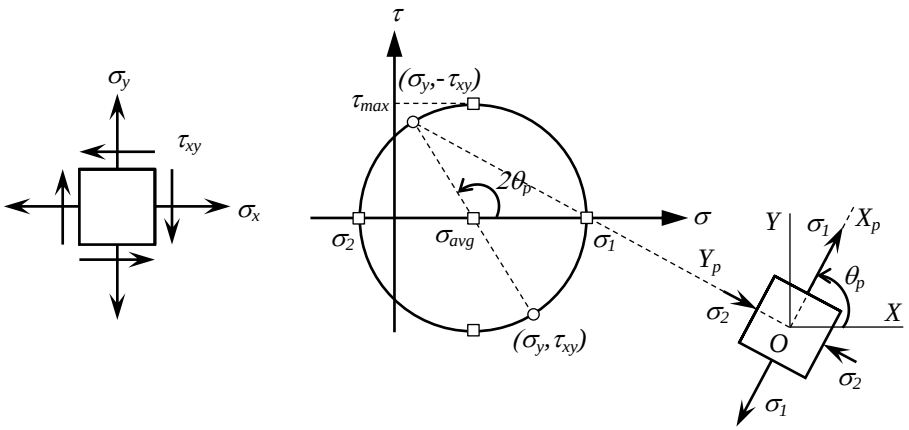

Figure 3-15 Case 3: $\tau_{xy} > 0$ and $\sigma_x < \sigma_y$

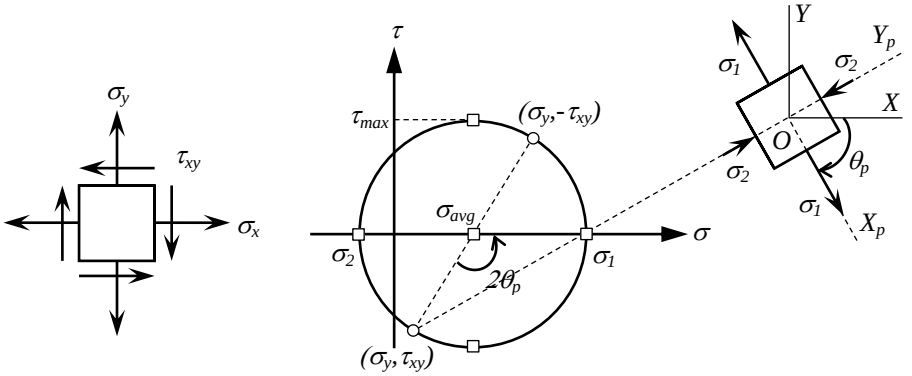

Figure 3-16 Case 4: $\tau_{xy} < 0$ and $\sigma_x < \sigma_y$

(3) Displacement at Gaussian points:

After obtaining the nodal displacement, the displacement at the Gaussian point, (r_i, s_j), is obtained from Equation (3-31) as follows:

$$\left.\begin{aligned} u_{(r_i,s_j)} &= \sum_{i=1}^{4} h_{i(r_i,s_j)} u_i \\ v_{(r_i,s_j)} &= \sum_{i=1}^{4} h_{i(r_i,s_j)} v_i \end{aligned}\right\} \tag{3-53}$$

3.9 Incompatible element

In an ideal situation, a beam under a pure bending moment experiences a curved shape change. The angle between the curved horizontal dotted line and the straight vertical line remains at 90 degree after bending as is shown in Figure 3-17. Therefore, no shear strain occurs inside a material. [4][8][31]

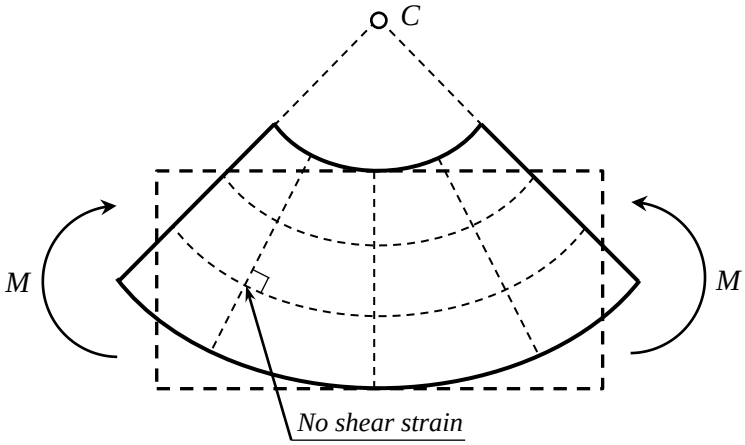

Figure 3-17 Beam under pure bending moment

To model the ideal shape change, an element should have the ability to assume the curved shape. As is shown in Figure 3-18, the second order element with eight nodes enables to represent the curved shape. On the contrary, the first order element is not able to bend to curves and all dotted lines remain straight and the angle is no longer than 90 degree. To cause the angle to change under pure moment, an incorrect artificial shear strain and stress have been introduced. Therefore, the strain energy of the element is larger than ideal situation. As we demonstrated in the principle of virtual work method, overestimate of strain energy causes overestimate of stiffness matrix. This is the reason that the first order element with four nodes becomes overly stiff under the bending moment. This problem is called shear locking.

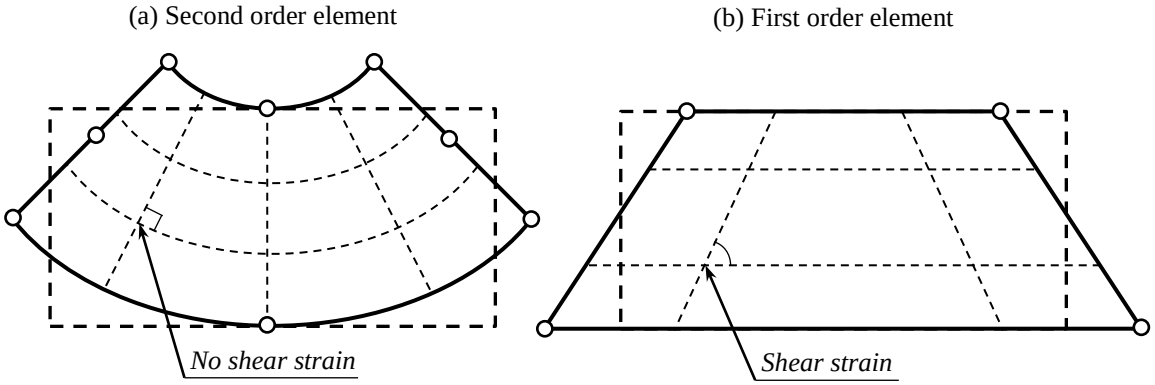

Figure 3-18 First and second order element

To solve the problem in the first order element, we introduce the new displacement shape functions (Equation (3-54)) to add curved displacement modes as is shown in Figure 3-19.

$$\left.\begin{aligned} u_{(r,s)} &= \sum_{i=1}^{4} h_{i(r,s)} u_i + (1-r^2)\alpha_1 + (1-s^2)\alpha_2 \\ v_{(r,s)} &= \sum_{i=1}^{4} h_{i(r,s)} v_i + (1-r^2)\alpha_3 + (1-s^2)\alpha_4 \end{aligned}\right\} \tag{3-54}$$

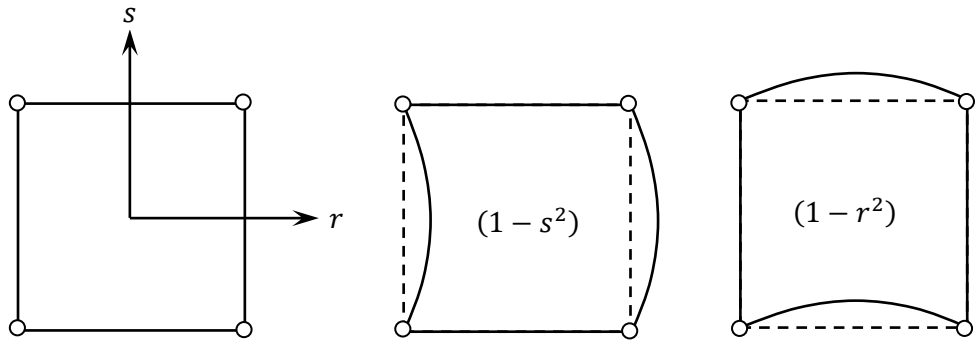

Figure 3-19 Second order shape function

It can avoid over stiff in bending; however there might be incompatibility of deformation at the boundary between two elements. Therefore, this element is called incompatible element.

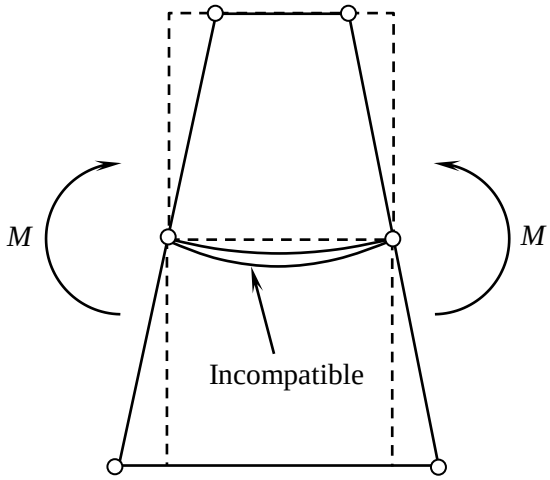

Figure 3-20 Incompatible element

Writing Equation (3-54) in matrix notation:

$$u_{(r,s)} = H_{(r,s)}U + G_{(r,s)}A \tag{3-55}$$

Where:

$$H = \begin{bmatrix} h_1 & 0 & h_2 & 0 & h_3 & 0 & h_4 & 0 \\ 0 & h_1 & 0 & h_2 & 0 & h_3 & 0 & h_4 \end{bmatrix}$$

$$G = \begin{bmatrix} g_1 & g_2 & 0 & 0 \\ 0 & 0 & g_1 & g_2 \end{bmatrix} \quad , \quad g_1 = (1 - r^2) \quad , \quad g_2 = (1 - s^2)$$

$$U = \begin{Bmatrix} u_1 \\ v_1 \\ u_2 \\ v_2 \\ u_3 \\ v_3 \\ u_4 \\ v_4 \end{Bmatrix} \quad , \quad A = \begin{Bmatrix} \alpha_1 \\ \alpha_2 \\ \alpha_3 \\ \alpha_4 \end{Bmatrix}$$

Stiffness matrix on incompatible element can be obtained from the Principle of Virtual Work Method, which is expressed in the following form:

$$\int_V \bar{\varepsilon}^T \sigma dv = \bar{U}^T F \tag{3-56}$$

Where, $\bar{\varepsilon}$ is a virtual strain vector, σ is a stress vector, $\bar{U}$ is a virtual displacement vector and F is a load vector, respectively.

The strain vector is calculated from the nodal displacement vector as follows:

$$\begin{Bmatrix}\varepsilon_x\\ \varepsilon_y\\ \gamma_{xy}\end{Bmatrix}=\begin{Bmatrix}\dfrac{\partial u}{\partial x}\\ \dfrac{\partial v}{\partial y}\\ \dfrac{\partial u}{\partial y}+\dfrac{\partial v}{\partial x}\end{Bmatrix}=\begin{Bmatrix}\displaystyle\sum_{i=1}^{4}\frac{\partial h_i}{\partial x}u_i+\frac{\partial g_1}{\partial x}\alpha_1+\frac{\partial g_2}{\partial x}\alpha_2\\ \displaystyle\sum_{i=1}^{4}\frac{\partial h_i}{\partial y}v_i+\frac{\partial g_1}{\partial y}\alpha_3+\frac{\partial g_2}{\partial y}\alpha_4\\ \displaystyle\sum_{i=1}^{4}\frac{\partial h_i}{\partial y}u_i+\frac{\partial g_1}{\partial y}\alpha_1+\frac{\partial g_2}{\partial y}\alpha_2+\sum_{i=1}^{4}\frac{\partial h_i}{\partial x}v_i+\frac{\partial g_1}{\partial x}\alpha_3+\frac{\partial g_2}{\partial x}\alpha_4\end{Bmatrix}$$

$$\begin{Bmatrix}\varepsilon_x\\ \varepsilon_y\\ \gamma_{xy}\end{Bmatrix}=\begin{bmatrix}\dfrac{\partial h_1}{\partial x} & 0 & \dfrac{\partial h_2}{\partial x} & 0 & \dfrac{\partial h_3}{\partial x} & 0 & \dfrac{\partial h_4}{\partial x} & 0\\ 0 & \dfrac{\partial h_1}{\partial y} & 0 & \dfrac{\partial h_2}{\partial y} & 0 & \dfrac{\partial h_3}{\partial y} & 0 & \dfrac{\partial h_4}{\partial y}\\ \dfrac{\partial h_1}{\partial y} & \dfrac{\partial h_1}{\partial x} & \dfrac{\partial h_2}{\partial y} & \dfrac{\partial h_2}{\partial x} & \dfrac{\partial h_3}{\partial y} & \dfrac{\partial h_3}{\partial x} & \dfrac{\partial h_4}{\partial y} & \dfrac{\partial h_4}{\partial x}\end{bmatrix}\begin{Bmatrix}u_1\\ v_1\\ u_2\\ v_2\\ u_3\\ v_3\\ u_4\\ v_4\end{Bmatrix}+\begin{bmatrix}\dfrac{\partial g_1}{\partial x} & \dfrac{\partial g_2}{\partial x} & 0 & 0\\ 0 & 0 & \dfrac{\partial g_1}{\partial y} & \dfrac{\partial g_2}{\partial y}\\ \dfrac{\partial g_1}{\partial y} & \dfrac{\partial g_2}{\partial y} & \dfrac{\partial g_1}{\partial x} & \dfrac{\partial g_2}{\partial x}\end{bmatrix}\begin{Bmatrix}\alpha_1\\ \alpha_2\\ \alpha_3\\ \alpha_4\end{Bmatrix}$$

$$\varepsilon = BU + GA \tag{3-57}$$

In the plane stress problem, the stress-strain relationship is expressed as:

$$\begin{Bmatrix}\sigma_x\\ \sigma_y\\ \tau_{xy}\end{Bmatrix}=\frac{\mathrm{E}}{1-\nu^2}\begin{bmatrix}1 & \nu & 0\\ \nu & 0 & 0\\ 0 & 0 & \dfrac{1-\nu}{2}\end{bmatrix}\begin{Bmatrix}\varepsilon_x\\ \varepsilon_y\\ \gamma_{xy}\end{Bmatrix} \tag{3-58}$$

$$\sigma \;=\; D \;\; \varepsilon$$

Substituting Equation (3-57) into Equation (3-58):

$$\sigma = D(BU + GA) \tag{3-59}$$

From the Principle of Virtual Work Method:

$$\int_V \left(B\overline{U} + G\overline{A}\right)^T D(BU + GA)dv$$

$$= \overline{U}^T\left(\int_V B^T DBdv\right)U + \overline{U}^T\left(\int_V B^T DGdv\right)A + \overline{A}^T\left(\int_V G^T DBdv\right)U + \overline{A}^T\left(\int_V G^T DGdv\right)A$$

$$= \overline{U}^T F \tag{3-60}$$

Equation (3-60) can be written in matrix notation form as follows:

$$[\overline{U}^T \quad \overline{A}^T] = \begin{bmatrix} \int_V B^T DBdv & \int_V B^T DGdv \\ \int_V G^T DBdv & \int_V G^T DGdv \end{bmatrix} \begin{bmatrix} U \\ A \end{bmatrix} = [\overline{U}^T \quad \overline{A}^T] \begin{bmatrix} F \\ 0 \end{bmatrix}$$

Therefore, the equilibrium equation is obtained as :

$$\begin{bmatrix} K_{UU} & K_{UA} \\ K_{AU} & K_{AA} \end{bmatrix} \begin{bmatrix} U \\ A \end{bmatrix} = \begin{bmatrix} F \\ 0 \end{bmatrix} \tag{3-61}$$

Where:

$$K_{UU} = \int_V B^T DBdv \quad , \quad K_{UA} = \int_V B^T DGdv$$

$$K_{AU} = \int_V G^T DBdv \quad , \quad K_{AA} = \int_V G^T DGdv$$

From Equation (3-61), it is possible to eliminate the incompatible displacement modes as follows:

$$\begin{aligned} K_{AU}U + K_{AA}A &= 0 \\ A &= -{K_{AA}}^{-1}K_{AU}U \end{aligned} \tag{3-62}$$

Then, the element stiffness matrix is given by:

$$\begin{aligned} F &= KU \\ K &= K_{UU} - K_{UA}{K_{AA}}^{-1}K_{AU} \end{aligned} \tag{3-63}$$

The process is summarized as follows:

(1) Evaluation of Jacobian matrix:

$$J = \begin{bmatrix} \frac{\partial x}{\partial r} & \frac{\partial y}{\partial r} \\ \frac{\partial x}{\partial s} & \frac{\partial x}{\partial s} \end{bmatrix} = \begin{bmatrix} \sum_{i=1}^{4} \frac{\partial h_i}{\partial r} x_i & \sum_{i=1}^{4} \frac{\partial h_i}{\partial r} y_i \\ \sum_{i=1}^{4} \frac{\partial h_i}{\partial s} x_i & \sum_{i=1}^{4} \frac{\partial h_i}{\partial s} y_i \end{bmatrix} \tag{3-64}$$

(2) Evaluation of G matrix. From Equation (3-57):

$$G = \begin{bmatrix} \frac{\partial g_1}{\partial x} & \frac{\partial g_2}{\partial x} & 0 & 0 \\ 0 & 0 & \frac{\partial g_1}{\partial y} & \frac{\partial g_2}{\partial y} \\ \frac{\partial g_1}{\partial y} & \frac{\partial g_2}{\partial y} & \frac{\partial g_1}{\partial x} & \frac{\partial g_2}{\partial x} \end{bmatrix} \tag{3-65}$$

Where the derivatives $\left(\frac{\partial g_1}{\partial x}, \frac{\partial g_2}{\partial x}, \frac{\partial g_1}{\partial y}, \frac{\partial g_2}{\partial y}\right)$ are calculated as follows:

$$\frac{\partial g_1}{\partial x} = \frac{\partial g_1}{\partial r}\frac{\partial r}{\partial x} + \frac{\partial g_1}{\partial s}\frac{\partial s}{\partial x} \quad , \quad \frac{\partial g_2}{\partial x} = \frac{\partial g_2}{\partial r}\frac{\partial r}{\partial x} + \frac{\partial g_2}{\partial s}\frac{\partial s}{\partial x}$$
$$\frac{\partial g_1}{\partial y} = \frac{\partial g_1}{\partial r}\frac{\partial r}{\partial y} + \frac{\partial g_1}{\partial s}\frac{\partial s}{\partial y} \quad , \quad \frac{\partial g_2}{\partial y} = \frac{\partial g_2}{\partial r}\frac{\partial r}{\partial y} + \frac{\partial g_2}{\partial s}\frac{\partial s}{\partial y}$$

In matrix form:

$$\begin{bmatrix} \frac{\partial g_1}{\partial x} & \frac{\partial g_2}{\partial x} \\ \frac{\partial g_1}{\partial y} & \frac{\partial g_2}{\partial y} \end{bmatrix} = \begin{bmatrix} \frac{\partial r}{\partial x} & \frac{\partial s}{\partial x} \\ \frac{\partial r}{\partial y} & \frac{\partial s}{\partial y} \end{bmatrix} \begin{bmatrix} \frac{\partial g_1}{\partial r} & \frac{\partial g_2}{\partial r} \\ \frac{\partial g_1}{\partial s} & \frac{\partial g_2}{\partial s} \end{bmatrix} = J^{-1} \begin{bmatrix} \frac{\partial g_1}{\partial r} & \frac{\partial g_2}{\partial r} \\ \frac{\partial g_1}{\partial s} & \frac{\partial g_2}{\partial s} \end{bmatrix} \tag{3-66}$$

(3) Evaluation of partial derivatives of the interpolation functions:

$$\left.\begin{array}{ll} \frac{\partial g_1}{\partial r} = -2r & , \quad \frac{\partial g_1}{\partial s} = 0 \\ \frac{\partial g_2}{\partial r} = 0 & , \quad \frac{\partial g_2}{\partial s} = -2s \end{array}\right\} \tag{3-67}$$

(4) Numerical integration:

Using the 3-points Gaussian quadrature rule, the stiffness matrices are calculated numerically as follows:

$$\left.\begin{array}{l} K_{UU} = t\sum_{i=1}^{3}\sum_{j=1}^{3} w_i w_j F_{UU(r_i,s_j)} \\ K_{UA} = t\sum_{i=1}^{3}\sum_{j=1}^{3} w_i w_j F_{UA(r_i,s_j)} \\ K_{AU} = t\sum_{i=1}^{3}\sum_{j=1}^{3} w_i w_j F_{AU(r_i,s_j)} \\ K_{AA} = t\sum_{i=1}^{3}\sum_{j=1}^{3} w_i w_j F_{AA(r_i,s_j)} \end{array}\right\} \tag{3-68}$$

Where:

$$F_{UU(r,s)} = B_{(x_{(r,s)},y_{(r,s)})}{}^{T} D B_{(x_{(r,s)},y_{(r,s)})} \frac{\partial(x,y)}{\partial(r,s)}$$
$$F_{UA(r,s)} = B_{(x_{(r,s)},y_{(r,s)})}{}^{T} D G_{(x_{(r,s)},y_{(r,s)})} \frac{\partial(x,y)}{\partial(r,s)}$$
$$F_{AU(r,s)} = G_{(x_{(r,s)},y_{(r,s)})}{}^{T} D B_{(x_{(r,s)},y_{(r,s)})} \frac{\partial(x,y)}{\partial(r,s)}$$
$$F_{AA(r,s)} = G_{(x_{(r,s)},y_{(r,s)})}{}^{T} D G_{(x_{(r,s)},y_{(r,s)})} \frac{\partial(x,y)}{\partial(r,s)}$$

$$w_1 = \frac{5}{9} = 0.5556 \quad , \quad w_2 = \frac{8}{9} = 0.8889 \quad , \quad w_3 = \frac{5}{9} = 0.5556$$

$$r_1 = s_1 = -\sqrt{3/5} = -0.7746 \quad , \quad r_2 = s_2 = 0 \quad , \quad r_3 = s_3 = \sqrt{3/5} = 0.7746$$

Then, the element stiffness matrix is calculated as:

$$\begin{aligned} F &= KU \\ K &= K_{UU} - K_{UA} K_{AA}{}^{-1} K_{AU} \end{aligned} \tag{3-69}$$

(5) Assemble of finite element:

The total stiffness matrix can be obtained assembling the stiffness matrix over the area of all finite elements.

$$K = \sum_{m} K_m \tag{3-70}$$

Where m denotes the m-th element.

(6) Strain and stress at Gaussian point:

Strain at Gaussian points can be obtained from Equations (3-57) and (3-62):

$$\varepsilon = BU + GA = \left(B - G K_{AA}{}^{-1} K_{AU}\right) U \tag{3-71}$$

Similarly, stress at Gaussian points can be obtained from:

$$\sigma = D\varepsilon = \left(DB - DG K_{AA}{}^{-1} K_{AU}\right) U \tag{3-72}$$

CHAPTER 4

EXPERIMENTAL TEST

CHAPTER 4 : EXPERIMENTAL TESTS

In recent years, large scale construction of medium-rise building that use low ductility reinforced concrete (LDRC) wall has become commonplace in Peru To improve seismic response of reinforced concrete (RC) buildings against earthquakes, two verification tests were conducted on LDRC walls, wall with and without carbon fiber sheet (CFS) as a retrofitting method. The first experiment was conducted in 2013 at the Toyohashi University of Technology (TUT), Japan on three LDRC walls [13][20][40], the first wall was without CFS reinforcement, the second wall was wrapped completely with CFS and the third wall was wrapped with CFS at the edges only. A second experiment was conducted in 2014 at TUT on three LDRC walls, following the same retrofitted pattern of the first experiment but with a partial retrofitting with CFS to a specified height. [21][35]

From those tests, it was verified that the carbon fiber sheets delay the concrete crushing of the wall base that occurs during flexural failure and that deformation capacity was improved. Moreover, during the test with the retrofitted walls it was observed that the crushing of the concrete produces bulges at the base corners of the wall. Additionally, when the maximum strain on the CFS is reached, the carbon fiber sheet over the crushed concrete area fails suddenly.

In order to verify the confinement effect of the carbon fiber sheet used as a retrofitting method for concrete, a third experiment was conducted in 2015 at TUT using concrete samples with or without CFS subjected under compressive loading (monotonic and cyclic), by changing the size, shape and number of CFS layers. [27][35]

From the third experiment, it was confirmed that deformation performance was improved and that strength of the concrete was increased due to the confinement provided by the CFS, however the stress-strain relationship of concrete with CFS depends on the shape of the concrete sample.

4.1 LDRC shear walls retrofitted with full height of CFS

4.1.1 Design of specimen

Three LDRC wall specimens were tested. The test specimen characteristics for each wall are shown in Table 4-1. The material properties of concrete, reinforcing steel and carbon fiber sheet are shown in Table 4-2, Table 4-3 and Table 4-4 respectively.

Table 4-1 Test specimen characteristics

Wall	WF	RWF1	RWF2
$l_w \times h_w$ (mm):	1600 × 1600		
Wall thickness, t_w (mm):	80		
Vertical reinforcement at boundary ends:	3-D13		
Wall mesh reinforcement:	D6@150, single ($p_w = 0.27\%$)		
Retrofitting Mode (mm):	Non-retrofitted	Over wall span L = 1600	Both boundary ends L = 400/side

Table 4-2 Concrete material properties

Specimen	σ_B (N/mm^2)	E_c (N/mm^2)	ε_{c0} (%)	f_t (N/mm^2)	Age (days)
WF	33.5	26800	0.228	3.0	54
RWF1	35.2	26400	0.256	2.9	62
RWF2	29.8	27200	0.215	2.9	67

σ_B: Compressive strength, E_c: Modulus of elasticity
ε_{c0}: Strain at compressive strength, f_t: Tensile strength by split cylinder test

Table 4-3 Reinforcing steel material properties

Name (Property)	σ_y (N/mm^2)	σ_u (N/mm^2)	E_s (N/mm^2)	Usage
D6 (SD295A)	359	474	174600	Wall mesh reinforcement
D13 (SD295A)	355	516	182100	Vertical reinforcement at boundary ends

σ_y: Yielding strength, σ_u: Ultimate tensile strength, E_s Modulus of elasticity

Table 4-4 CFS material properties

Fiber weight:	300	g/m^3
Sheet thickness:	0.167	mm
Density:	1.80	g/m^3
Tensile strength:	3.4	kN/mm^2
Modulus of elasticity:	230	kN/mm^2
Rupture strain:	1.478	%
Width:	330	mm

Figure 4-1 shows the arrangement of the reinforcing steel bars for all the specimens tested. WF corresponds to the wall without CFS, RWF1 corresponds to the wall retrofitted with CFS by wrapping the entire wall span and RWF2 corresponds to the wall retrofitted with CFS by wrapping both lateral ends of the wall as is shown in Figure 4-2.

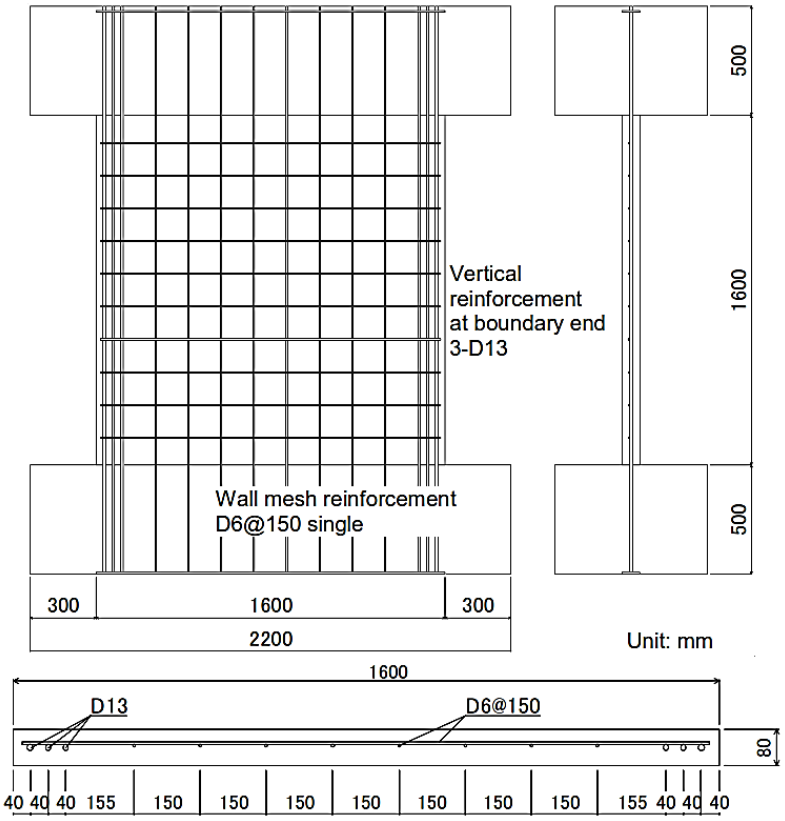

Figure 4-1 Reinforcing bar arrangement

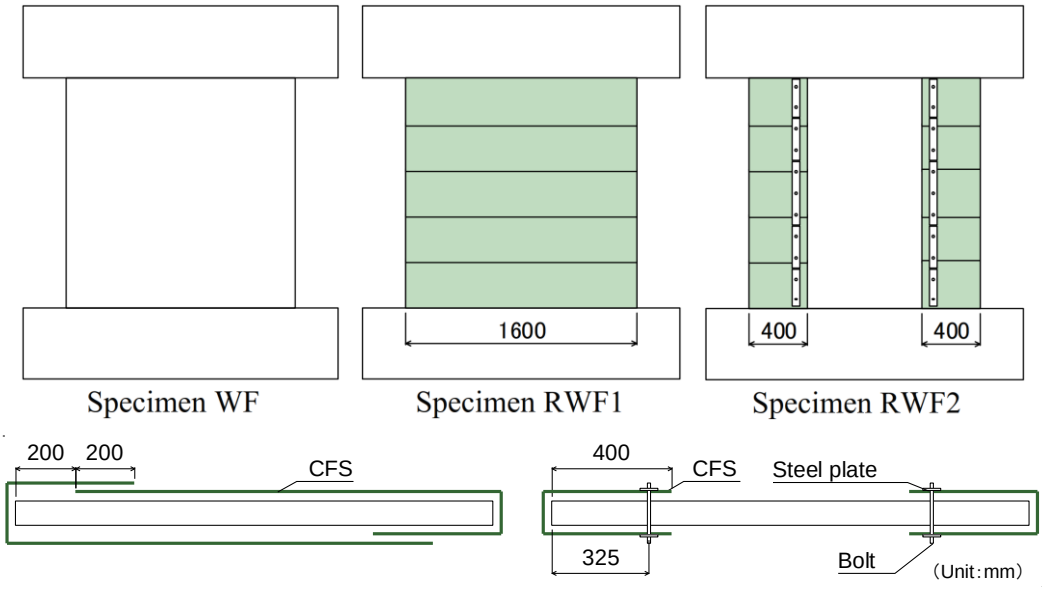

Figure 4-2 Test specimens

To attach the CFS, the corners of the walls were chamfered to a diameter of 24mm, epoxy resin was first applied to the wall surface, the CFS was then attached while maintaining tension manually and with a roller, and then epoxy resin was further applied on top with a roller to impregnate the CFS. Moreover, the top and bottom sheets were overlapped by 12.5mm each. For specimen RWF2, the CFS was fixed by steel plates (PL-4.5) and threaded bolts (M10) as shown in Figure 4-2. The threaded bolts were installed into drilled hole after concrete casting and threaded bolts were tightened without management of tightening torque of bolts.

4.1.2 Outline of loading test

A description of the loading device is presented in Figure 4-3. A horizontal lateral force applied in cycles over the positive and negative directions was used for the loading. Also, a constant axial load of 343kN (Equation (4-1)) was applied at the top of the specimen using a couple of vertical hydraulic jacks. Where, used F_c of compressive strength of concrete was 33.5 N/mm^2 in this calculation.

$$N = 0.08 l_w t_w F_c \tag{4-1}$$

Additional moment was applied at the top of the specimen by controlling these vertical jacks to correspond to the acting shear force, such that the shear span ratio was 1.5, using the following equations.

$$N_E = \frac{N}{2} \pm \frac{Q}{l}(h_s - a)$$
$$N_W = \frac{N}{2} \mp \frac{Q}{l}(h_s - a) \tag{4-2}$$

Where, N_E: axial force of east side jack, N_W: axial force of west side jack, N: constant axial force, Q: lateral load, l: distance between two vertical jacks, h_s: assumed height of applied lateral load, and a: actual height of applied lateral load.

In the experiment, the horizontal displacement δ measured at the top stub, divided by the height of the measurement point h (1985 mm), was controlled through the drift angle of the member $R = \delta / h$. The loading cycle started with one cycle of R = 1/800 rad, and then two cycles each of R = 1/400, 1/200, 1/133, 1/100, 1/67, 1/50 and 1/33 rad, as is shown in Table 4-5.

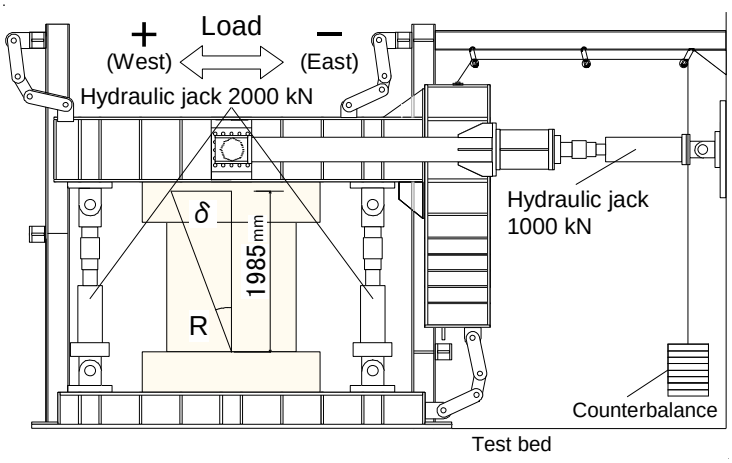

Figure 4-3 Loading apparatus

Table 4-5 Loading pattern

R	R (%)	δ (mm)	Number of cycles
1/800	0.125	2.48	1
1/400	0.25	4.96	2
1/200	0.5	9.93	2
1/133	0.75	14.93	2
1/100	1.0	19.85	2
1/67	1.5	29.63	2
1/50	2.0	39.70	2
1/33	3.0	60.15	2

4.1.3 Measuring method

In the tests, the horizontal displacement was measured at the top of the wall and along with the boundary ends of wall. The vertical deformation was measured along the boundary ends of the wall and over the wall base. The diagonal deformation was measured from the top corner to the opposite bottom corner of the wall. Horizontal, vertical and diagonal deformation was measured using displacement transducers as is shown in Figure 4-4. Figure 4-5 shows the strain gauges distribution of the longitudinal and horizontal reinforcing steel bars of the wall. Besides, CFS was measured using strain gauges, the strain gauges setup on the CFS is shown in Figure 4-6. Additionally, the widths of cracks were measured using a crack scale at each loading cycle.

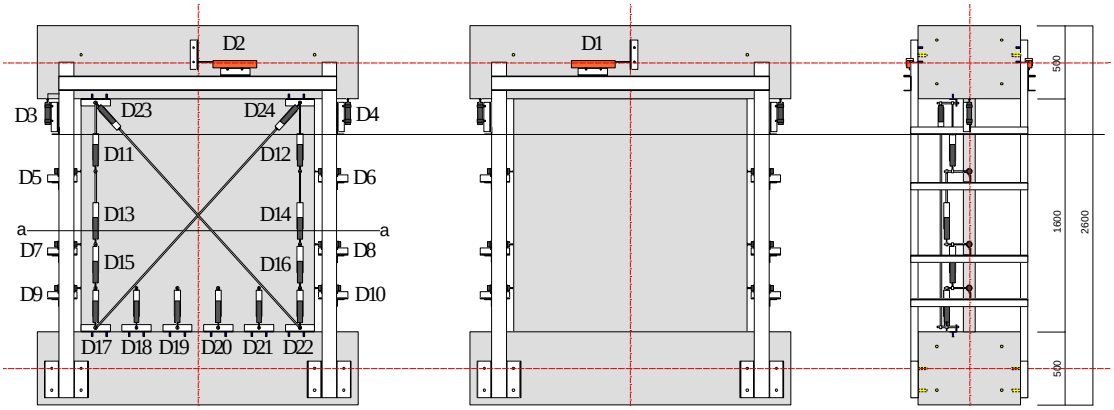

Figure 4-4 Horizontal, vertical and diagonal displacement transducers setup

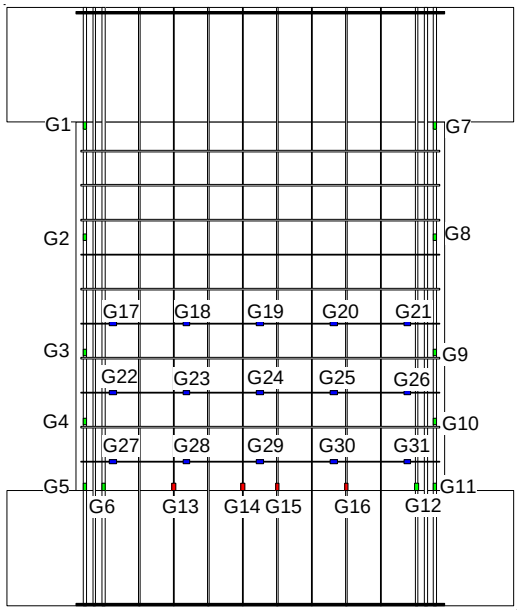

Figure 4-5 Strain gauges setup – Reinforcing steel bars

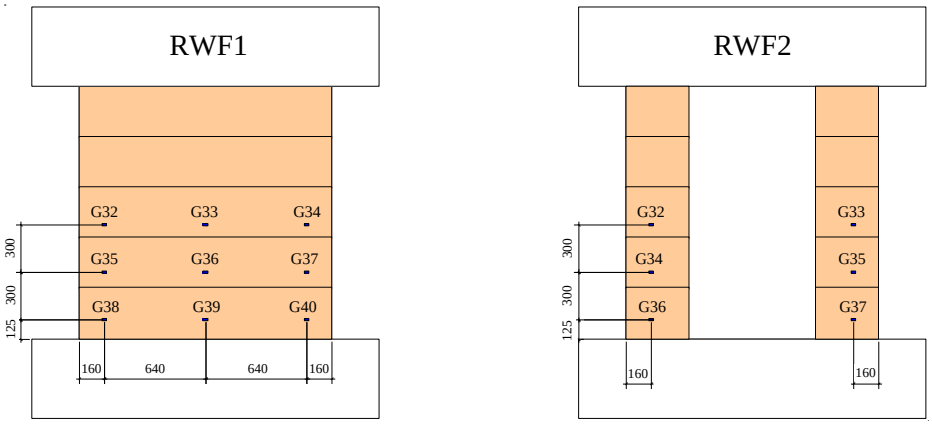

Figure 4-6 Strain gauges setup - CFS

4.1.4 Test result

The relationship between lateral load (Shear force) and drift angle for each specimen is shown in Figure 4-7.

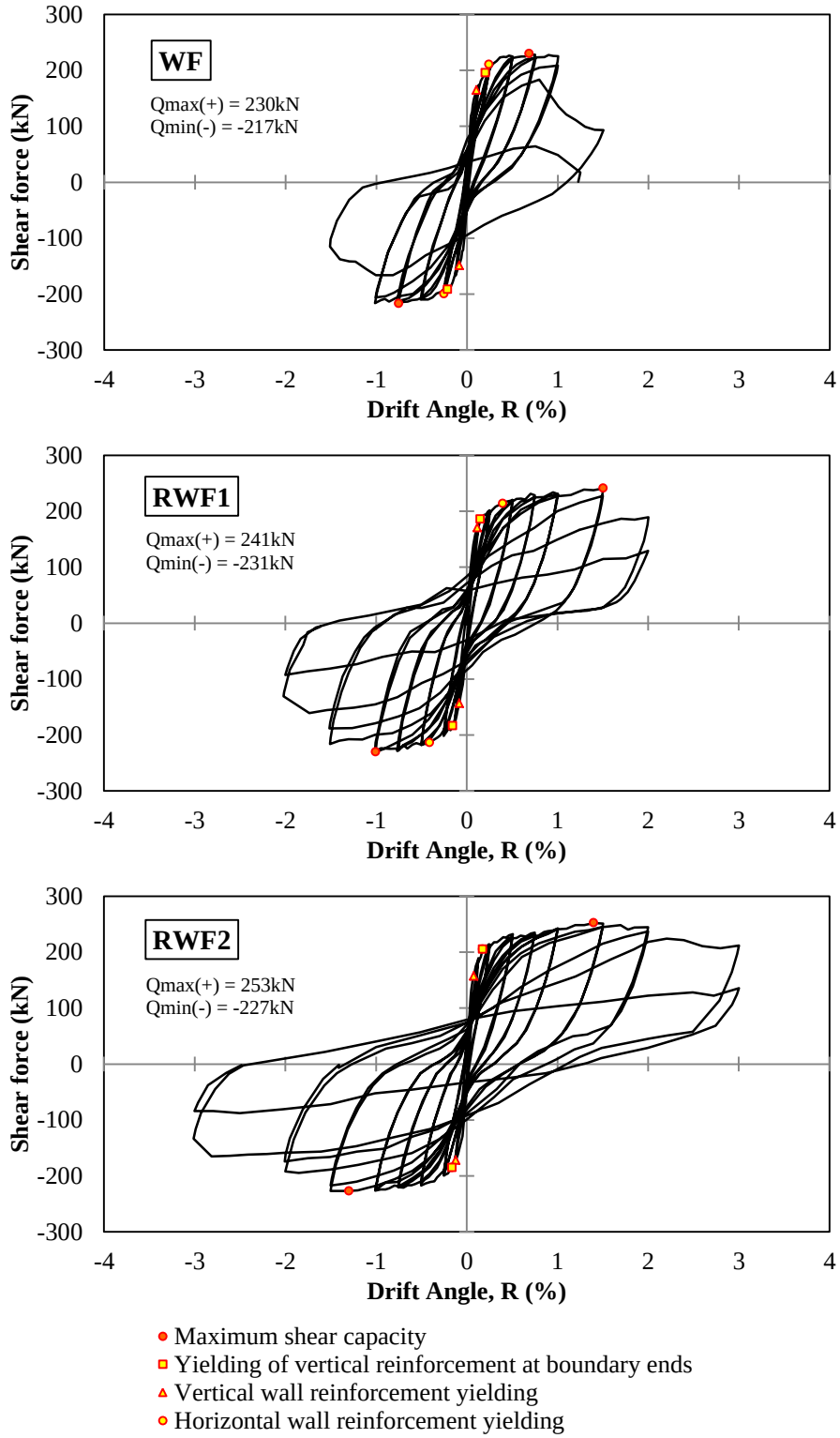

Figure 4-7 Lateral load and drift angle relationship

From experimental hysteretic curves of the three LDRC walls (WF, RWF1, and RWF2); the envelope curve (skeleton curve) for each specimen was found as is shown in Figure 4-8. Moreover, Figure 4-9 shows the comparison between the envelope curves of the tested walls.

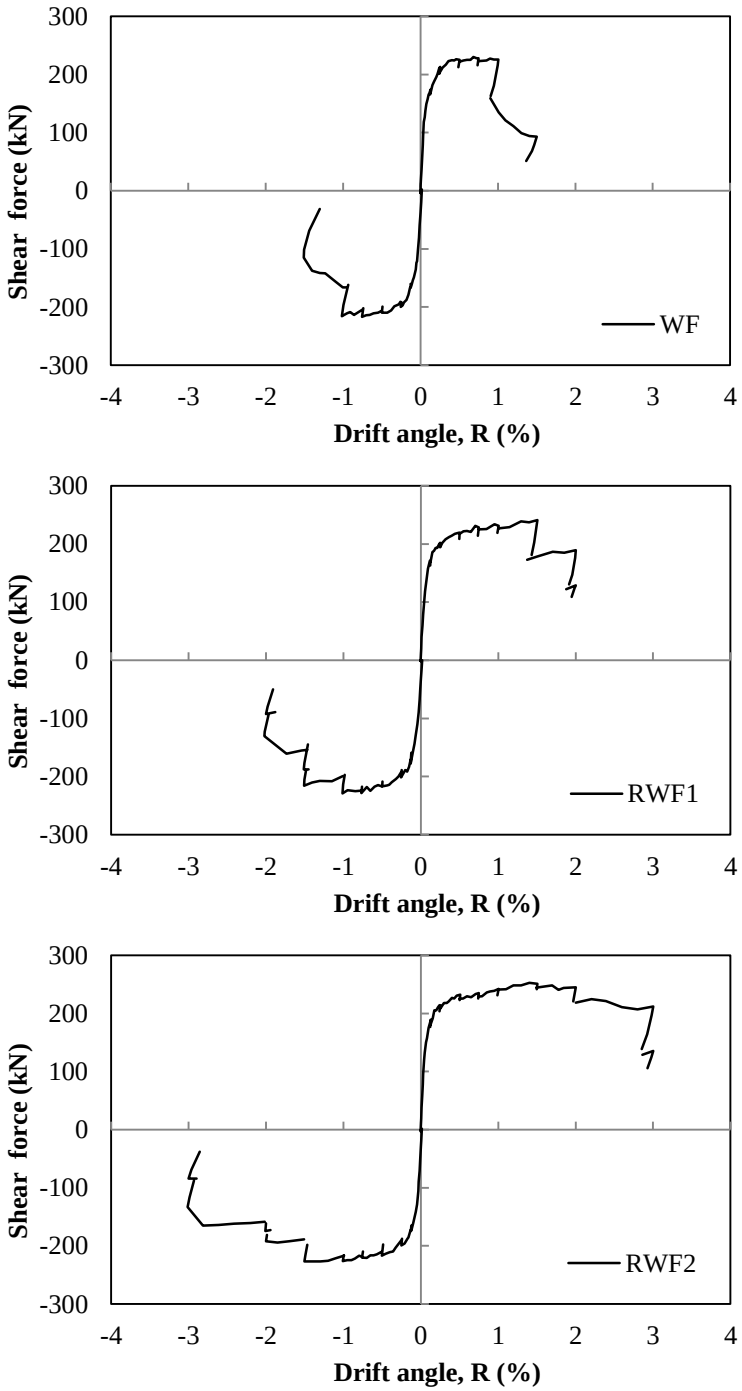

Figure 4-8 Experimental envelope curves

By comparing the envelope curves of the tested walls, it can be observed that the maximum strength remains about the same level, but most importantly, deformation capacity got improved, in both retrofitted walls, RWF1 and RWF2, in comparison with the non-retrofitted wall WF. Also it can be appreciated that wall RWF2 got larger deformation capacity than the wall RWF1, this could be explained due to the different retrofitted method, were RWF2, was retrofitted at the ends of the wall while RWF1 was retrofitted by wrapping the CFS over the entire span; both with full height of the wall retrofitted.

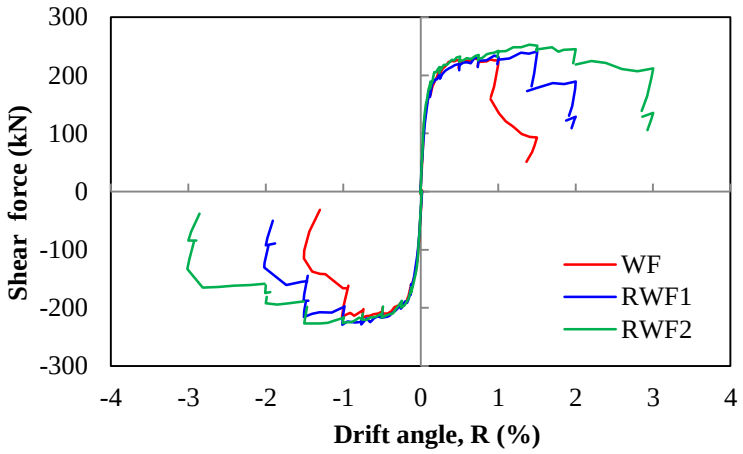

Figure 4-9 Comparison of experimental envelope curves

For specimen WF, shear cracks appeared at the same cycle that the vertical wall reinforcement yielded under the R=1/800 rad cycle, while the horizontal wall reinforcement and the vertical reinforcement at boundary ends yielded under the R=1/400 rad cycle. Afterwards, maximum capacity was reached at the R=1/133 rad cycle. Large concrete spalling at the lower part of the wall occurred under R=1/67 rad cycle. At which point the axial load could not be sustained and the loading was terminated. (See Figure 4-10)

Figure 4-10 Failure of specimen WF

For specimen RWF1, the vertical wall reinforcement yielded under the R=1/800 rad cycle while the vertical reinforcement at boundary ends yielded under the R=1/400 rad cycle, similar to specimen WF. The horizontal wall reinforcement were found to yield at the R=1/200 rad cycle. Afterwards, maximum capacity was reached at the R=1/67 rad cycle; at the R=1/50 rad cycle, concrete swelling at the wall base grew until swelling occurred at the center of the lower part of the wall as well. (See Figure 4-11)

Figure 4-11 Failure of specimen RWF1

For specimen RWF2, the vertical wall reinforcement yielded under the R=1/800 rad cycle while the horizontal wall reinforcement and the vertical reinforcement at boundary ends yielded under the R=1/400 rad cycle, similar to specimen WF. Afterwards, maximum capacity was reached at the R=1/67 rad cycle; large concrete spalling at the base occurred during the R=1/33 rad cycle. And then, right after starting with the R=1/25 rad cycle, the axial load could not be sustained and loading was terminated. Looking at the condition at the base during R=1/50 rad, it was found that the swelling was not as much as that of specimen RWF1. (See Figure 4-12)

Figure 4-12 Failure of specimen RWF2

4.2 LDRC shear walls retrofitted with partial height of CFS

4.2.1 Design of specimen

Three LDRC wall specimens were tested. The test specimen characteristics for each wall are shown in Table 4-6. The material properties of concrete, reinforcing steel and carbon fiber sheet are shown in Table 4-7, Table 4-8 and Table 4-9 respectively.

Table 4-6 Test specimens characteristics

Wall	WD	RWD1	RWD2
$l_w \times h_w$ (mm):	1600 × 1600		
Wall thickness, t_w (mm):	80		
Vertical reinforcement at boundary ends:	6-D10		
Hoop at boundary ends:	D4@120		
Wall mesh reinforcement:	D4@120, double ($p_w = 0.29\%$)		
Retrofitting Mode (mm):	Non-retrofitted	Over wall span L = 1600	Both boundary ends L = 400/side

Table 4-7 Concrete material properties

Specimen	σ_B (N/mm^2)	E_c (N/mm^2)	ε_{c0} (%)	f_t (N/mm^2)	Age (days)
WD	26.7	23700	0.220	2.7	37
RWD1	26.5	23000	0.225	2.5	42
RWD2	28.3	23800	0.250	3.0	53

σ_B: Compressive strength, E_c: Modulus of elasticity
ε_{c0}: Strain at compressive strength, f_t: Tensile strength by split cylinder test

Table 4-8 Reinforcing steel material properties

Name (Property)	σ_y (N/mm^2)	σ_u (N/mm^2)	E_s (N/mm^2)	Usage
D4	365	524	186000	Wall mesh and hoop reinforcement
D10	371	508	182000	Vertical reinforcement at boundary ends

σ_y: Yielding strength, σ_u: Ultimate tensile strength, E_s Modulus of elasticity

Table 4-9 CFS material properties

Fiber weight:	300	g/m^3
Sheet thickness:	0.167	mm
Density:	1.80	g/m^3
Tensile strength:	3.4	kN/mm^2
Modulus of elasticity:	230	kN/mm^2
Rupture strain:	1.478	%
Width:	330	mm

Figure 4-13 shows the arrangement of the reinforcing steel bars for all the specimens tested. WD corresponds to the wall without CFS, RWD1 corresponds to the wall retrofitted with CFS by wrapping the entire wall span and RWD2 corresponds to the wall retrofitted with CFS by wrapping both lateral ends of the wall as is shown in Figure 4-14. Both RWD1 and RWD2 were retrofitted partially in height with 650mm from the bottom of the wall.

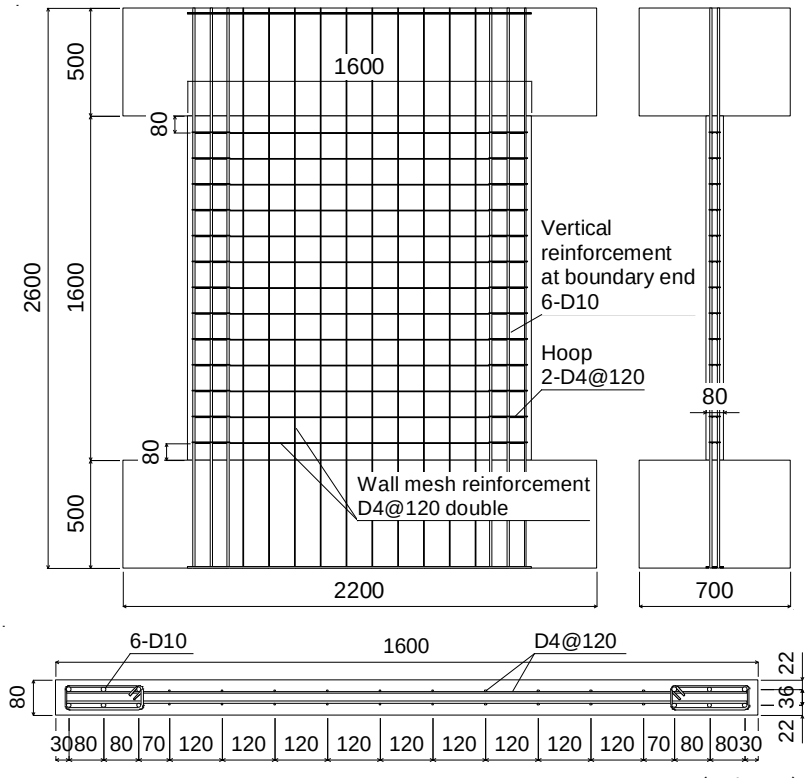

Figure 4-13 Reinforcing bar arrangement

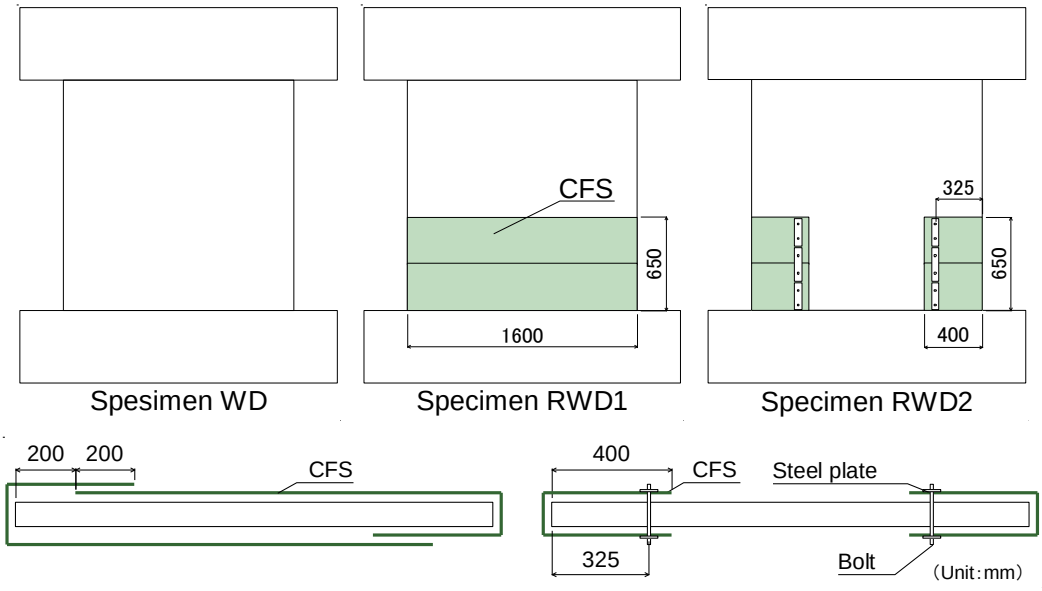

Figure 4-14 Test specimens

To attach the CFS, the corners of the walls were chamfered to a diameter of 13mm, epoxy resin was first applied to the wall surface, the CFS was then attached while maintaining tension manually and with a roller, and then epoxy resin was further applied on top with a roller to impregnate the CFS. Moreover, the top and bottom sheets were overlapped by 10 mm each. For specimen RWD2, the CFS was fixed by steel plates (PL-4.5) and threaded bolts (M10) as shown in Figure 4-14. The threaded bolts were installed into drilled hole after concrete casting and threaded bolts were tightened without management of tightening torque of bolts.

4.2.2 Outline of loading test

A description of the loading device is presented in Figure 4-3. A horizontal lateral force applied in cycles over the positive and negative directions was used for the loading. Also, a constant axial load of 273kN (Equation (4-1)) was applied at the top of the specimen using a couple of vertical hydraulic jacks. Where, used F_c of compressive strength of concrete was 26.7 N/mm^2 in this calculation.

$$N = 0.08 l_w t_w F_c \tag{4-3}$$

Additional moment was applied at the top of the specimen by controlling these vertical jacks to correspond to the acting shear force, such that the shear span ratio was 1.5, using Equation (4-2).

$$N_E = \frac{N}{2} \pm \frac{Q}{l}(h_s - a)$$
$$N_W = \frac{N}{2} \mp \frac{Q}{l}(h_s - a) \tag{4-4}$$

In the experiment, the horizontal displacement δ measured at the top stub, divided by the height of the measurement point h (1985 mm), was controlled through the drift angle of the member $R = \delta / h$. The loading cycle started with one cycle of R = 1/800 rad, and then two cycles each of R = 1/400, 1/200, 1/133, 1/100, 1/67, 1/50 and 1/33 rad, as is shown in Table 4-5.

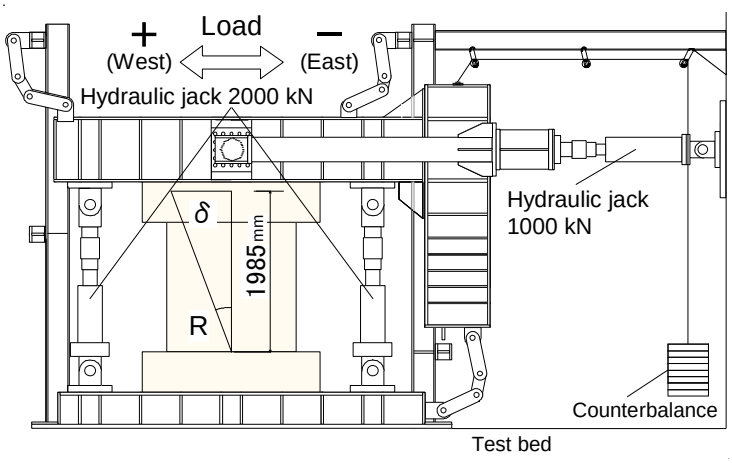

Figure 4-15 Loading apparatus

Table 4-10 Loading pattern

R	R (%)	δ (mm)	Number of cycles
1/800	0.125	2.48	1
1/400	0.25	4.96	2
1/200	0.5	9.93	2
1/133	0.75	14.93	2
1/100	1.0	19.85	2
1/67	1.5	29.63	2
1/50	2.0	39.70	2
1/33	3.0	60.15	2

4.2.3 Measuring method

In the tests, the horizontal displacement was measured at the top of the wall and along with the boundary ends of wall. The vertical deformation was measured along the boundary ends of the wall and over the wall base. The diagonal deformation was measured from the top corner to the opposite bottom corner of the wall. Horizontal, vertical and diagonal deformation was measured using displacement transducers as is shown in Figure 4-16. Figure 4-17 shows the strain gauges distribution of the longitudinal and horizontal reinforcing steel bars of the wall. Besides, CFS was measured using strain gauges, the strain gauges setup on the CFS is shown in Figure 4-18. Additionally, the widths of cracks were measured using a crack scale at each loading cycle.

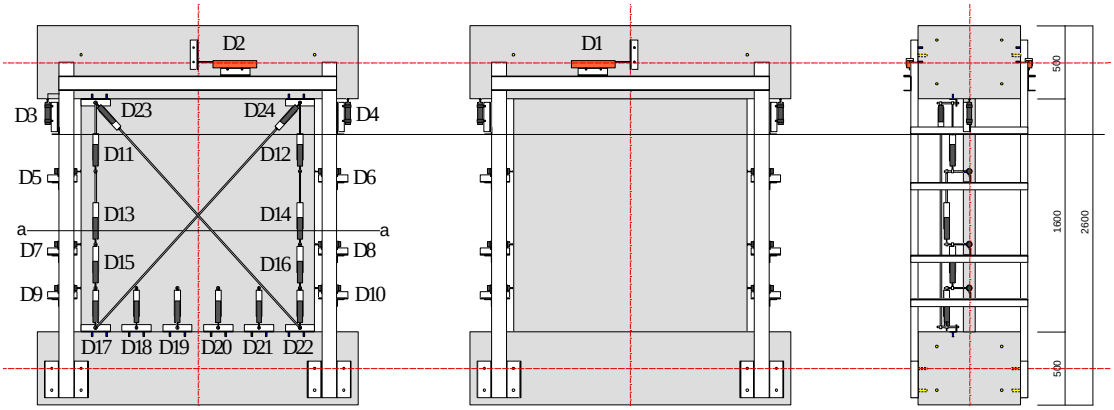

Figure 4-16 Horizontal, vertical and diagonal displacement transducers setup

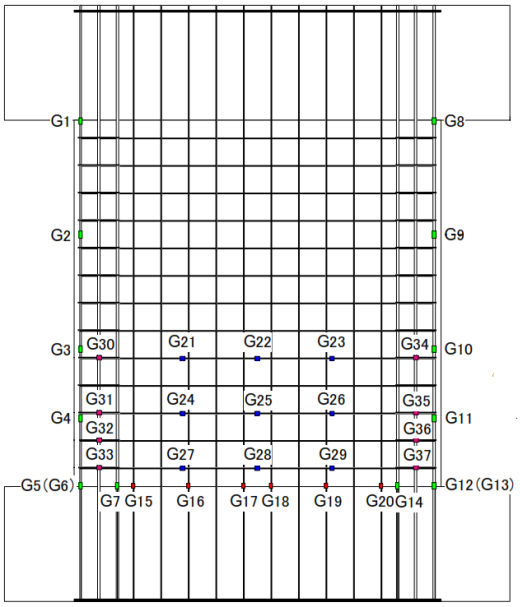

Figure 4-17 Strain gauges setup – Reinforcing steel bars

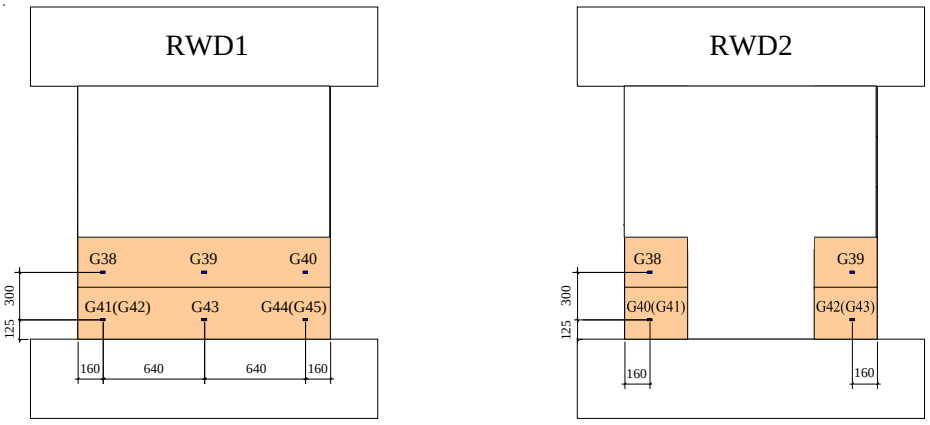

Figure 4-18 Strain gauges setup – CFS

4.2.4 Test result

The relationship between lateral load and drift angle for each specimen is shown in Figure 4-19.

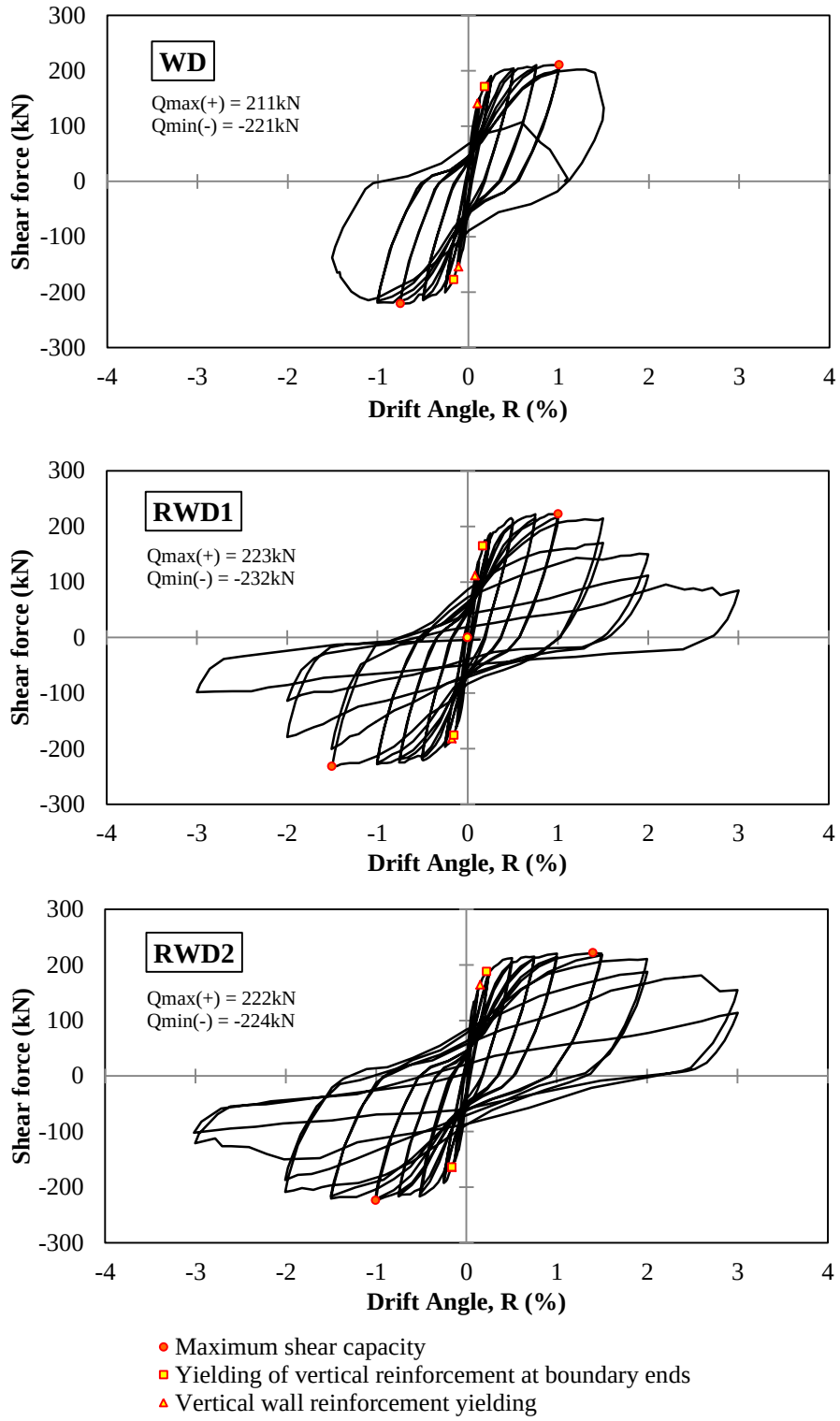

Figure 4-19 Lateral load and drift angle relationship

From experimental hysteretic curves of the three LDRC walls (WF, RWF1, and RWF2); the envelope curve (skeleton curve) for each specimen was found as is shown in Figure 4-20. Moreover, Figure 4-21 shows the comparison between the envelope curves of the tested walls.

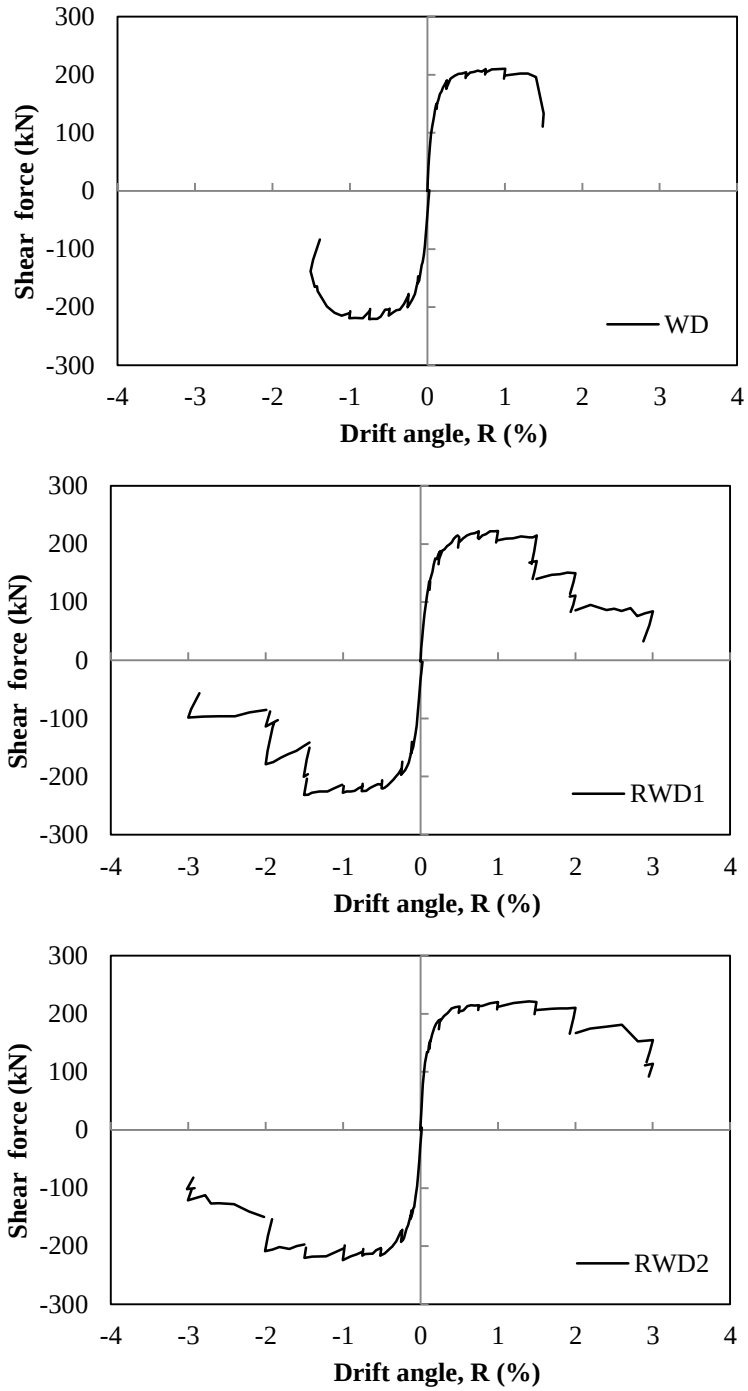

Figure 4-20 Experimental envelope curves

By comparing the envelope curves of the tested walls, it can be observed that the maximum strength remains about the same level, but most importantly, deformation capacity got improved, in both retrofitted walls, RWD1 and RWD2, in comparison with the non-retrofitted wall WD. Also it can be appreciated that wall RWD2 got larger deformation capacity than the wall RWD1, this could be explained due to the different retrofitted method, were RWD2, was retrofitted at the ends of the wall while RWD1 was retrofitted by wrapping the CFS over the entire span; both with partial height of the wall retrofitted.

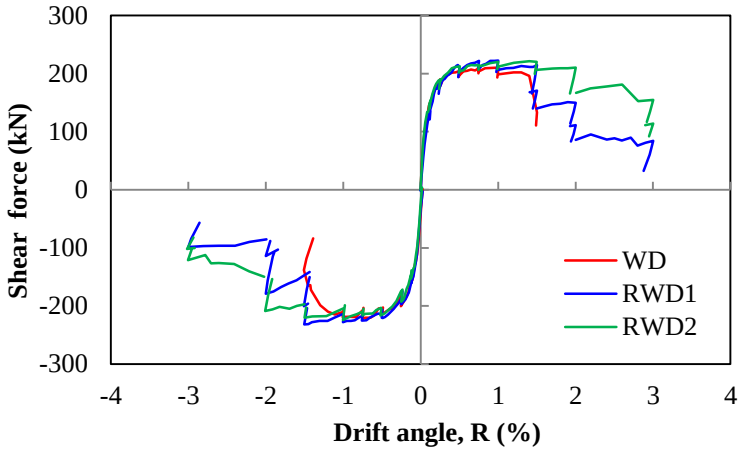

Figure 4-21 Comparison of experimental envelope curves

For specimen WD, flexural crack and flexural shear cracks appeared at the same cycle that the vertical wall reinforcement yielded under the R = 1/800 rad cycle, while the vertical reinforcement at boundary ends yielded under the R = 1/400 rad cycle. Afterwards, maximum capacity was reached at the R = 1/133 rad cycle. Concrete spalling at the lower part of the wall occurred under the second R = 1/100 rad cycle. Compression failure of concrete at the lower part of the wall occurred together with steep capacity deterioration under the R = 1/67 rad cycle, and buckling of vertical reinforcement at the boundary end was observed. (See Figure 4-22)

Figure 4-22 Failure of specimen WD

For specimen RWD1, flexural crack and flexural shear cracks appeared at the same cycle that the vertical wall reinforcement yielded under the R = 1/800 rad cycle, while the vertical reinforcement at boundary ends yielded under the R = 1/400 rad cycle, similar to specimen WD. Maximum capacity was reached at the *R* = 1/67 rad cycle, the boundary end wrapped CFS began to swell. In subsequent loading cycles, concrete swelling at the wall base grew until swelling occurred at the center of the lower part of the wall as well with capacity deterioration. Fracture of CFS occurred under the *R* =1/33 rad cycle. (See Figure 4-23)

Figure 4-23 Failure of specimen RWD1

For specimen RWD2, flexural crack and flexural shear cracks appeared under the *R* = 1/800 rad cycle, and the vertical wall reinforcement and the vertical reinforcement at boundary ends yielded under the *R* = 1/400 rad cycle. Maximum capacity was reached at the *R* = 1/100 rad cycle. The boundary end wrapped CFS began to swell at the same cycle, afterwards, concrete swelling at the wall base grew and capacity decreased with progress of loading cycle. Fracture of CFS occurred under the *R* =1/33 rad cycle. (See Figure 4-24)

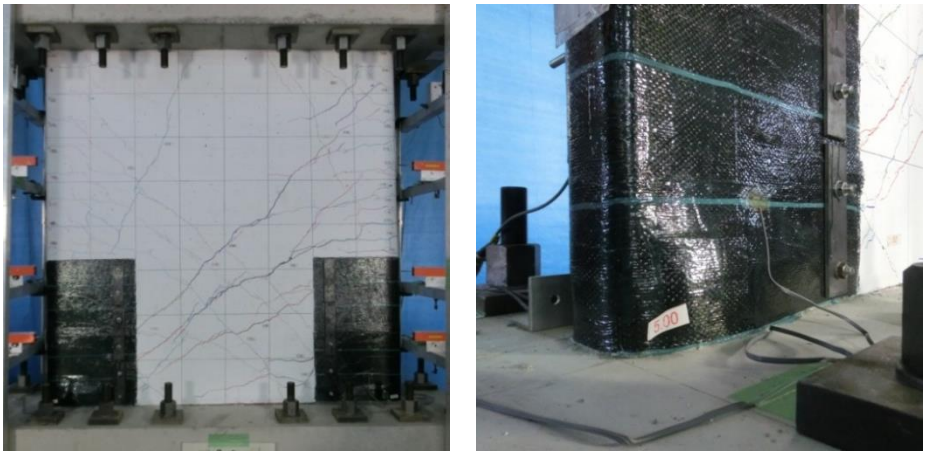

Figure 4-24 Failure of specimen RWD2

4.3 Confinement effect of concrete with carbon fiber sheet reinforcement

From the previous tests it was verified that the carbon fiber sheets delay the concrete crushing of the wall base that occurs during the flexural failure and that deformation capacity was improved. Moreover, during the test with the retrofitted walls (with full height and partial height retrofitting) it was observed that the crushing of the concrete produces bulges at the base corners of the wall. Additionally, when the maximum strain on the CFS is reached, the carbon fiber sheet over the crushed concrete area fails suddenly.

In order to verify the confinement effect of the carbon fiber sheet that covers the concrete, a third experiment was conducted in 2015 at TUT using concrete samples with or without CFS subjected under compressive loading (monotonic and cyclic), by changing the size, shape and amount of CFS layers. Characteristics of the specimens were decided following Lam and Teng's research [16][17] and Nakatsuka's research. [23]

4.3.1 Design of specimen

In total, 39 concrete samples were tested under compressive loading (monotonic and cyclic). The specimens have three kinds of cross section shapes: circular (C), square (S) and rectangular (R); the ratio of each specimen corresponds to the ratio of $\overline{(w/b)(h/b)}$, where b, w and h are the thickness, width and height of the specimen respectively. Table 4-11 shows the dimensions and quantities of each specimen.

Table 4-11 Dimension of the specimens

Shape	Ratio	b (mm)	w (mm)	h (mm)	Quantity
C	2	ϕ 150		300	8
S	12	150	150	300	9
S	13			450	2
R	22	150	300	300	4
R	23			450	2
R	32	100	300	200	5
R	33			300	2
R	42	100	400	200	5
R	43			300	2

29 specimens were retrofitted using carbon fiber sheet wrapped over the lateral surface of the specimen by using chemical epoxy. Table 4-12 shows the materials properties of the different carbon fiber sheet used to retrofit the concrete samples. Where ρ_f is the density per unit of area of CFS, t is the thickness of CFS, E_f is the young modulus of CFS, σ_{fu} is the ultimate tensile strength of CFS and ε_{fu}, is the ultimate tensile strain of CFS.

Table 4-12 Material properties of CFS with glue

CFS	ρ_f (g/m^2)	t (mm)	E_f (MPa)	σ_{fu} (MPa)	ε_{fu} (%)
1	200	0.111	249000	4283	1.72
2	300	0.167	249000	4681	1.88
3	300	0.163	444000	3241	0.73

All square and rectangular specimens has a chamfer radius, which is the radius at rounded corners, $R = 15mm$, except for 4 specimens with $R = 30mm$. Besides, one circular and one square shaped specimen where retrofitted using a CFS with higher young modulus (CFS-3). Finally, 2 specimens where retrofitted by fixing the CFS with steel plates and bolts.

Each specimen was allocated a code which represents the geometry of the specimen, type of CFS and special conditions. (See Figure 4-25)

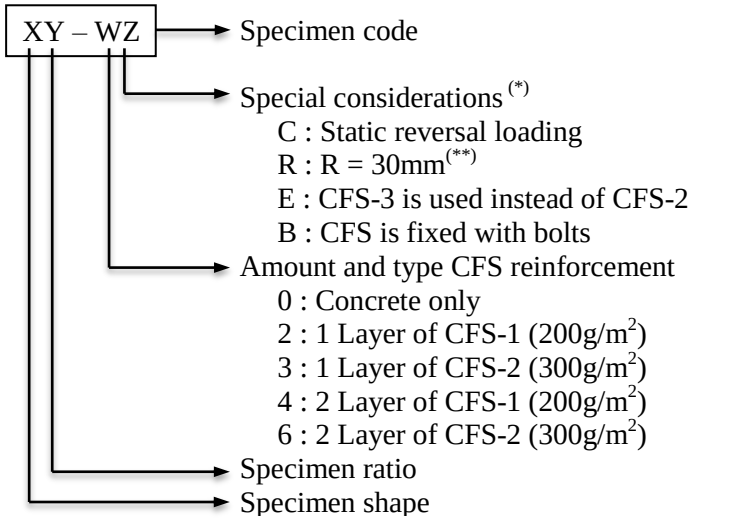

(*) No character means monotonic test
(**) R is the chamfer radius of the specimen for other cases R = 15mm

Figure 4-25 Specimen code

4.3.2 Outline of loading test

Two types of test where conducted:

- Monotonic test, where the specimen is under compressive loading until failure.
- Static reversal loading (Cyclic Test), where the specimen is under cyclic loading until failure. Once the target strain is reached, the unloading stage starts until zero stress, and then the reloading continues to the next target strain. (See Figure 4-26)

Figure 4-27 shows the compression loading machine used for the experiment with a maximum compression loading of 2000kN. Table 4-13 shows the type of loading for each specimen and condition.

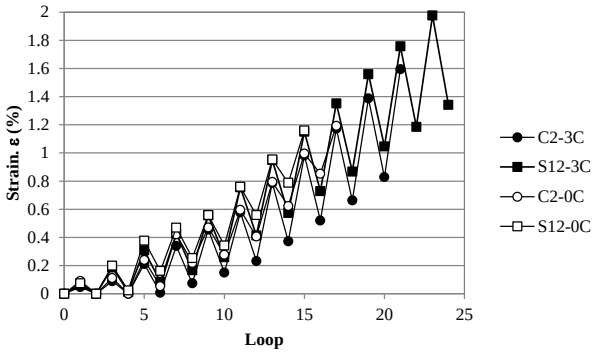

Figure 4-26 Loading pattern for cyclic test

Figure 4-27 Compression loading machine

Table 4-13 Loading tests

XY	WZ									
	0	0C	2	3	3C	3R	3E	3B	4	6
C2	○	○	○	○	○		○		○	○
S12	○	○	○	○	○	○	○		○	○
S13	○			○						
R22	○		○	○		○				
R23	○			○						
R32	○		○	○		○		○		
R33	○			○						
R42	○		○	○		○		○		
R43	○			○						

4.3.3 Measuring method

The vertical displacement of the concrete along the compressive direction was measured using displacement transducers for all the specimens, as is shown in Figure 4-28. In the case of the retrofitted specimens with CFS, the horizontal strain of the CFS was measured using strain gauges. Specimens with CFS and strain gauges are shown in Figure 4-29.

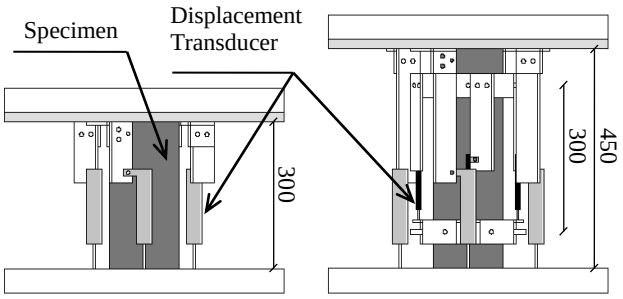

Figure 4-28 Arrangement of measuring devices (unit: mm)

Figure 4-29 Specimens with and without strange gauges

4.3.4 Test results

4.3.4.1 Circular shaped

The circular shaped specimen C2 is 150mm in diameter and 300mm in height. Figure 4-30 shows the experimental curves for specimens C2 under monotonic loading. The maximum strength of the concrete, f_c', without CFS (C2-0) is 36.03MPa, the strain corresponding to the maximum strength, ε_{cu}, is 0.0024. Table 4-14 shows the maximum strength and maximum strain for each specimen C2 under monotonic and cyclic loading.

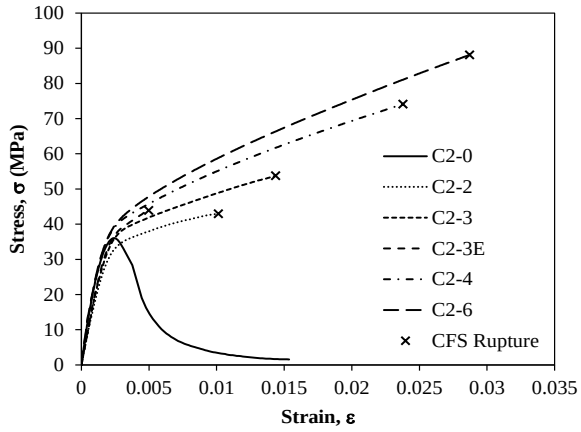

Figure 4-30 Stress-strain relationship of concrete – C2 under monotonic loading

Figure 4-31 corresponds to the specimens C2 under cyclic loading, specimen C2-0C (concrete only) and specimen C2-3C (concrete with CFS confinement). Both, Figure 4-30 and Figure 4-31 shows the increment in strength and the increment of deformation capacity due to CFS confinement on the concrete samples.

Table 4-14 Maximum strength and strain for circular shaped specimens

Specimen	Maximum Strength (MPa)	Strain at Maximum Strength (%)	Maximum Strain (%)
C2-0	36.03	0.24	1.54
C2-0C	35.56	0.23	1.19
C2-2	42.96	1.01	1.01
C2-3	53.73	1.44	1.44
C2-3C	55.70	1.94	1.94
C2-3E	43.87	0.50	0.50
C2-4	74.11	2.38	2.38
C2-6	88.12	2.87	2.87

Figure 4-32 shows specimens C2-0 and C2-0C (concrete only) corresponding to the monotonic curve and cyclic curve respectively; the monotonic curve follows the shape of the envelope of the cyclic curve. In the same way, Figure 4-33 shows the good match between specimens C2-3 and C2-3C corresponding to the monotonic curve and cyclic curve respectively for specimens retrofitted with CFS.

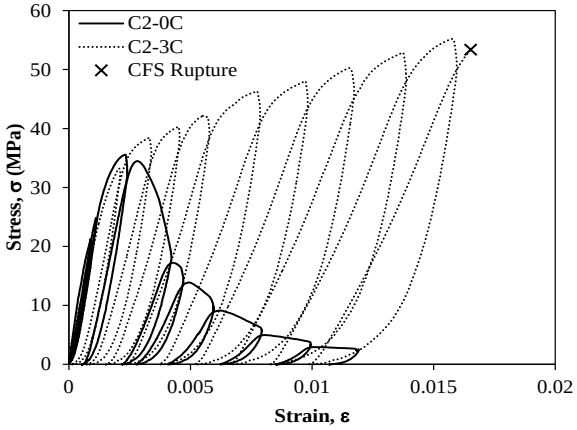

Figure 4-31 Stress-strain relationship of concrete – C2 under cyclic loading

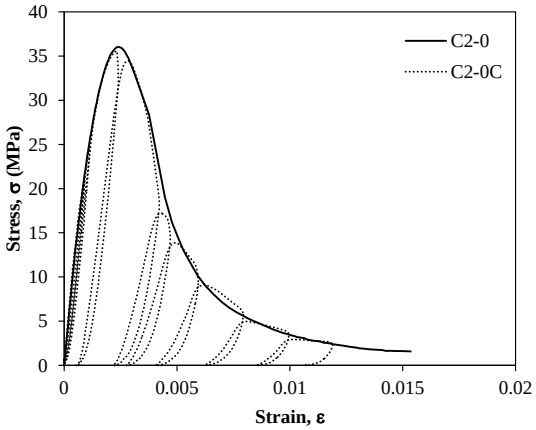

Figure 4-32 Comparison between monotonic and cyclic curve – C2 without CFS

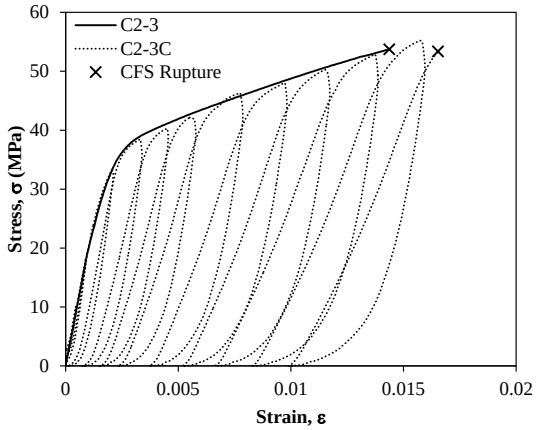

Figure 4-33 Comparison between monotonic and cyclic curve – C2 with CFS

During the failure mode with the circular shaped specimens (C2) retrofitted with CFS a sudden failure occurs when maximum strength is reached. This can be explained as the deformation of the concrete applies about the same level of stress on the CFS. Figure 4-34

shows the failure sequence: (a) shows the state of the specimen before reaching the maximum strength, (b) shows the state of the specimen when the maximum strength is reached; after this, the strength drops suddenly (c) shows the remaining core of concrete and (d) shows the state of the specimen after the crushing of concrete.

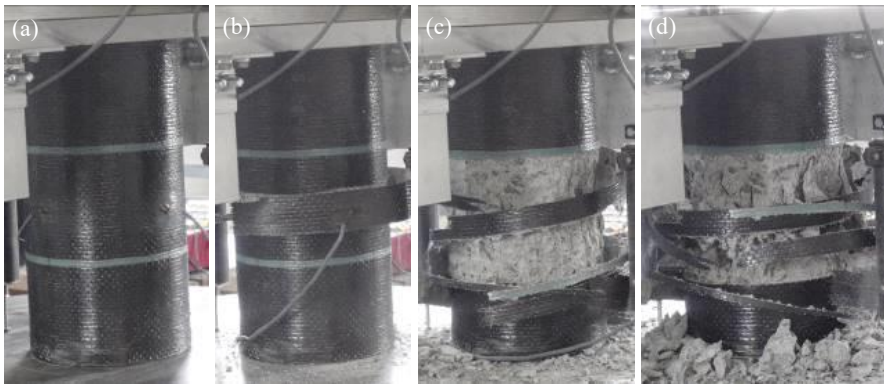

Figure 4-34 Failure mode of circular shaped specimens

4.3.4.2 Square shaped

The square shaped specimen has a cross section of 150mm x 150mm and heights of 300mm and 450mm for S12 and S13 respectively. Figure 4-35 shows the experimental curves for specimens S12 and S13 under monotonic loading. Both, specimens S12 and S13 show a discrepancy in terms of the maximum strength of the concrete between the non-retrofitted sample and the sample retrofitted with CFS; where specimens with CFS have a higher maximum strength than the non-retrofitted specimen. Besides, specimens retrofitted with CFS shows an increment of the deformation capacity due to the CFS confinement. Table 4-15 shows the maximum strength and maximum strain for each specimen, S12 and S13, under monotonic and cyclic loading.

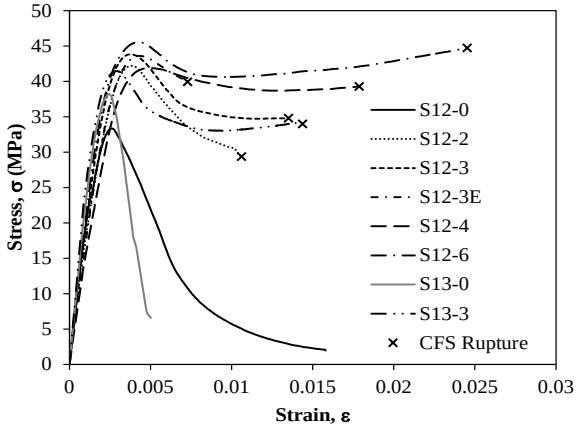

Figure 4-35 Stress-strain relationship of concrete – S12 and S13 under monotonic loading

Table 4-15 Maximum strength and strain for square shaped specimens

Specimen	Maximum Strength (MPa)	Strain at Maximum Strength (%)	Maximum Strain (%)
S12-0	33.34	0.26	1.58
S12-0C	38.46	0.27	1.16
S12-2	42.21	0.38	1.06
S12-3	43.83	0.38	1.35
S12-3C	39.55	0.42	2.55
S12-3R	43.93	0.50	1.44
S12-3E	43.62	0.43	0.73
S12-4	41.89	0.50	1.79
S12-6	45.55	0.42	2.45
S13-0	38.20	0.24	0.50
S13-3	41.46	0.30	1.44

Figure 4-36 corresponds to the specimens S12 under cyclic loading, specimen S12-0C (concrete only) and specimen S12-3C retrofitted with CFS. The contribution of the CFS confinement can be observed by increasing the maximum strain, but not the maximum strength, which remains about the same.

Figure 4-37 shows a slight discrepancy in terms of the maximum strength between the monotonic curve (S12-0) and the cyclic curve (S12-0C), where specimen S12-0 has a lower strength than specimen S12-0C. This occurs because of the relocation of the head of the compression machine over the top of the specimen during the monotonic compression test. On the other hand, Figure 4-38 shows the comparison between the monotonic curve (Specimen S12-3) and the cyclic curve (Specimen S12-3C), where specimen S12-3 has a greater strength than specimen S12-3C.

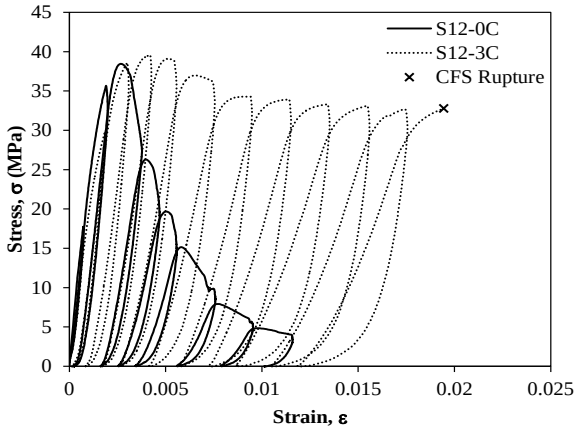

Figure 4-36 Stress-strain relationship of concrete – S12 under cyclic loading

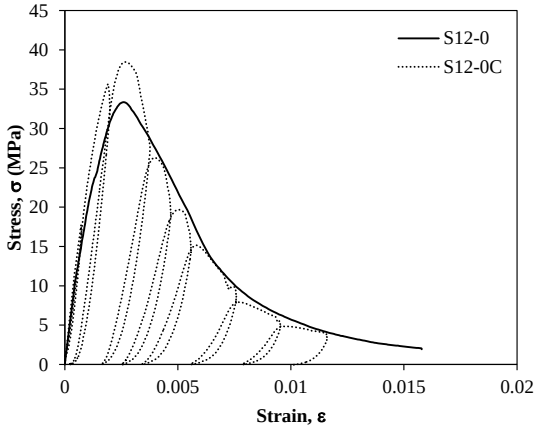

Figure 4-37 Comparison between monotonic and cyclic curve – S12 without CFS

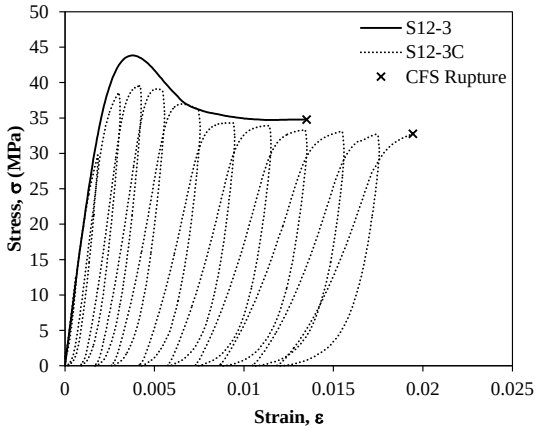

Figure 4-38 Comparison between monotonic and cyclic curve – S12 with CFS

In the failure mode with the square shaped specimens (S12 and S13) retrofitted with CFS, a two-step failure occurs; due to the stress on the CFS concentrated at the rounded corners of the specimen. Figure 4-39 shows the failure sequence: (a) shows the state of the specimen before reaching the maximum strength, (b) shows the state of the specimen after the maximum strength is reached, the strength decreases and the strain deformation capacity is improved, (c) shows the state of the specimen when CFS fails first at one corner releasing partially the confinement provided by CFS and (d) shows the state of the specimen when the CFS fails at the opposite corner. This study will consider the stress-strain relationship until the first CFS failure.

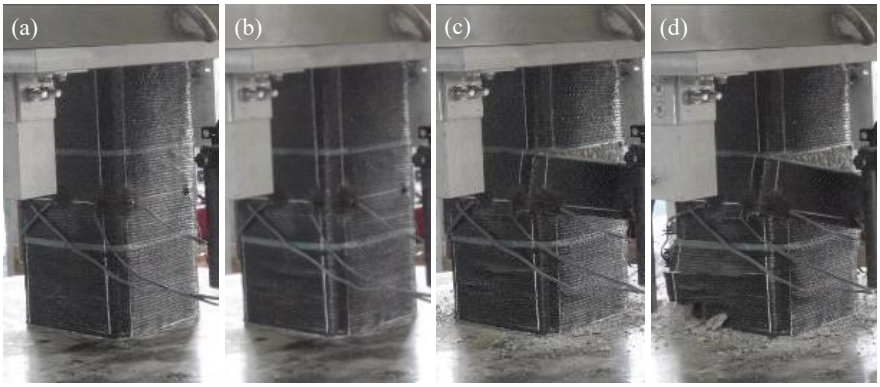

Figure 4-39 Failure mode of square shaped specimens

4.3.4.3 Rectangular shaped

Figure 4-40, Figure 4-41 and Figure 4-42 corresponds to the experimental curve for specimens R22 & R23, R32 & R33 and R42 & R43 under monotonic loading. Table 4-16 shows the maximum strength and maximum strain for each rectangular specimen under monotonic loading.

Table 4-16 Maximum strength and strain for rectangular shaped specimens

Specimen	Maximum Strength (MPa)	Strain at Maximum Strength (%)	Maximum Strain (%)
R22-0	37.74	0.33	0.45
R22-2	36.61	0.38	0.72
R22.3	36.85	0.42	0.63
R22-3R	37.87	0.42	1.68
R23-0	30.02	0.23	0.33
R23-3	36.71	0.40	1.09
R32-0	42.34	0.32	0.41
R32-2	39.80	0.34	4.83
R32-3	39.01	0.54	2.34
R32-3R	49.93	0.68	3.22
R32-B	40.90	0.38	2.32
R33-0	39.10	0.27	0.34
R33-3	39.87	0.32	0.32
R42-0	43.47	0.33	0.39
R42-2	40.05	0.38	1.94
R42-3	38.59	0.51	0.58
R42-3R	46.01	0.58	2.55
R42-3B	40.68	0.37	2.64
R43-0	35.89	0.27	0.34
R43-3	32.60	0.39	1.87

The failure mode of rectangular shaped specimens (R22, R23, R32, R33, R42 and R43) retrofitted with CFS occurs in a similar way to the square shaped specimens.

Figure 4-40 show a discrepancy in terms of the maximum strength of the concrete between the non-retrofitted sample and the sample retrofitted with CFS; where specimens with CFS have a higher maximum strength than the non-retrofitted specimen. Besides, retrofitted specimens with CFS show an increment of the deformation capacity.

Specimens R22 and R33, in Figure 4-40 and Figure 4-41 respectively, shows a relatively close maximum strength in all of the specimens. However, specimens R23, R32, R42 and R43 in Figure 4-40, Figure 4-41 and Figure 4-42, show a discrepancy in terms of the maximum strength.

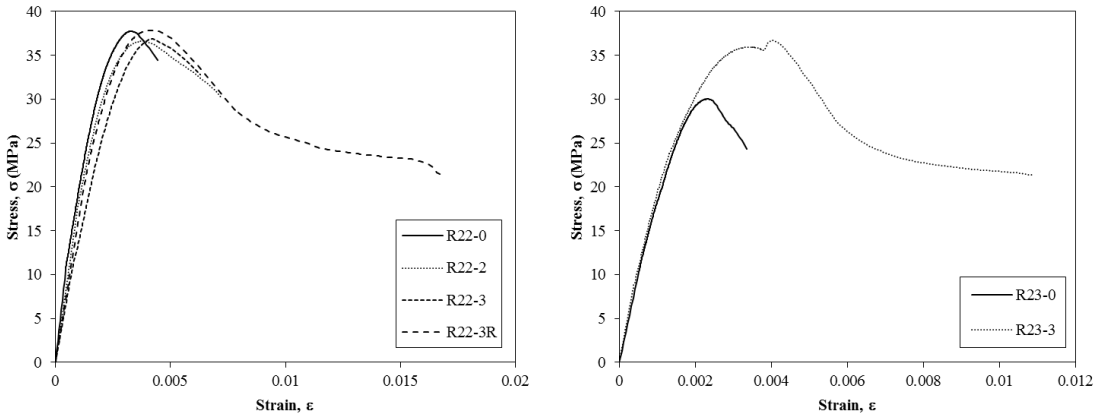

Figure 4-40 Stress-strain relationship of concrete – R22 and R23 under monotonic loading

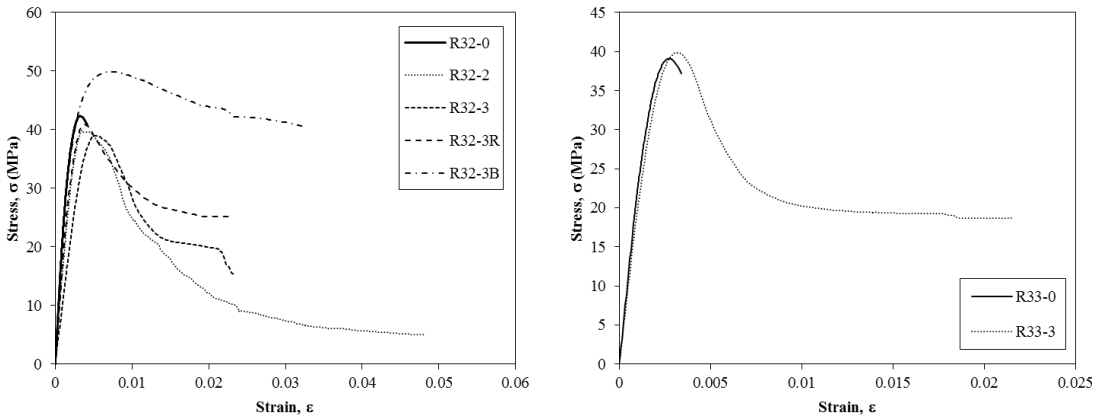

Figure 4-41 Stress-strain relationship of concrete – R32 and R33 under monotonic loading

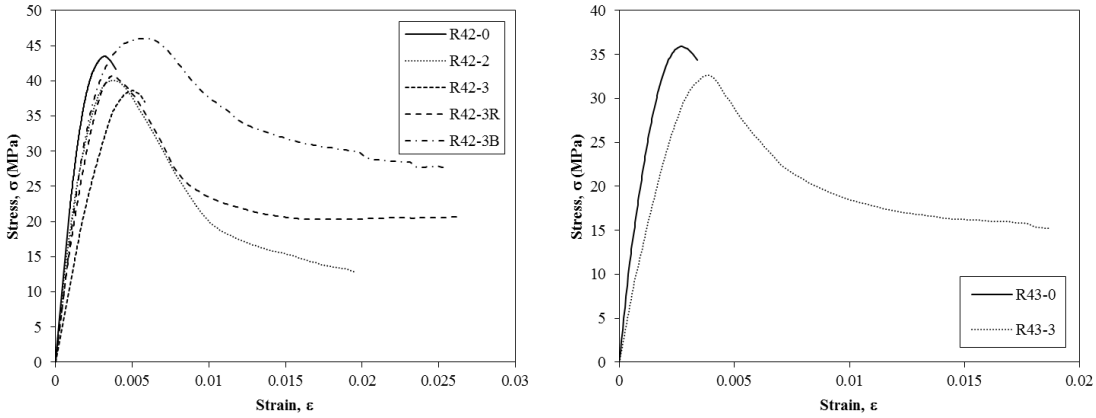

Figure 4-42 Stress-strain relationship of concrete – R42 and R43 under monotonic loading

4.3.5 Analysis of the test results

From the test result, the effect of the parameters such as the shape effect, the amount of CFS, the chamfer radius, the Young Modulus of the CFS and the usage of bolts for fixing the CFS is studied in this research.

Figure 4-43 shows the effect of the amount of CFS used to confine the concrete samples, specimens C2 has an important contribution in terms of maximum stress, strain at maximum stress and maximum strain, while for square and rectangular shaped specimens, the maximum stress and strain at maximum stress remains at about the same values with a slight discrepancy. Specimens C2, S12, S13, R23, R32, R42 and R43 show an increment of the maximum strain according to the amount of CFS. The clear contribution of CFS on circular shaped specimens in terms of maximum stress, strain at maximum stress and maximum strain, occurs because the stress over the CFS tend to be uniform in case of circular shaped specimens unlike square and rectangular shaped specimens where the stress over the CFS is concentrated at the rounded corners.

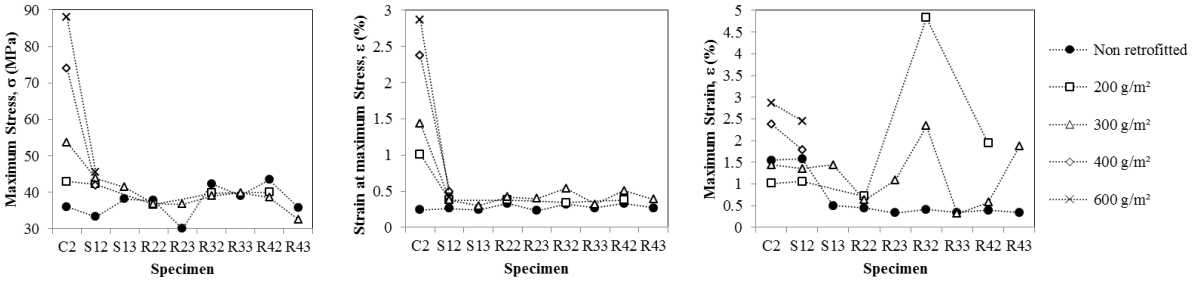

Figure 4-43 Effect of the amount of CFS

Figure 4-44 shows the effect of the radius R at the rounded corners of the square and rectangular shaped specimens tested, by comparing specimens with R=30mm and R=15mm, it can be observed that a larger radius helps to increase the maximum stress, the strain at maximum strain and the maximum strain. This occurs because the stress of CFS at the rounded corners of specimens of R=30mm has improved stress distribution in comparison with specimens of R=15mm.

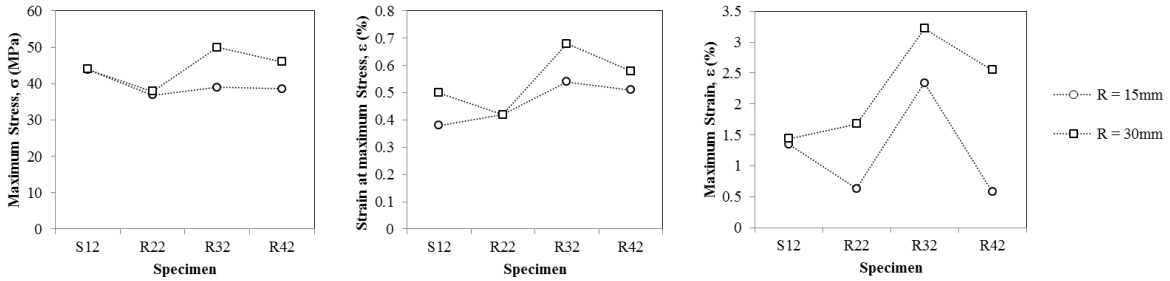

Figure 4-44 Effect of the chamfer radius

Figure 4-45 shows the effect of the Young Modulus of CFS-2 (249000MPa) and CFS-3 (444000MPa) and its corresponding ultimate strain 1.88% and 0.73% respectively, where it displays an important contribution in terms of the maximum strain. This can be explained because CFS-2 has a larger ultimate strain than CFS-3. Therefore, CFS-3 has a brittle behaviour in comparison with CFS-2. For circular shaped specimen, the Young Modulus of CFS-2 shows an improved maximum strength and an improved strain at maximum stress, while for square shaped specimen remains about the same values.

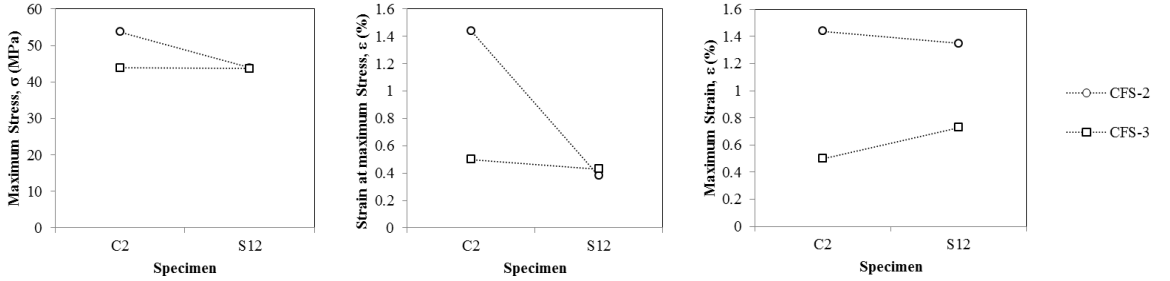

Figure 4-45 Effect of the Young Modulus of CFS

Figure 4-46 shows the effect of using bolts to fix the CFS to the rectangular specimens. It can be seen that the maximum stress remains about the same in both cases; the strain at maximum stress is improved without bolts, however the maximum strain is improved when bolts are used in specimen R42, this may happen because of the axial contribution of the steel plates attached to the specimens for fixing the bolts during the last stage of the test.

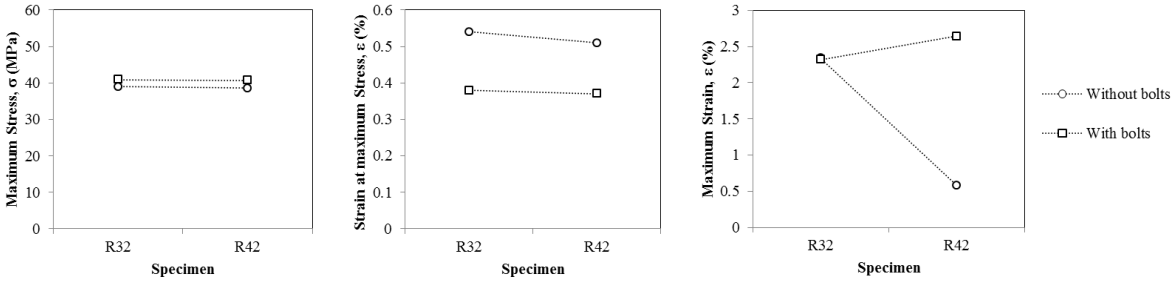

Figure 4-46 Effect of the CFS fixed with bolts

CHAPTER 5

MONOTONIC STRESS-STRAIN RELATIONSHIP OF CONCRETE WITH CFS CONFINEMENT

CHAPTER 5 : MONOTONIC STRESS-STRAIN RELATIONSHIP OF CONCRETE WITH CFS CONFINEMENT

To study the stress-strain relationship of the concrete retrofitted with CFS under monotonic loading, two stress-strain models were reviewed:

Lam and Teng [16][17] proposed a stress-strain relationship to model CFS confined concrete for circular and rectangular shaped specimens. This model consider an envelope curve with two parts, first part correspond to a parabolic function until a transition point from which the second part starts following a linear function until the rupture point.

Nakatsuka [23] proposed a stress-strain relationship to model CFS confined concrete for circular and square shapes. This model considers an envelope with three parts, first part corresponds to n-grade function, second and third parts follow a linear function.

From the third experiment shown in Section 3.3.4, circular and square shaped specimens subjected under monotonic loading (6 circular shaped specimens and 9 square shaped specimens) are chosen to conduct the comparison between both, Lam and Teng's model and Nakatsuka's model [28]. Table 5-1 shows the dimension of the circular and square shaped specimens and the amount of CFS used.

Table 5-1 Dimension and amount of CFS

Specimen	*b* (mm)	*d* (mm)	*h* (mm)	p_f (%)
C2-0	ϕ150		300	-
C2-2				0.148
C2-3				0.223
C2-3E				0.217
C2-4				0.296
C2-6				0.445
S12-0	150	150	300	-
S12-2				0.148
S12-3				0.223
S12-3E				0.217
S12-4				0.296
S12-6				0.445
S13-0	150	150	450	-
S13-3				0.223

5.1 Lam and Teng's model

Figure 5-1 shows the monotonic stress-strain relationship for concrete with CFS confinement proposed by Lam & Teng [16][17] and reviewed by Benzaid et al. [5], which consists of a parabolic portion following Equation (5-1) and a linear portion following Equation (5-2).

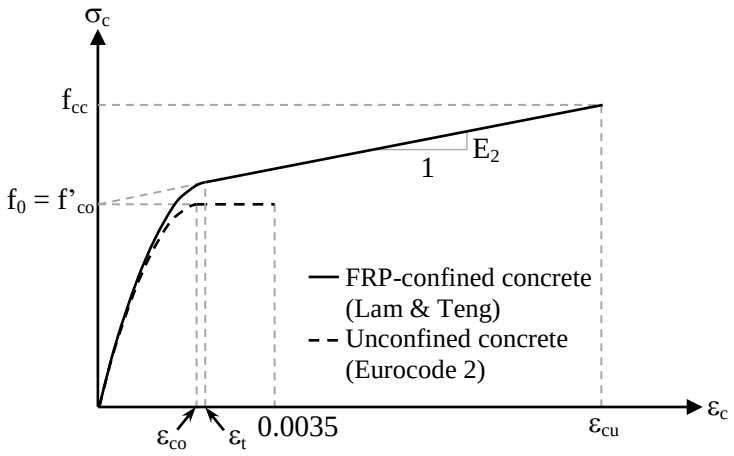

Figure 5-1 Lam and Teng's stress-strain model

$$\sigma_c = E_c\varepsilon_c - \frac{(E_c - E_2)^2}{4f'_{co}}\varepsilon_c^2 \quad for \quad 0 \le \varepsilon_c \le \varepsilon_t \tag{5-1}$$

$$\sigma_c = f'_{co} + E_2\varepsilon_c \quad for \quad \varepsilon_t < \varepsilon_c \le \varepsilon_{cu} \tag{5-2}$$

From the above equations, E_2 and ε_t are defined by Equations (5-3) and (5-4) respectively.

$$E_2 = \frac{f'_{cc} - f'_{co}}{\varepsilon_{cu}} \tag{5-3}$$

$$\varepsilon_t = \frac{2f'_{co}}{(E_c - E_2)} \tag{5-4}$$

Where:

f'_{co}: Compressive strength of unconfined concrete.
E_c: Elastic modulus of unconfined concrete.
E_2: Slope of linear portion of the envelope.
f'_{cc}: Compressive strength of CFS confined concrete.
ε_{cu}: Ultimate strain of CFS confined concrete.
ε_t: The strain at the transition point.

The compressive strength and ultimate axial strain of concrete confined by CFS are defined by Equation (5-5) and (5-6) respectively.

$$\frac{f'_{cc}}{f'_{co}} = 1 + 3.3\frac{f_l}{f'_{co}} \tag{5-5}$$

$$\frac{\varepsilon_{cu}}{\varepsilon_{co}} = 1.75 + 12\frac{f_l}{f'_{co}}\left(\frac{\varepsilon_{h,rup}}{\varepsilon_{co}}\right) \tag{5-6}$$

$$f_l = \frac{E_{frp}t\varepsilon_{h,rup}}{R} \tag{5-7}$$

Where:

ε_{co}: Axial strain at the compressive strength of unconfined concrete and is assumed a constant value of 0.002.

$\varepsilon_{h,rup}$: CFS hoop rupture strain.

f_l: Lateral confining pressure provided by CFS jacket at hoop rupture failure. Equation (5-7)

E_{frp}: Elastic modulus of CFS.

t: Thickness of CFS jacket.

R: Radius of the confined concrete core.

5.2 Nakatsuka's model

Figure 5-2 shows the monotonic stress-strain relationship for concrete with CFS confinement proposed by Nakatsuka [23], which consists of an n-degree function, linear function with slope E_{BT} and a linear function with slope E_{TR} following Equations (5-8), (5-9) and (5-10) respectively.

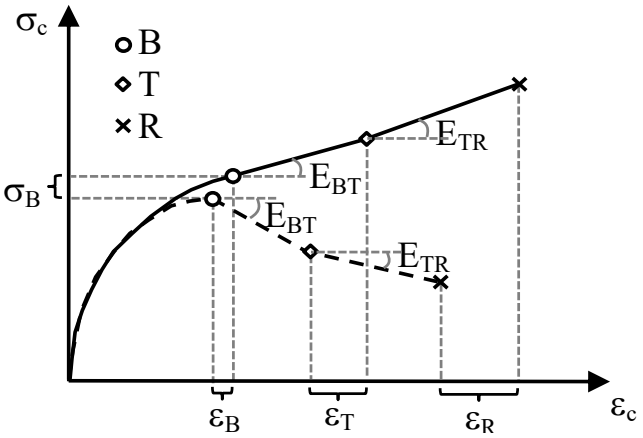

Figure 5-2 Nakatsuka's stress-strain model

$$\sigma_c = E_c\varepsilon_B\left(\frac{\varepsilon_c}{\varepsilon_B} - \frac{a}{n}\left(\frac{\varepsilon_c}{\varepsilon_B}\right)^n\right) \quad for \quad 0 \le \varepsilon_c \le \varepsilon_B \tag{5-8}$$

$$\sigma_c = \sigma_B + E_{BT}\varepsilon_B\left(\frac{\varepsilon_c}{\varepsilon_B} - 1\right) \quad for \quad \varepsilon_B \le \varepsilon_c \le \varepsilon_T \tag{5-9}$$

$$\sigma_c = \sigma_B + E_{BT}\varepsilon_B\left(\frac{\varepsilon_T}{\varepsilon_B} - 1\right) + E_{TR}\varepsilon_T\left(\frac{\varepsilon_c}{\varepsilon_T} - 1\right) \quad for \quad \varepsilon_T \le \varepsilon_c \le \varepsilon_R \tag{5-10}$$

Where:

$$a = \begin{cases} 1 & (E_{BT} \le 0) \\ 1 - \dfrac{E_{BT}}{E_c} & (E_{BT} > 0) \end{cases} \qquad and \qquad n = \frac{E_c\varepsilon_B}{E_c\varepsilon_B - \sigma_B}a$$

And B, T, R points and the two slopes are defined as follows:

Stress at B :
$$\frac{\sigma_B}{F_0} = 1 + 4C_{\sigma_B}\frac{p_f E_f \varepsilon_{fB}}{F_0} \tag{5-11}$$

Strain at B :
$$\frac{\varepsilon_B}{\varepsilon_0} = 1 + 10C_{\varepsilon_B}\frac{p_f E_f \varepsilon_{fB}}{F_0} \tag{5-12}$$

$$\varepsilon_{fB} = \begin{cases} 0.01\left(1 - \dfrac{1}{\dfrac{F_0}{140} + 1}\right) & (F_0 \le 60) \\ 0.003 & (60 < F_0 \le 80) \end{cases} \tag{5-13}$$

Strain at T :
$$\frac{\varepsilon_T}{\varepsilon_0} = (-0.016F_0 + 2.7) + (-10^{-5}F_0 + 0.0016)C_{\varepsilon_T}p_f E_f \tag{5-14}$$

Strain at R :
$$\frac{\varepsilon_R}{\varepsilon_0} = \left(20\varepsilon_{fr} + 1.2\right) + \left(1000\varepsilon_{fr} - 3\right)C_{\varepsilon_R}\frac{p_f E_f}{{F_0}^2} \tag{5-15}$$

First Slope :
$$\frac{E_{BT}}{E_{0BT}} = -0.4 + \frac{1.4}{C_{\varepsilon_{BT}}\dfrac{p_f E_f}{0.06{F_0}^2} + 1} \tag{5-16}$$

Second Slope :
$$\frac{E_{TR}}{E_{0BT}} = -0.25 + \frac{0.55}{C_{\varepsilon_{TR}}\dfrac{p_f E_f}{0.06{F_0}^2} + 1} \tag{5-17}$$

$$E_{0BT} = 1000(6 - 0.43F_0) \quad [MPa]$$

Shape Coefficients :
$$C_{\sigma_B}, C_{\varepsilon_B}, C_{\varepsilon_T} = \begin{cases} 1 & (C) \\ 0.6 & (S) \end{cases} \quad C_{\varepsilon_R} = \begin{cases} 1 & (C) \\ 1 & (S) \end{cases} \quad C_{\varepsilon_{BT}}, C_{\varepsilon_{TR}} = \begin{cases} 1 & (C) \\ 0.4 & (S) \end{cases}$$

Where:

E_{0BT}: Slope of the concrete after reaching the maximum strength.

F_0: Compressive strength of the unconfined concrete.

ε_0: Strain at F_0 for unconfined concrete.

p_f: Ratio of CFS.

E_f: Young Modulus of CFS.

ε_{fr}: Rupture strain of CFS.

5.3 Comparison between studied models and experimental results

From Figure 5-3, the comparison between Lam and Teng's model, Nakatsuka's model and the experimental results for circular shaped specimens, it can be observed that both models give a good approach in case of circular shaped specimens. This kind of specimens has an incremental stress in strain until failure, for this reason Lam and Teng's model can approach the envelope by using one slope after the transition point. Although Nakatsuka's model used two slopes to model the envelope after B-point, also gives a good approach. Both models give an ultimate point larger than the real one from experimental results, besides due to Lam and Teng's model shows a slight over strength, Nakatsuka's model is chosen to be modified.

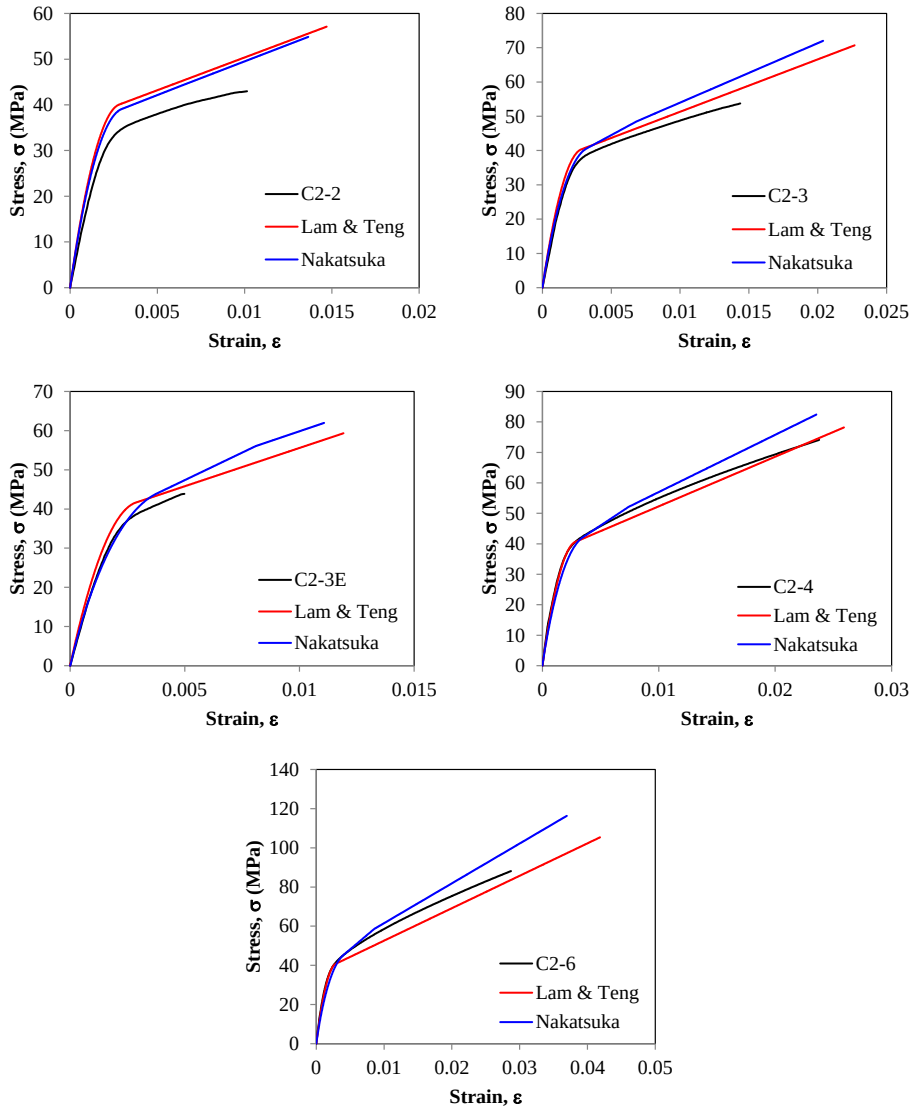

Figure 5-3 Theoretical models vs. experimental test – Circular shaped
Monotonic curves of concrete with CFS confinement

From Figure 5-4, the comparison between Lam and Teng's model, Nakatsuka's model and the experimental results for square shaped specimens, it can be observed that the envelope from experimental results has a strength reduction after the transition point (Lam and Teng's model) or B-point (Nakatsuka's model). Lam and Teng's model use only one slope after the transition point, for this reason the strength reduction cannot be modeled properly by using this model. On the other hand, Nakatsuka's model proposed two-slope model after reaching B-point; this model can be used to model the strength reduction in case of square shaped specimens. Nakatsuka's model needs to be improved due to the model does not have a good approach with the experimental results, this model will be modified to perform the approach.

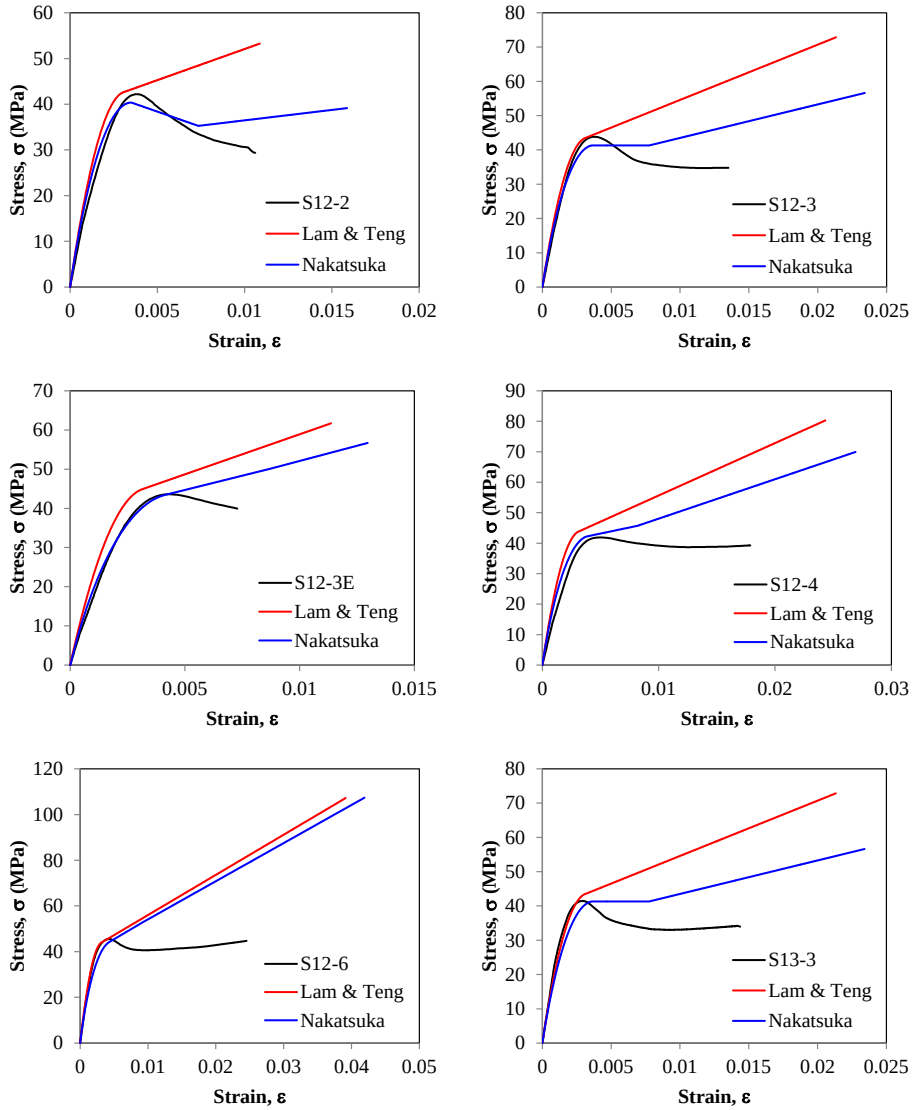

Figure 5-4 Theoretical models vs. experimental test – Square shaped

Monotonic curves of concrete with CFS confinement

5.4 Proposed modified Nakatsuka's model

5.4.1 Shape coefficients for circular shaped specimens

Regarding the shape coefficients for circular shaped specimens, the experimental data were used to find suitable coefficients. Figure 5-5 shows the result comparison between the experimental parameter of the envelope curve for circular shaped specimens versus the calculated values by using the proposed parameters.

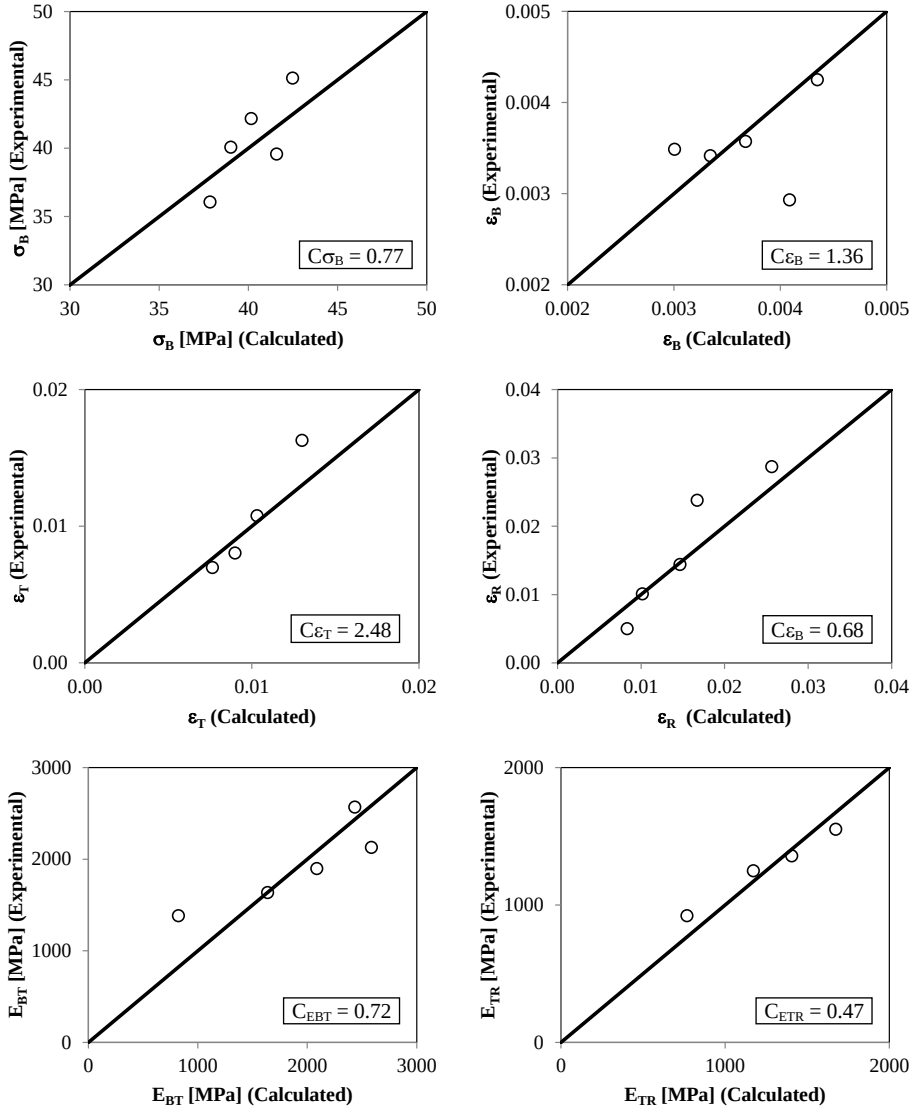

Figure 5-5 Modified shape coefficients – Circular shaped

Although the found coefficients are suitable for the circular shape specimen tested, Nakatsuka proposed a constant coefficient for all the coefficients as 1.00; this is based on the

procedure to get the formulated equations by Nakatsuka. Therefore the shape coefficients for circular shape specimen will be considered as the original model.

5.4.2 Shape coefficients for rectangular shaped specimens

Nakatsuka's model is considered for specimens with a chamfer radius of 30mm. The specimens used in this research has a chamfer radius of 15mm, this discrepancy is important when is considered the effective confinement area ratio between the effective confinement area under compression A_e and the section area of the concrete A_c. The effective confinement area is contained by four parabolas as is shown in Figure 5-6; with the initial slopes as the parabolas begin the same of the adjacent diagonal lines [2][17]. Therefore the effective confinement area ratio A_e/A_c is given by Equation (5-18).

$$\frac{A_e}{A_c} = \frac{1 - \frac{\left[\frac{d}{b}(b-2R)^2 + \frac{b}{d}(d-2R)^2\right]}{3A_g} - \rho_g}{1-\rho_g} \tag{5-18}$$

$$A_g = bd + (\pi - 4)R^2 \tag{5-19}$$

Where:

$b\ and\ d$: Dimension of the section of sample.

R: Chamfer radius at corners.

A_g: Gross-section area of the section defined by Equation (5-19).

ρ_g: Gross-section area ratio of the reinforcing steel.

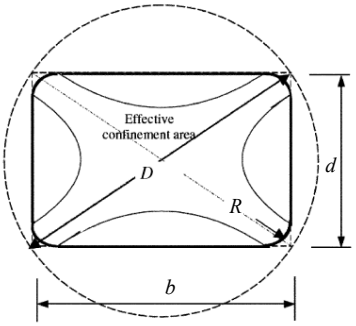

Figure 5-6 Effective confinement area of concrete

Table 5-2 shows the shape coefficients (following Nakatsuka's procedure) for R=15mm corresponding to $A_e/A_c = 0.57$, which are different from coefficients proposed by Nakatsuka for R=30mm corresponding to $A_e/A_c = 0.75$. Besides, taking into consideration circular shaped specimens (150mm of diameter) as an square shaped specimen with the highest chamfer radius possible R= 75mm corresponding to $A_e/A_c = 1.00$, and the minimum effective

confinement area ratio corresponding to $A_e/A_c = 0.33$. Using those coefficients, Equations (5-20) to (5-24) are proposed to calculate the shape coefficients for any chamfer radius with a range of effective confinement area ratio $0.33 \leq A_e/A_c \leq 1.00$, as is shown in Figure 5-7 to Figure 5-11 respectively.

Table 5-2 Shape coefficients for different chamfer radius

	R (mm)			
	0	15	30	75
C_{σ_B}	0.60	0.55	0.60	1.00
C_{ε_B}	0.60	0.60	0.60	1.00
C_{ε_T}	0.00	0.37	0.60	1.00
C_{ε_R}	0.00	0.52	0.40	1.00
$C_{E_{BT}}$	0.00	0.22	1.00	1.00
$C_{E_{TR}}$	0.00	0.13	0.40	1.00

a) Shape coefficient C_{σ_B} and C_{ε_B}.

Range of effective confinement area ratio: $0.33 \leq A_e/A_c \leq 1.00$.

Both shape coefficients are considered constant up to $A_e/A_c = 0.75$, then it is considered following a linear function up to $A_e/A_c = 1.00$

$$C_{\sigma_B} = C_{\varepsilon_B} = \begin{cases} 0.6 & if \quad 0.33 \leq \dfrac{A_e}{A_c} \leq 0.75 \\ 1.61\dfrac{A_e}{A_c} - 0.61 & if \quad 0.75 < \dfrac{A_e}{A_c} \leq 1.00 \end{cases} \tag{5-20}$$

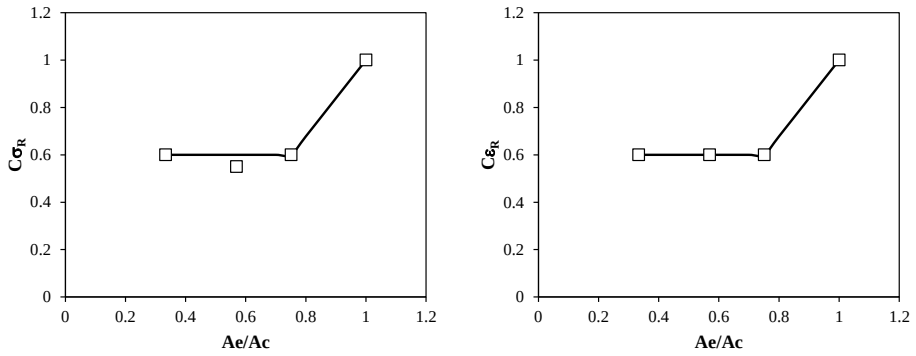

Figure 5-7 Effective confinement area of concrete

b) Shape coefficient C_{ε_T}.

Range of effective confinement area ratio: $0.33 \leq A_e/A_c \leq 1.00$.

The shape coefficient is considered following a linear function from $A_e/A_c = 0.33$ up to $A_e/A_c = 1.00$

$$C_{\varepsilon_T} = 1.48\frac{A_e}{A_c} - 0.49 \tag{5-21}$$

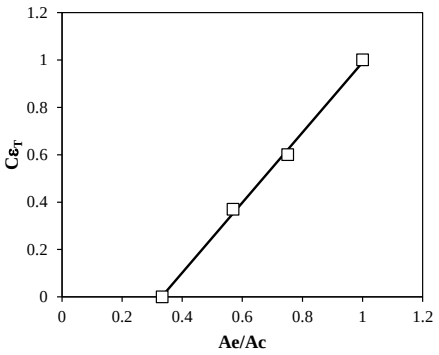

Figure 5-8 Effective confinement area of concrete

c) Shape coefficient C_{ε_R}.

Range of effective confinement area ratio: $0.33 \leq A_e/A_c \leq 1.00$.

The shape coefficient is considered following a linear function from $A_e/A_c = 0.33$ up to $A_e/A_c = 0.75$, then it is considered constant up to $A_e/A_c = 1.00$

$$C_{\varepsilon_R} = \begin{cases} 2.38\dfrac{A_e}{A_c} - 0.81 & if \quad 0.33 \leq \dfrac{A_e}{A_c} \leq 0.75 \\ 1 & if \quad 0.75 < \dfrac{A_e}{A_c} \leq 1.00 \end{cases} \tag{5-22}$$

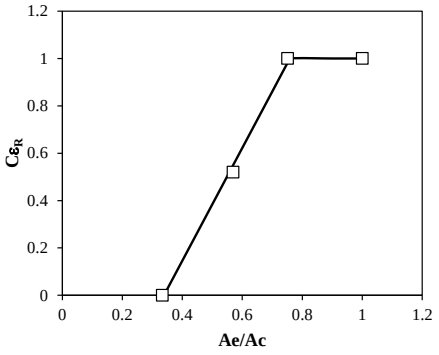

Figure 5-9 Effective confinement area of concrete

d) Shape coefficient $C_{\varepsilon_{BT}}$.

Range of effective confinement area ratio: $0.33 \leq A_e/A_c \leq 1.00$.

The shape coefficient is considered following a parabolic function from $A_e/A_c = 0.33$ up to $A_e/A_c = 1.00$

$$C_{\varepsilon_{BT}} = 1.77\left(\frac{A_e}{A_c}\right)^2 - 0.89\frac{A_e}{A_c} + 0.11 \quad (5\text{-}23)$$

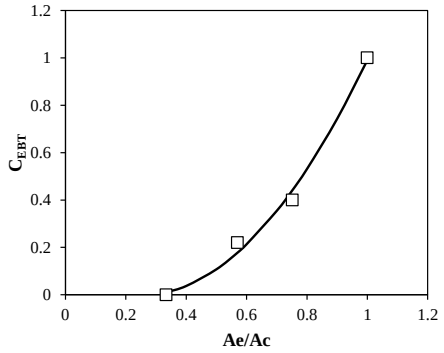

Figure 5-10 Effective confinement area of concrete

e) Shape coefficient $C_{\varepsilon_{TR}}$.

Range of effective confinement area ratio: $0.33 \leq A_e/A_c \leq 1.00$.

The shape coefficient is considered following a parabolic function from $A_e/A_c = 0.33$ up to $A_e/A_c = 1.00$

$$C_{\varepsilon_{TR}} = 2.19\left(\frac{A_e}{A_c}\right)^2 - 1.43 + 0.23 \quad (5\text{-}24)$$

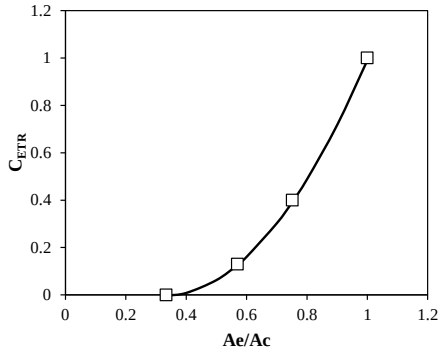

Figure 5-11 Effective confinement area of concrete

5.5 Comparison between proposed model and experimental results

By using the modified Nakatsuka's coefficients, the comparison between Nakatsuka's model and Modified Nakatsuka's model is shown in Figure 5-12. From Figure 5-12 can be observed that modified Nakatsuka's model gives a better approach to model the experimental envelope curves for square shaped specimens confined with CFS.

Specimen S12-2 and S12-3 underestimate the maximum strength of the envelope curve with a slight discrepancy. On the other hand, specimens S12-3E, S12-4 and S13-3 have a better approach with the experimental envelope curve in terms of maximum strength. Although specimen S12-4 has the best approach to the experimental envelope, also has a lower ultimate strain. Moreover, specimens S12-3 and S12-3E has larger ultimate strain. Other specimens have a good match of ultimate strain with experimental values.

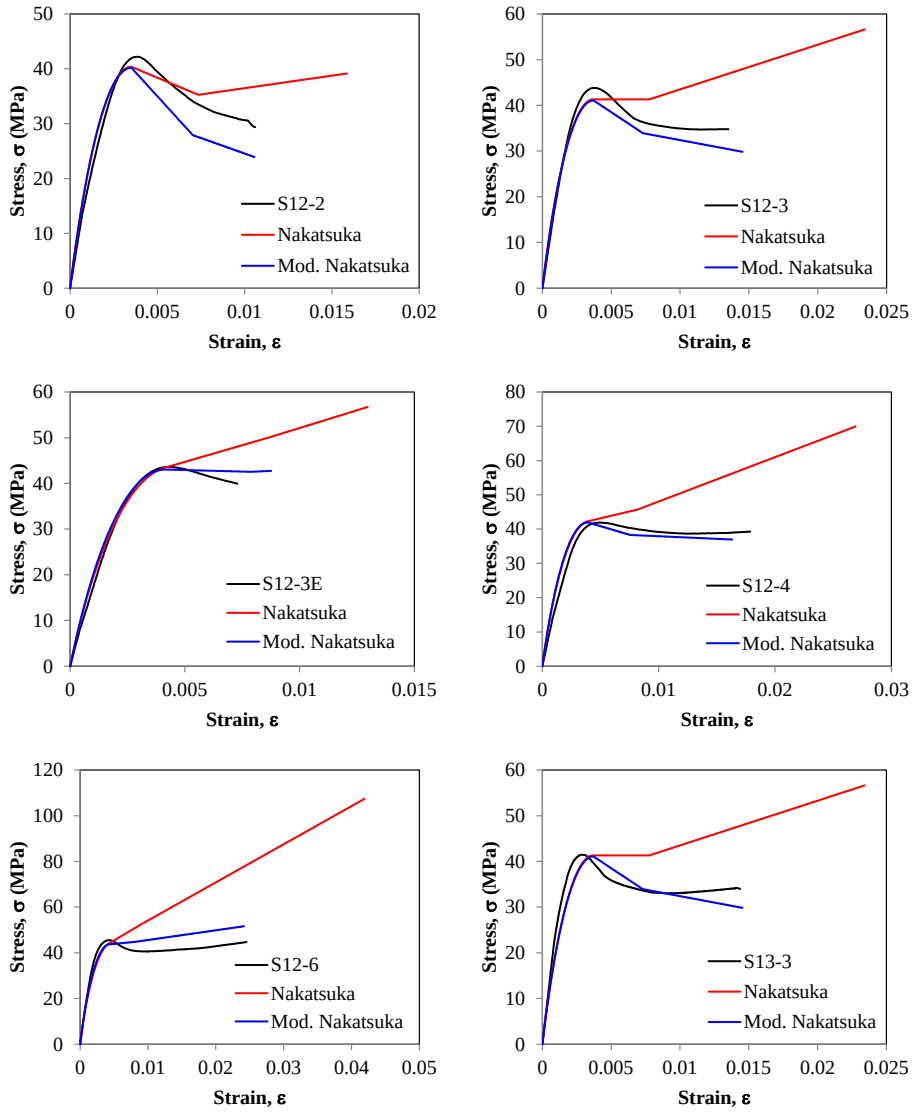

Figure 5-12 Proposed model vs. experimental test – Square shaped Monotonic curves of concrete with CFS confinement

CHAPTER 6

STRESS-STRAIN RELATIONSHIP OF CONCRETE WITH OR WITHOUT CFS CONFINEMENT UNDER CYCLIC LOADING

CHAPTER 6 : STRESS-STRAIN RELATIONSHIP OF CONCRETE WITH OR WITHOUT CFS CONFINEMENT UNDER CICLYC LOADING

6.1 Envelope curve of concrete

The equivalent uniaxial stress-strain curve of concrete in compression and tension shown in Figure 6-1 is based on the Modified Darwin & Pecknold [9], Noguchi [11][25], Naganuma [22], Lam & Teng [18] and Nakatsuka's Model [23]. Although several researches [7][10][26][41] show a good agreement in compression stage until the maximum compressive strength, Saenz et al. [30] proposal is adopted.

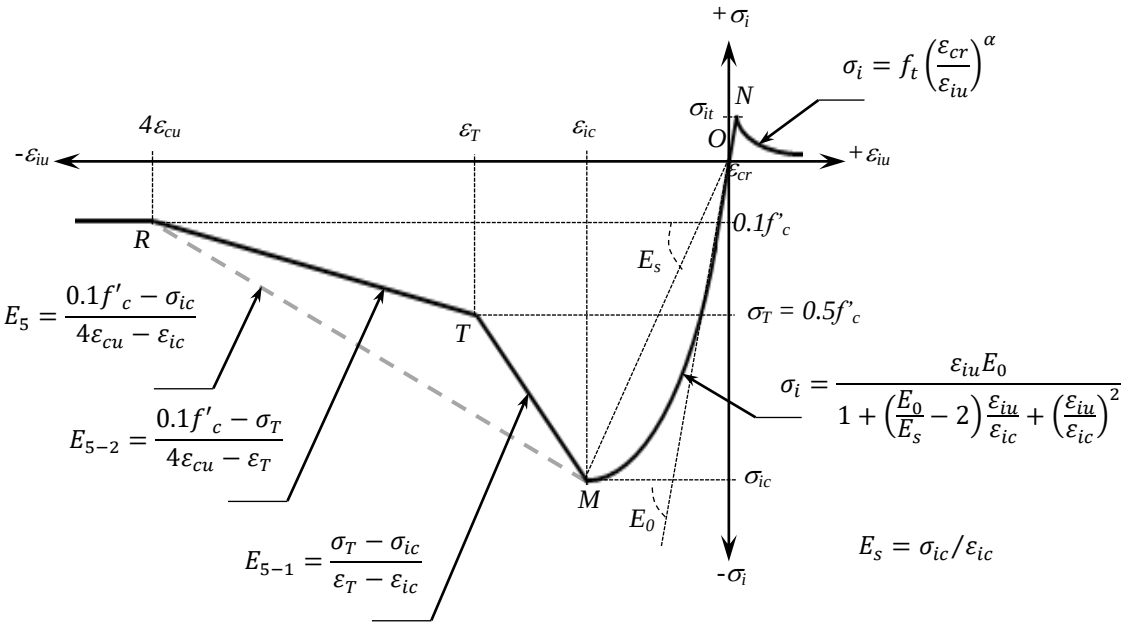

Figure 6-1 Proposed envelope curve for concrete

The envelope curve is composed by:

- *O→M*: Suggested by Saenz et al. [30], goes from the origin until the maximum strength of concrete f'_c (M).
- *M→T*: Linear portion after reaching the maximum strength of concrete, where the strength decreases until T-point.
- *T→R*: Linear portion, the strength continues decreasing until R-point ($4\varepsilon_{cu}$,$0.10\ f'_c$).
- *R →*: Flat portion where the strength remains constant at $0.10\ f'_c$ of strength.
- *O→N*: Linear portion with E_0 slope until the maximum tensile strength of concrete. [19]
- *N →*: Decreasing the strength of concrete with the opening crack of concrete. [36][37]

Where:

E_0: Tangent modulus of elasticity at zero stress.

E_s: Secant modulus at the point of maximum compressive stress, σ_{ic}.

ε_{ic}: Corresponding equivalent uniaxial strain at, σ_{ic}.

ε_{cu}: Real strain at f'_c from the compression test.

ε_{cr}: Equivalent uniaxial strain at σ_{it}, where the cracking starts

6.2 Loading, unloading and reloading in compression

The loading, unloading and reloading in compression are described From Level 1 to Level 5 as is shown in Figure 6-2. For the case in which the reloading takes place during Level 3 and before reaching zero stress (P), the reloading curve goes into Level 4, oriented to the common point (C) between the unloading curve and the reloading curve. Moreover, in case of unloading occurring over Level 4 and before reaching the common point (C), the unloading curve goes over a new Level 3, oriented to the same plastic strain (P). (See Figure 6-3) [29]

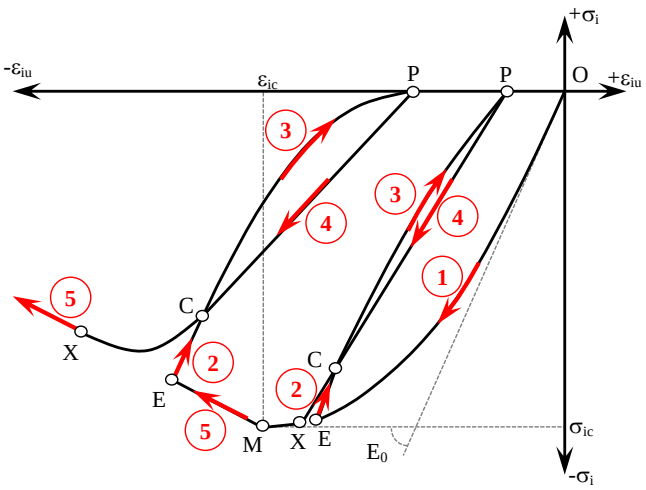

Figure 6-2 Loading, unloading and reloading in compression

From Figure 6-3, for the case in which a second unloading takes place after the concrete has been reloaded, and the unloading occurs after passing the common point (C) but has not yet reached the envelope curve, a new unloading curve is defined based on the projected point of unloading over the envelope curve. [29]

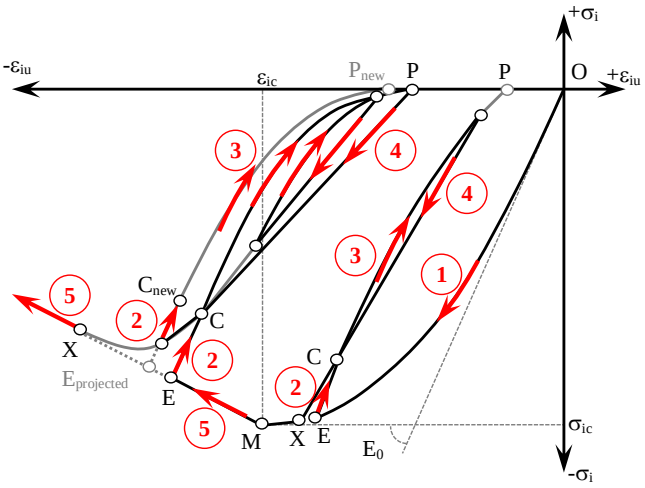

Figure 6-3 Internal cycles in compression

- *Level 1 – Loading Compressive Stage: O→M*

$$\sigma_i = \frac{\varepsilon_{iu} E_0}{1 + \left(\frac{E_0}{E_s} - 2\right)\frac{\varepsilon_{iu}}{\varepsilon_{ic}} + \left(\frac{\varepsilon_{iu}}{\varepsilon_{ic}}\right)^2} \tag{6-1}$$

- *Level 2 – Unloading Compressive Stage: M→C→M (Linear)*

$$E_2 = \frac{2\sigma_{en}}{\varepsilon_{en} - \varepsilon_p} \leq E_0 \tag{6-2}$$

Where:

Plastic Strain, (ε_P,0):

$$\varepsilon_P = \begin{cases} \left(0.145\left(\frac{\varepsilon_{en}}{\varepsilon_{cu}}\right)^2 + 0.13\left(\frac{\varepsilon_{en}}{\varepsilon_{cu}}\right)\right)\varepsilon_{cu}, & \varepsilon_{en} < \varepsilon_{ic} \\ (1.437 + 0.01 * \sigma_{ic})\varepsilon_{en} + 0.0023, & \varepsilon_{en} \geq \varepsilon_{ic} \end{cases} \tag{6-3}$$

Common Point, (ε_C,σ_C):

$$(\varepsilon_C, \sigma_C) = \left(\varepsilon_{en} - \frac{1}{6}\frac{\sigma_{en}}{E_2}, \frac{5}{6}\sigma_{en}\right) \tag{6-4}$$

- *Level 3 – Unloading Compressive Stage: C→P*

$$\sigma_i = a{\varepsilon_i}^n + b\varepsilon_i + c \tag{6-5}$$

To define Level 3, the n-degree function must satisfy the stress, strain and slope conditions at C and P, where the slope at P (E_P) is defined as follow:

$$E_P = \frac{\sigma_F}{\varepsilon_F - \varepsilon_P} \tag{6-6}$$

- *Level 4 – Reloading Compressive Stage: P→C (Linear), C→X (Parabolic)*

$$E_4 = \frac{\sigma_C}{\varepsilon_C - \varepsilon_P} \tag{6-7}$$

Level 4 is defined from the reloading point or plastic point as a linear function oriented to the common point using a slope E_4. For the case in which the strain is larger than the strain at C and before reaching the envelope curve, Level 4 follow a parabolic function satisfying the stress, strain and slope conditions at the common point, and the corresponding point over the envelope (X). [29]

- *Level 5-1 – Loading Compressive Stage: M→T (Linear)*

$$E_{5-1} = \frac{\sigma_T - \sigma_{ic}}{\varepsilon_T - \varepsilon_{ic}} \tag{6-8}$$

- *Level 5-2 – Loading Compressive Stage: T→R (Linear)*

$$E_{5-2} = \frac{0.1f'_c - \sigma_T}{4\varepsilon_{cu} - \varepsilon_T} \tag{6-9}$$

- *Level 5-3 – Loading Compressive Stage: R→ (Flat)*

$$\sigma_i = 0.1f'_c \tag{6-10}$$

In the case of concrete only, Level 5-3 is considered as it is shown above, for the case of concrete confined with CFS, Level 5-3 is not considered.

6.3 Loading, unloading and reloading in tension

The loading, unloading and reloading in tension are described from Level 6 to Level 8 as is shown in Figure 6-4. For the case in which the loading tensile stage takes place before loading compressive stage, then Level 6 will follow E_0 slope until reach the tensile concrete strength, $f_t = \sigma_{it}$. [29]

When the tensile stress of concrete in the principal i-direction exceeds the tensile concrete strength, σ_{it}, the first crack occur perpendicular to the principal i-direction. Then the stress decrease while the Crack width is in opening stage. [29]

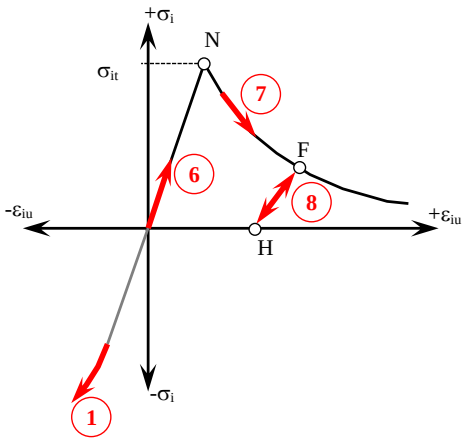

Figure 6-4 Loading, unloading and reloading in tension

- *Level 6 – Loading Tensile Stage: O→N (Linear)*

$$E_6 = E_0 \tag{6-11}$$

- *Level 7 – Crack Formation and Crack Opening: N→F*

$$\sigma_i = f_t \left(\frac{\varepsilon_{cr}}{\varepsilon_{iu}}\right)^{\alpha} \quad , \quad (\alpha = 1.0) \tag{6-12}$$

- *Level 8 – Drops linearly until Residual Deformation: F→H→F (Linear)*

$$E_8 = E_0^{\frac{\varepsilon_{cr}+r_y\varepsilon_F}{(r_y+1)\varepsilon_F}} \quad , \quad (r_y = 4.0) \tag{6-13}$$

Where the intersection point (I) defined by Level 8 and Level 10 is defined as:

$$\begin{aligned} \sigma_I &= 0.9\sigma_F \\ \varepsilon_I &= (\sigma_I - \sigma_F + E_8\varepsilon_F)/E_8 \end{aligned} \tag{6-14}$$

6.4 Transition from compression to tension and vice versa

The transition from compression to tension and from tension to compression is described by Level 9 and Level 10 as is shown in Figure 6-5. For the case in which an inner loop occurs in transition from Level 9 to 10 or Level 10 to 9, a linear function was proposed following a slope E_{11}; this slope can be obtained by interpolation between slope at J-point and E_8. (See Figure 6-6) [29]

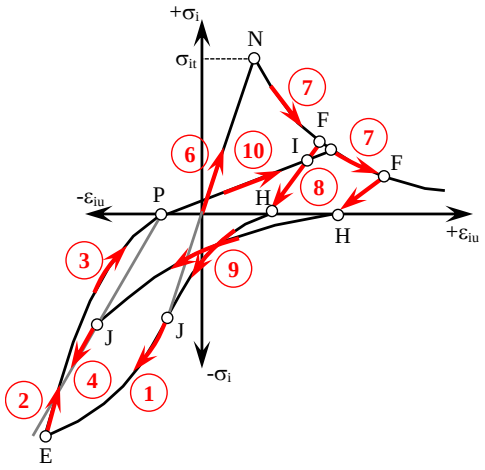

Figure 6-5 Transition from compression to tension and vice versa

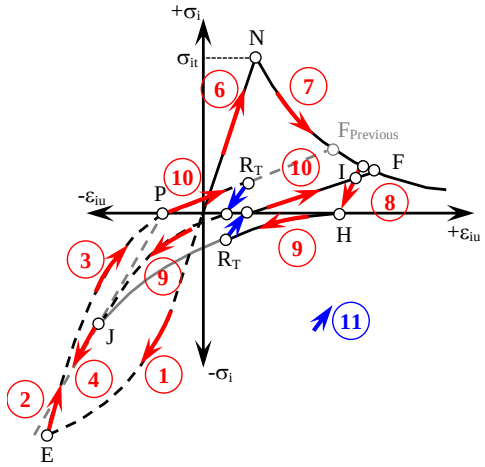

Figure 6-6 Inner loop in transition

- *Level 9 – Transition from Tensile Stage to Compressive Stage: H→J (Logarithmic)*

$$\sigma_i = (Ln(\varepsilon_i + a) + b)c \tag{6-15}$$

Where J-point is defined as follow:

$$\sigma_J = \beta\sigma_{it} \quad , \quad \beta = 1.0 + 0.02\left(\frac{\varepsilon_F - \varepsilon_{cr}}{\varepsilon_{cr}}\right) \tag{6-16}$$

- *Level 10 – Transition from Compressive Stage to Tensile Stage: P→F (Linear)*

$$E_{10} = \frac{\sigma_F}{\varepsilon_{cr} - \varepsilon_P} \tag{6-17}$$

- *Level 11 – Transition from Compressive Stage to Tensile Stage: RT→Zero stress (Linear)*

$$E_{11} = \frac{(\varepsilon_{RT} - \varepsilon_J)(E_8 - E_J)}{\varepsilon_H - \varepsilon_J} + E_J \quad (6\text{-}18)$$

Where ε_{RT} is the returning point in transition from either Level 9 to Level 10 or Level 10 to Level 9.

6.5 Envelope curve of concrete with CFS confinement

The envelope curve of concrete with CFS confinement is considered following Nakatsuka's model described in Section 4.2, considering the modified shape coefficients presented in Section 4.4. The hysteresis rules to describe the loading, unloading and reloading of concrete with CFS confinement follows the same rules from Level 1 to Level 11 which are described above. [29]

6.6 Plastic strain of concrete with CFS confinement

When considering the cyclic behavior for concrete with CFS confinement, the hysteresis rules are taken as the same as for the concrete only but changing the envelope curve and the plastic strain (ε_P) must be taken following Equation (6-19). [29]

Previous studies show the experimental linear relationship between envelope unloading strain and plastic strain [18][33] (See Table 6-1); including the linear relationship found in this study, Equation (6-19) shows a proposed expression for plastic strain by modifying the coefficients of Lam and Teng's equation for plastic strain of concrete retrofitted with CFS. The comparison between experimental and calculated plastic strain can be observed in Figure 6-7.

Table 6-1 Linear relationship between envelope unloading strain and plastic strain

Source	f'c (Mpa)	(a+cf'$_c$)	c	R^2
Reyna et al.	35.56	0.758	-0.0021	0.9982
	38.46	0.763	-0.0016	0.9997
Lam and Teng.	38.9	0.714	-0.0016	0.998
	41.1	0.703	-0.0014	0.996
Ilki and Kumbasar	32	0.713	-0.0019	0.994
Rousakis	49.5	0.737	-0.002	0.981
	65.5	0.601	-0.0015	0.981
	68.5	0.603	-0.0015	0.968
	95	0.467	-0.0013	0.999

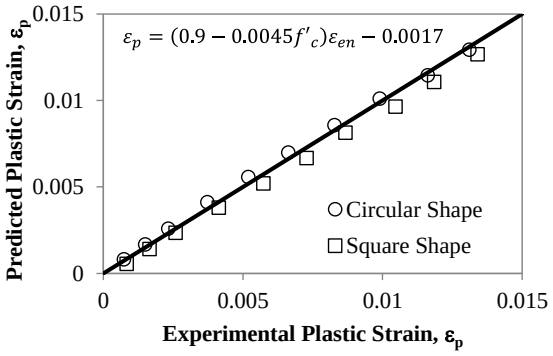

Figure 6-7 Comparison between experimental and calculated plastic strain

$$\varepsilon_P = \begin{cases} 0 \quad , \quad 0 < \varepsilon_{en} \leq 0.001 \\ [1.4(0.9 - 0.0045 * F_0) - 0.64](\varepsilon_{en} - 0.001) \quad , \quad 0.001 < \varepsilon_{en} \leq 0.035 \\ (0.9 - 0.0045 * F_0)\varepsilon_{en} - 0.0016 \quad , \quad 0.035 < \varepsilon_{en} \leq \varepsilon_R \end{cases} \tag{6-19}$$

6.7 Experimental results vs. analytical approach

6.7.1 Circular shaped specimens under cyclic test

Figure 6-8 and Figure 6-9 shows a comparison between experimental curves and analytical hysteresis curves for circular shaped specimens for both concrete only and concrete with CFS respectively. The comparison shows that proposed model and the experimental result match pretty well. The strain pattern used to get the analytical curve is shown in Figure 4-26. The calculated strain level for the rupture of the circular specimen of concrete with CFS is about the same level as the experimental test. Besides, the plastic strain definition for both, concrete only and concrete with CFS, has a good agreement between the experimental curve and the proposed model. [29]

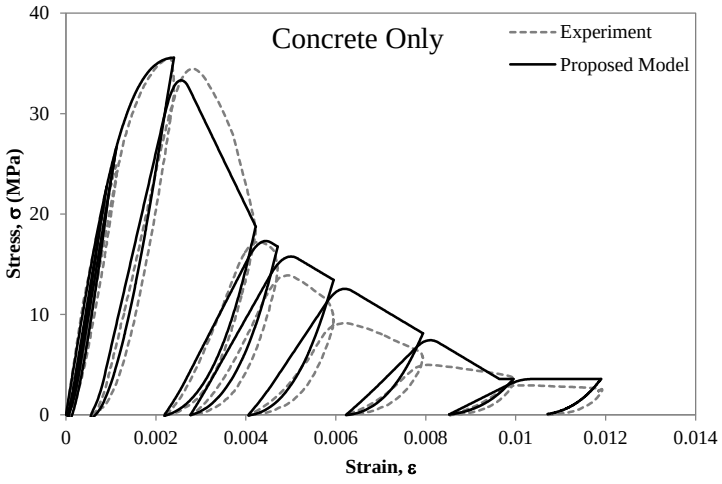

Figure 6-8 Experimental vs. proposed model – Circular shaped specimen

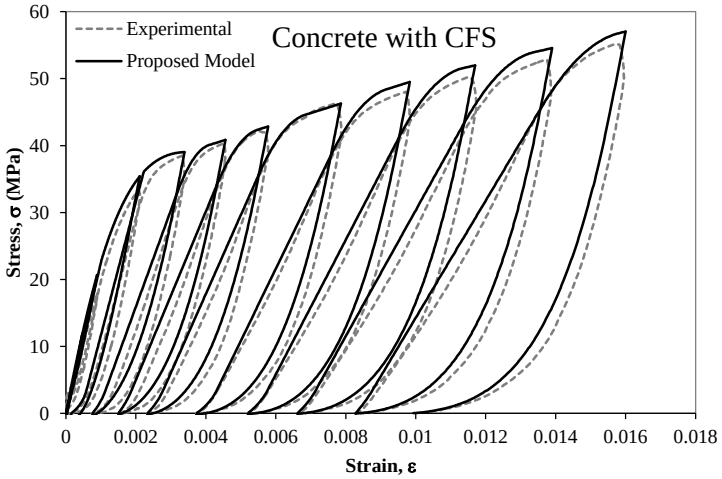

Figure 6-9 Experimental vs. proposed model – Circular shaped specimen

6.7.2 Square shaped specimens under cyclic test

Figure 6-10 and Figure 6-11 shows the comparison between experimental curves and analytical hysteresis curves for square shaped specimens for both concrete only and concrete with CFS respectively. The strain pattern used to get the analytical curve is shown in Figure 4-26. The comparison shows that proposed model and the experimental result match pretty well. The analytical model gives a lower strain level for the rupture of the square shaped specimen of concrete with CFS, but when it is compared with the monotonic curve it has about the same strain level for the rupture of the CFS during the test. [29]

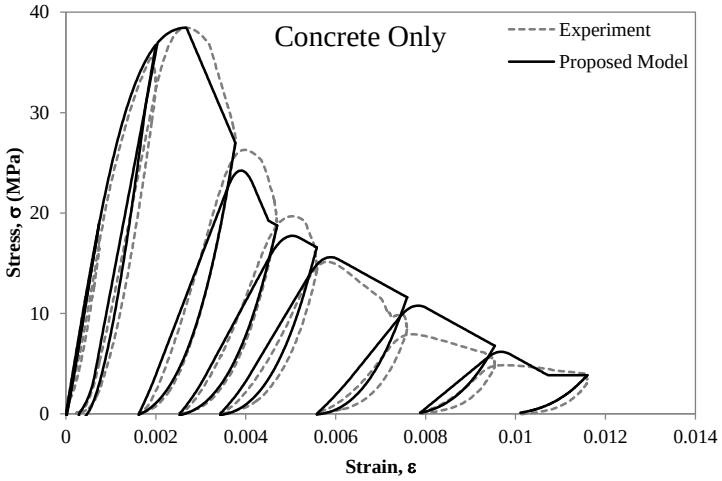

Figure 6-10 Experimental vs. proposed model – Square shaped specimen

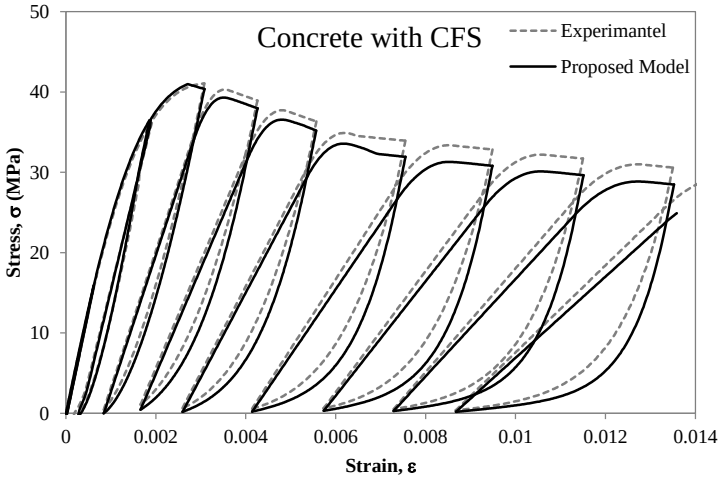

Figure 6-11 Experimental vs. proposed model – Square shaped specimen

CHAPTER 7

NONLINEAR FINITE ELEMENT ANALYSIS

CHAPTER 7 : NONLINEAR FINITE ELEMENT ANALYSIS

7.1 Material model of concrete under biaxial stress

7.1.1 Constitutive material model

The material behaves as elastic material between each incremental load step. Plain concrete has been idealized as an orthotropic material is suggested in Figure 7-1.[9][31]

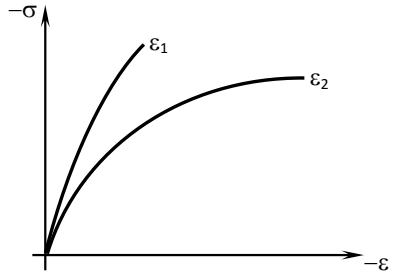

Figure 7-1 Behavior of Plain Concrete under Biaxial Compression

Thus, considering a planar element: (See Figure 7-2)

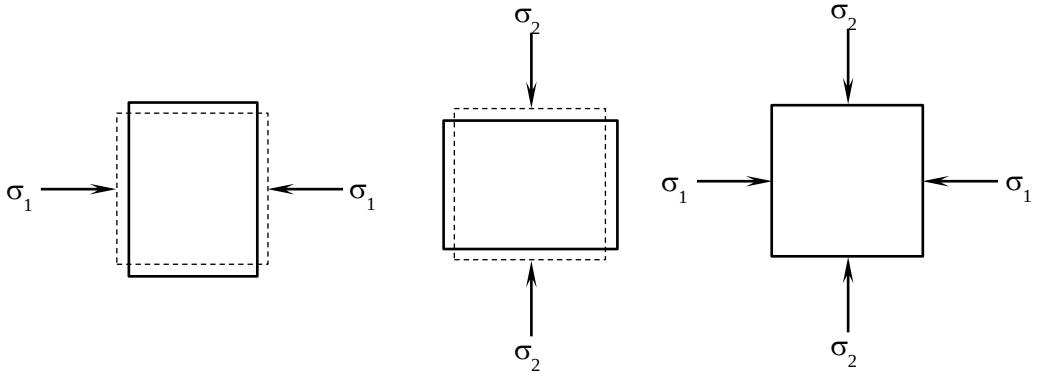

Figure 7-2 Deformation of planar element in principal axes

$$d\varepsilon_1 = \frac{d\sigma_1}{E_1} \qquad d\varepsilon_2 = \frac{d\sigma_2}{E_2} \qquad d\varepsilon_1 = \frac{d\sigma_1}{E_1} - \nu_2 \frac{d\sigma_2}{E_2}$$
$$d\varepsilon_2 = -\nu_1 \frac{d\sigma_1}{E_1} \qquad d\varepsilon_1 = -\nu_2 \frac{d\sigma_2}{E_2} \qquad d\varepsilon_2 = -\nu_1 \frac{d\sigma_1}{E_1} + \frac{d\sigma_2}{E_2} \tag{7-1}$$

Where E_1, E_2, ν_1, ν_2 are stress-dependent material properties.

$$\begin{Bmatrix} d\sigma_1 \\ d\sigma_2 \end{Bmatrix} = \frac{1}{1-\nu_1\nu_2}\begin{bmatrix} E_1 & \nu_2 E_1 \\ \nu_1 E_2 & E_2 \end{bmatrix}\begin{Bmatrix} d\varepsilon_1 \\ d\varepsilon_2 \end{Bmatrix} \tag{7-2}$$

From energy considerations:

$$d\sigma_1 d\varepsilon_1 = d\sigma_2 d\varepsilon_2$$

$$\frac{1}{1-\nu_1\nu_2}(E_1 d\varepsilon_1 + \nu_2 E_1 d\varepsilon_2)d\varepsilon_1 = \frac{1}{1-\nu_1\nu_2}(\nu_1 E_2 d\varepsilon_1 + E_2 d\varepsilon_2)d\varepsilon_2$$

$$E_1 d\varepsilon_1{}^2 + \nu_2 E_1 d\varepsilon_1 d\varepsilon_2 = \nu_1 E_2 d\varepsilon_1 d\varepsilon_2 + E_2 d\varepsilon_2{}^2$$

If $d\varepsilon \ll 1$ then $d\varepsilon^2 \approx 0$

$$\nu_2 E_1 d\varepsilon_1 d\varepsilon_2 = \nu_1 E_2 d\varepsilon_1 d\varepsilon_2$$

$$\nu_2 E_1 = \nu_1 E_2$$

Introducing an equivalent Poisson's ratio: $\nu^2 = \nu_1\nu_2$

$$\begin{Bmatrix} d\sigma_1 \\ d\sigma_2 \end{Bmatrix} = \frac{1}{1-\nu^2}\begin{bmatrix} E_1 & \nu\sqrt{E_1E_2} \\ \nu\sqrt{E_1E_2} & E_2 \end{bmatrix}\begin{Bmatrix} d\varepsilon_1 \\ d\varepsilon_2 \end{Bmatrix} \tag{7-3}$$

Including the shear strain into the Equation (7-3):

$$\begin{Bmatrix} d\sigma_1 \\ d\sigma_2 \\ d\tau_{12} \end{Bmatrix} = \frac{1}{1-\nu^2}\begin{bmatrix} E_1 & \nu\sqrt{E_1E_2} & 0 \\ \nu\sqrt{E_1E_2} & E_2 & 0 \\ 0 & 0 & (1-\nu^2)G \end{bmatrix}\begin{Bmatrix} d\varepsilon_1 \\ d\varepsilon_2 \\ d\gamma_{12} \end{Bmatrix} \tag{7-4}$$

Finally the stress strain relationship is as follow:

$$d\sigma = Dd\varepsilon$$

$$D = \frac{1}{1-\nu^2}\begin{bmatrix} E_1 & \nu\sqrt{E_1E_2} & 0 \\ \nu\sqrt{E_1E_2} & E_2 & 0 \\ 0 & 0 & (1-\nu^2)G \end{bmatrix} \tag{7-5}$$

For rotation of principal axes of planar element, considering an element, and assuming the area corresponding to each lateral plane is 1 and the element rotate an angle θ, then from force equilibrium in the Figure 7-3, the principal stresses rotated are given by:

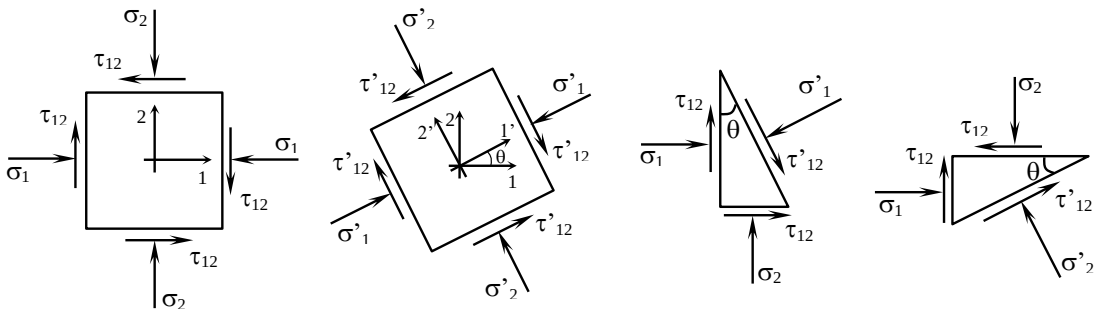

Figure 7-3 Rotation of principal axis of planar element

$$\sigma_1' = \sigma_1 cos^2\theta + \sigma_2 sin^2\theta + 2\tau_{12} sin\theta cos\theta$$
$$\sigma_2' = \sigma_1 sin^2\theta + \sigma_2 cos^2\theta - 2\tau_{12} sin\theta cos\theta \quad (7\text{-}6)$$
$$\tau_{12}' = -\sigma_1 sin\theta cos\theta + \sigma_2 sin\theta \cos\theta + \tau_{12}(cos^2\theta - sin^2\theta)$$

Considering a very small element:

$$\begin{Bmatrix} d\sigma_1' \\ d\sigma_2' \\ d\tau_{12}' \end{Bmatrix} = \begin{bmatrix} cos^2\theta & sin^2\theta & 2sin\theta cos\theta \\ sin^2\theta & cos^2\theta & -2sin\theta cos\theta \\ -sin\theta cos\theta & sin\theta cos\theta & cos^2\theta - sin^2\theta \end{bmatrix} \begin{Bmatrix} d\sigma_1 \\ d\sigma_2 \\ d\tau_{12} \end{Bmatrix} \quad (7\text{-}7)$$
$$d\sigma' = A d\sigma$$

Where A is the matrix that transform stresses between axes. Also strain vector can be expressed as follow:

$$\begin{Bmatrix} \varepsilon'_1 \\ \varepsilon'_2 \\ \frac{1}{2}\gamma'_{12} \end{Bmatrix} = A \begin{Bmatrix} \varepsilon_1 \\ \varepsilon_2 \\ \frac{1}{2}\gamma_{12} \end{Bmatrix}$$

Defining R matrix:

$$R = \begin{bmatrix} 1 & 0 & 0 \\ 0 & 1 & 0 \\ 0 & 0 & 2 \end{bmatrix} \qquad R^{-1} = \begin{bmatrix} 1 & 0 & 0 \\ 0 & 1 & 0 \\ 0 & 0 & 1/2 \end{bmatrix}$$

$$\begin{Bmatrix} \varepsilon'_1 \\ \varepsilon'_2 \\ \gamma'_{12} \end{Bmatrix} = R \begin{Bmatrix} \varepsilon'_1 \\ \varepsilon'_2 \\ \frac{1}{2}\gamma'_{12} \end{Bmatrix}$$

$$\begin{Bmatrix} \varepsilon'_1 \\ \varepsilon'_2 \\ \gamma'_{12} \end{Bmatrix} = RA \begin{Bmatrix} \varepsilon_1 \\ \varepsilon_2 \\ \frac{1}{2}\gamma_{12} \end{Bmatrix}$$

$$\begin{Bmatrix} \varepsilon'_1 \\ \varepsilon'_2 \\ \gamma'_{12} \end{Bmatrix} = RAR^{-1} \begin{Bmatrix} \varepsilon_1 \\ \varepsilon_2 \\ \gamma_{12} \end{Bmatrix}$$

$$\begin{Bmatrix} \varepsilon'_1 \\ \varepsilon'_2 \\ \gamma'_{12} \end{Bmatrix} = \begin{bmatrix} cos^2\theta & sin^2\theta & sin\theta cos\theta \\ sin^2\theta & cos^2\theta & -sin\theta cos\theta \\ -2sin\theta cos\theta & 2sin\theta cos\theta & cos^2\theta - sin^2\theta \end{bmatrix} \begin{Bmatrix} \varepsilon_1 \\ \varepsilon_2 \\ \gamma_{12} \end{Bmatrix} \tag{7-8}$$

$$d\varepsilon' = Bd\varepsilon$$

Where B is the matrix that transforms strain between axes.

From Equation (7-5), and using Equations (7-7) and (7-8):

$$A^{-1}d\sigma' = DB^{-1}d\varepsilon'$$
$$AA^{-1}d\sigma' = ADB^{-1}d\varepsilon$$
$$d\sigma' = ADB^{-1}d\varepsilon' \tag{7-9}$$

From Equation (7-9), stress-strain relationship can be expressed using axes rotation as follows:

$$d\sigma' = D'd\varepsilon' \tag{7-10}$$

Where D' can be defined as follows:

$$D' = ADB^{-1}$$
$$B^{-1} = A^T$$
$$D' = ADA^T \tag{7-11}$$

Where:

$$A = \begin{bmatrix} cos^2\theta & sin^2\theta & 2sin\theta cos\theta \\ sin^2\theta & cos^2\theta & -2sin\theta cos\theta \\ -sin\theta cos\theta & sin\theta cos\theta & cos^2\theta - sin^2\theta \end{bmatrix}$$

From Equation (7-10) and Equation (7-11), G' is calculated as follow:

$$d\tau'_{12} = G'd\gamma'_{12} \tag{7-12}$$

$$D' = \frac{1}{1-\nu^2}\begin{bmatrix} c^2 & s^2 & 2sc \\ s^2 & c^2 & -2sc \\ -sc & sc & c^2 - s^2 \end{bmatrix}\begin{bmatrix} E_1 & \nu\sqrt{E_1E_2} & 0 \\ \nu\sqrt{E_1E_2} & E_2 & 0 \\ 0 & 0 & (1-\nu^2)G \end{bmatrix}\begin{bmatrix} c^2 & s^2 & -sc \\ s^2 & c^2 & sc \\ 2sc & -2sc & c^2 - s^2 \end{bmatrix}$$

$$G' = \frac{sin^2\theta cos^2\theta\left(E_1 + E_2 - 2\nu\sqrt{E_1E_2}\right)}{1-\nu^2} + (cos^2\theta - sin^2\theta)^2 G \tag{7-13}$$

Taking into consideration: $G = G'$

$$G = G' = \frac{1}{4}\frac{\left(E_1 + E_2 - 2\nu\sqrt{E_1E_2}\right)}{1-\nu^2} \tag{7-14}$$

Going back to the Equation (7-5) and using Equation (7-14):

$$\begin{Bmatrix} d\sigma_1 \\ d\sigma_2 \\ d\tau_{12} \end{Bmatrix} = \frac{1}{1-\nu^2}\begin{bmatrix} E_1 & \nu\sqrt{E_1E_2} & 0 \\ \nu\sqrt{E_1E_2} & E_2 & 0 \\ 0 & 0 & \frac{1}{4}\left(E_1 + E_2 - 2\nu\sqrt{E_1E_2}\right) \end{bmatrix}\begin{Bmatrix} d\varepsilon_1 \\ d\varepsilon_2 \\ d\gamma_{12} \end{Bmatrix} \quad (7\text{-}15)$$

Where E_1, E_2 and ν are determined as a function of the stress and strain state at each incremental load step. Finally stress depends on Young's modulus in each principal directions and the equivalent Poisson's ratio only: $\sigma = f(E_1, E_2, \nu)$.

7.1.2 Equivalent Uniaxial Strain

The concept of Equivalent Uniaxial Strain was developed in order to keep track of the degradation of stiffness and strength of plain concrete and to allow actual biaxial stress-strain curves to be duplicated from uniaxial curves. Figure 7-4 shows that may for a single value of stress correspond to a many values of strain. Therefore, the stiffness and strength of the concrete has strongly stress-strain dependency. [9][31]

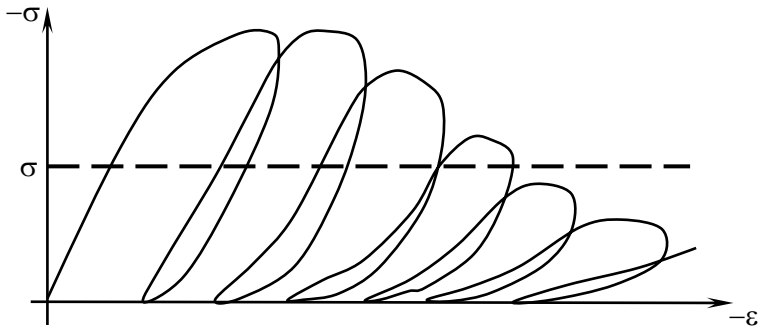

Figure 7-4 Cyclic loading of concrete

For biaxial state of stress, the strain in one direction is a function not only of stress in that direction, but also of the stress in the orthogonal direction, due to the Poisson ratio effect as is presented in Equation (7-5).

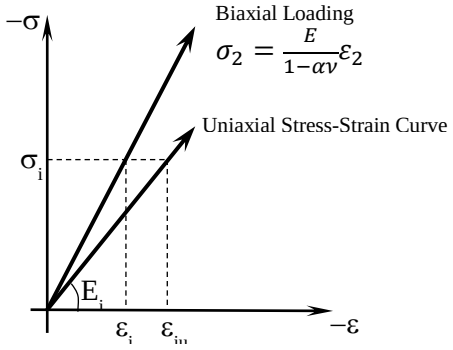

Figure 7-5 Equivalent uniaxial strain for linear material

For a linear elastic material, the equivalent uniaxial strain in i-th direction ε_{iu}, is given by:

$$\varepsilon_{iu} = \frac{\sigma_i}{E_i} \tag{7-16}$$

Where ε_{iu} may be thought of as the strain that would exist in i-th direction for zero stress in j-th direction. Considering a nonlinear material, Equation (7-16) can be written as follow:

$$\varepsilon_{iu} = \int d\varepsilon_{iu} = \int \frac{d\sigma_i}{E_i} \tag{7-17}$$

Where $d\sigma_i$ and $d\varepsilon_{iu}$ are differential stress and uniaxial strain in i-th direction respectively, and E_i is the tangent modulus of elasticity in i-th direction in each incremental step. Considering a finite numbers of increments $\Delta\sigma$, Equation (7-17) can be expressed as follow:

$$\varepsilon_{iu} = \sum \frac{\Delta\sigma_i}{E_i} \tag{7-18}$$

For every step, the change of the equivalent uniaxial strain, $\Delta\varepsilon_{iu}$, is given by:

$$\Delta\varepsilon_{iu} = \frac{\sigma_{i,new} - \sigma_{i,old}}{E_i} \tag{7-19}$$

Figure 7-6 shows the state of stress at the beginning and at the end of each load increment. Where $\sigma_{i,old}$ corresponds to the original i-axis, $\sigma_{i,new}$ corresponds to the new i-axis and E_i represents the tangent modulus in the i-th direction at the start of the load increment.

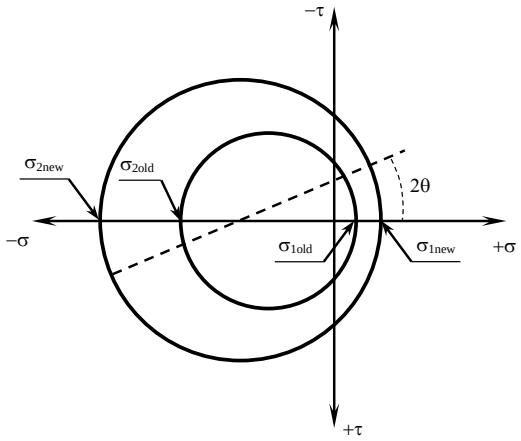

Figure 7-6 Rotation of principal stress axis

In addition, the actual equivalent uniaxial strain at loading step "k" will be given by:

$$\varepsilon_{iu(k)} = \varepsilon_{iu(k-1)} + \Delta\varepsilon_{iu(k)} \tag{7-20}$$

To consider the inelastic behavior, axis rotations must be allowed, thus the tangent stiffness E_1 and E_2, always represent the modulus corresponding to the principal and maximum value of stress. It is possible, even through small load increments, for the material axis to rotate more than 90°, this is undesirable since the stress and uniaxial strain history developed at one orientation should continue to control the behavior of material in essentially the same orientation. Therefore, the rotation of the material axis is limited to the 90° regions oriented with the initial principal axis. If the material axis change the region due to the load increment, then the material axis are reoriented to coincide with the principal stress axis within their respective regions, as is shown in Figure 7-7. [9]

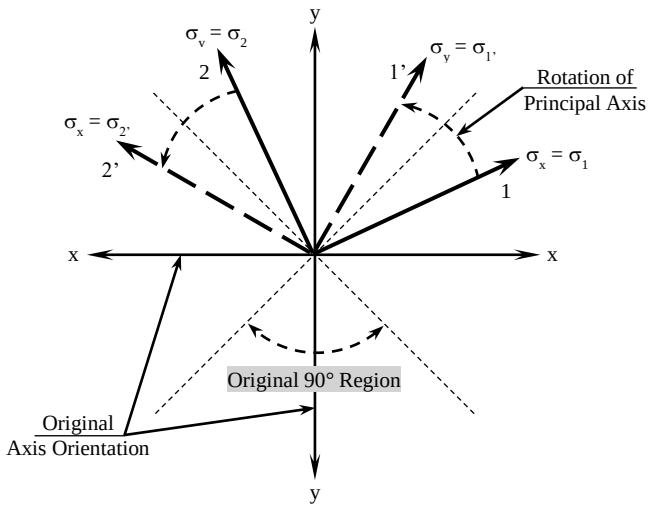

Figure 7-7 Rotation of principal stress axis out of originally defined regions

7.1.3 Maximum Stress Surface of concrete

For biaxial compression, Kupfer and Gerstle [14] found that the total strength envelope can be approximated by the following expression:

$$\left(\frac{\sigma_1}{f'_c}+\frac{\sigma_2}{f'_c}\right)^2-\frac{\sigma_2}{f'_c}-3.65\frac{\sigma_1}{f'_c}=0 \tag{7-21}$$

For compression-compression state, considering $\sigma_1 \geq \sigma_2$, and defining α as the ratio of σ_1 and σ_2 ($\alpha = \sigma_1/\sigma_2$), then Equation (2-34) can be written to give the maximum concrete compressive strength, σ_{2c}, as follow:

$$\sigma_{2c}=\frac{1+3.65\alpha}{(1+\alpha)^2}f'_c \tag{7-22}$$

Besides, the compressive stress in the orthogonal direction will be:

$$\begin{gathered}\sigma_{1c}=\alpha\sigma_{2c}\\ \sigma_{1c}=\alpha\frac{1+3.65\alpha}{(1+\alpha)^2}f'_c\end{gathered} \tag{7-23}$$

The values of σ_1 and σ_2 define the shape of the equivalent uniaxial stress-strain curves for a given value of α. Considering tension-compression state over plain concrete, σ_{1t}, Kupfer and Gerstle suggest [14] the following expression:

$$\sigma_{1t}=\left(1-0.8\frac{\sigma_2}{f'_c}\right)f'_t \tag{7-24}$$

On the other hand, Darwin and Pecknold [9] propose for tension-compression zone, the compressive stress-strain curve is modeled using the following expression:

$$\begin{gathered}\sigma_{2c}=\frac{1+3.28\alpha}{(1+\alpha)^2}f'_c \quad , \quad \sigma_{2c}\leq 0.65f'_c\\ \sigma_{1t}=f'_t\end{gathered} \tag{7-25}$$

In case of tension-compression state with $\sigma_{2c} > 0.65f'_c$ and for tension-tension state, Kupfer and Gerstle [14] recommended a constant tensile strength, equal to the uniaxial tensile strength of the material. This is in close agreement with the findings of other investigations [15][24].

$$\sigma_{1t}=\sigma_{2t}=f'_t \tag{7-26}$$

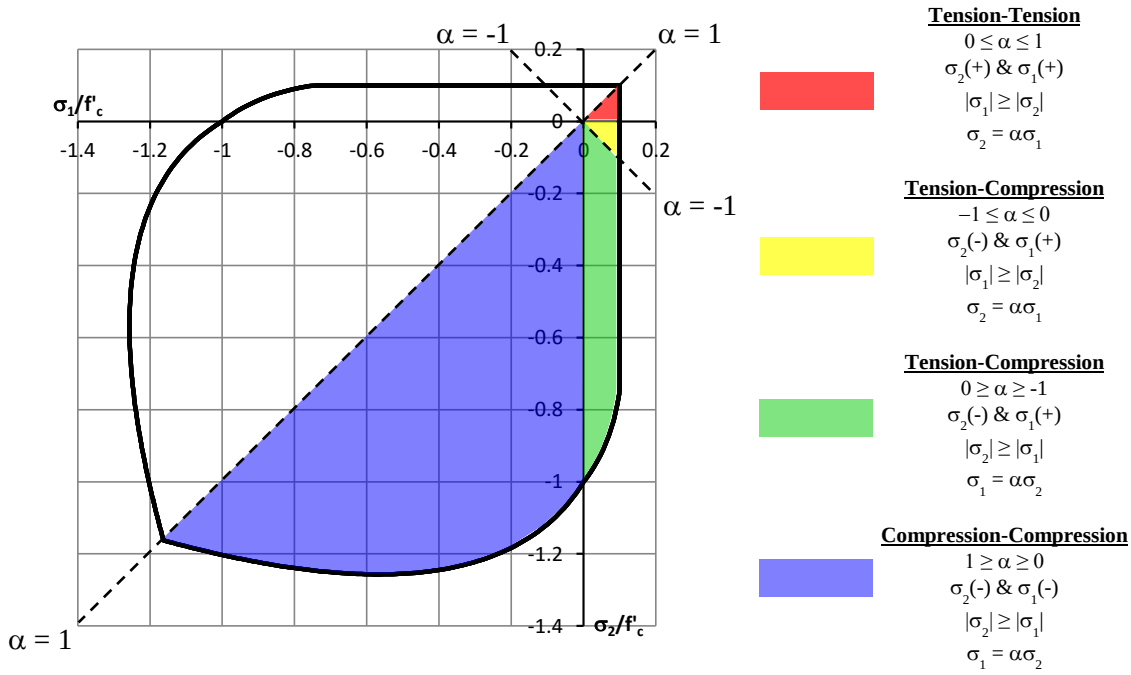

Figure 7-8 Analytical biaxial stress envelope by Darwin and Pecknold

7.1.4 Equivalent uniaxial strain ε_{ic} at σ_{ic}

To determine ε_{ic}, defined as equivalent uniaxial strain corresponding to the maximum compressive stress σ_{ic}, a constant value of Poisson's ratio $(\nu = 0.2)$ is assumed. Kupfer, Hilsdorf and Rusch [15] found that the Poisson's ratio remained essentially constant up to 80% of the ultimate load.[9]

When $|\sigma_{ic}| \geq |f'_c|$, ε_{ic} is assumed to vary linearly with σ_{ic} as:

$$\varepsilon_{ic} = \varepsilon_{cu}\left(\frac{\varepsilon_{ic}}{f'_c}R - (R-1)\right) \tag{7-27}$$

Where ε_{cu} is the strain at peak stress for the real uniaxial curve and f'_c is the uniaxial compressive strength of concrete. R is defined as follows:

$$R = \frac{\frac{\varepsilon_{ic(\alpha=1)}}{\varepsilon_{cu}} - 1}{\frac{\sigma_{ic(\alpha=1)}}{f'_c} - 1} \approx 3.15 \tag{7-28}$$

When $|\sigma_{ic}| < |f'_c|$, ε_{ic} is expressed by the following equation:

$$\varepsilon_{ic} = \varepsilon_{cu}\left(-1.6\left(\frac{\sigma_{ic}}{f'_c}\right)^3 + 2.25\left(\frac{\sigma_{ic}}{f'_c}\right)^2 + 0.35\left(\frac{\sigma_{ic}}{f'_c}\right)\right) \tag{7-29}$$

7.1.5 Effective Poisson's ratio

The Poisson's ratio assumed ($\nu = 0.2$), proved quite satisfactory for monotonic loading in tension-tension and compression-compression. Besides, this value proved to be adequate for uniaxial compression and tension-compression at low values of stress. However for values of stress above 80% of f'_c, the Poisson's ratio assumed is too small. Thus Poisson's ratio is assumed to be equal to 0.2 until 80% of f'_c, after that, Poisson's ratio of concrete starts to increase.[9]

For tension-tension and compression-compression state:

$$\nu = 0.2 \tag{7-30}$$

For uniaxial compression and tension-compression state:

$$\nu = 0.2 + 0.6\left(\frac{\sigma_2}{f'_c}\right)^4 + 0.4\left(\frac{\sigma_1}{\sigma_{1t}}\right)^4 < 1.00 \tag{7-31}$$

7.1.6 Cracking

For the proposed model, cracking first occurs when the tensile strength of concrete is exceeded, thus, a crack is formed perpendicular to the principal direction in tensile state, when the principal stress in the concrete exceeds the tensile strength in that direction. [9]

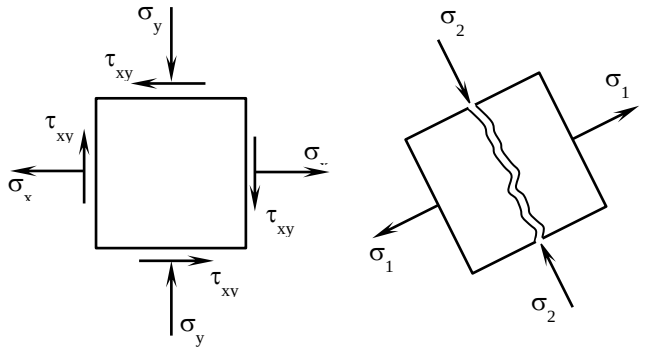

Figure 7-9 Crack in principal tension direction

For one open crack, considering 1-direction reaches the tensile concrete strength, $E_1 = 0$, therefore going back to the Equation (7-15).

$$\begin{Bmatrix} d\sigma_1 \\ d\sigma_2 \\ d\tau_{12} \end{Bmatrix} = \begin{bmatrix} 0 & 0 & 0 \\ 0 & E_2 & 0 \\ 0 & 0 & E_2/4 \end{bmatrix} \begin{Bmatrix} d\varepsilon_1 \\ d\varepsilon_2 \\ d\gamma_{12} \end{Bmatrix} \tag{7-32}$$

Where the crack is perpendicular to the 1-direction.

For the case of two open cracks:

$$\begin{Bmatrix} d\sigma_1 \\ d\sigma_2 \\ d\tau_{12} \end{Bmatrix} = \begin{Bmatrix} 0 \\ 0 \\ 0 \end{Bmatrix} \tag{7-33}$$

Just after the crack is formed, the crack width, C_{wi}, is defined as follow:

$$C_{wi} = \frac{\sigma_{cri}}{E_i} + \sum_{\substack{Load\ increments \\ following\ crack \\ formation}} (\Delta\varepsilon_i + \nu\Delta\varepsilon_j) \tag{7-34}$$

Where σ_{cri} is the stress that cause the crack and E_i is the tangent stiffness that was assumed just prior to the crack formation, $\Delta\varepsilon_i$ and $\Delta\varepsilon_j$ are the true strain increments perpendicular and parallel to the crack respectively, and $\nu = 0.2$, unless $\nu = 0$ if two cracks are open.

7.2 Material model of reinforcing steel

7.2.1 Smeared model

Cracks and reinforcing bars are idealized as being distributed or smeared over the concrete element at a certain angle orientation. The nonlinearity of a cracked RC element is primarily due to cracking, reinforcement plasticity and bond interaction between concrete and reinforcement. [31]

It has to be noted that the averaged stress-strain relation for the reinforcement differs from that of bare bars with no interaction with the concrete. Here the averaged stress-strain relation of concrete normal to the crack is much different from that of plain concrete with no interaction with reinforcement. [31]

At cracks, concrete tensile local stress is almost zero but the other local stress of concrete is still in tension. Thus, the average tensile stress remains non-zero, which is attributed to the bond between deformed bars and concrete. [31]

In this research, perfect bond between concrete and steel is assumed. In this model, the reinforcing bars inside a concrete element are replaced by an equivalent steel element with

distributed uniaxial material properties in a reinforcing direction. The thickness of the equivalent steel element t_s can be obtained as follows:

$$t_s = \frac{A_s}{b} \tag{7-35}$$

Where:

A_s: Cross-section of a bar.
d: Depth of the member.
b: Spacing of bars.

Considering one-direction reinforcing bar as is shown in Figure 7-10.

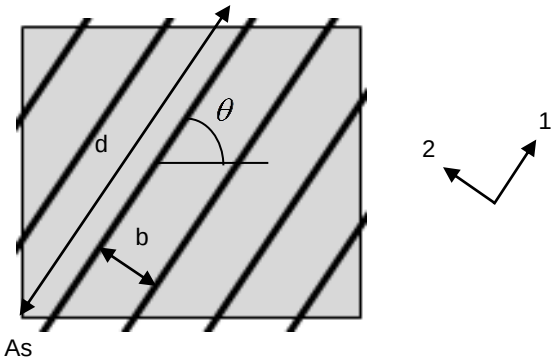

Figure 7-10 One-direction smeared model

Since the equivalent steel element has uniaxial properties in the direction parallel to the axis of the reinforcing bars, the constitutive matrix is defines as follows:

$$\begin{Bmatrix} d\sigma_1 \\ d\sigma_2 \\ d\tau_{12} \end{Bmatrix} = \begin{bmatrix} E_s & 0 & 0 \\ 0 & 0 & 0 \\ 0 & 0 & 0 \end{bmatrix} \begin{Bmatrix} d\varepsilon_1 \\ d\varepsilon_2 \\ d\gamma_{12} \end{Bmatrix} = D_s \begin{Bmatrix} d\varepsilon_1 \\ d\varepsilon_2 \\ d\gamma_{12} \end{Bmatrix}$$
$$D_s = \begin{bmatrix} E_s & 0 & 0 \\ 0 & 0 & 0 \\ 0 & 0 & 0 \end{bmatrix} \tag{7-36}$$

The constitutive matrix needs to be transformed to the global coordinate using the rotation matrix as shown in Equation (7-11):

$$\begin{Bmatrix} d\sigma_x \\ d\sigma_y \\ d\tau_{xy} \end{Bmatrix} = AD_sA^T \begin{Bmatrix} d\varepsilon_x \\ d\varepsilon_y \\ d\gamma_{xy} \end{Bmatrix} = D'_s \begin{Bmatrix} d\varepsilon_x \\ d\varepsilon_y \\ d\gamma_{xy} \end{Bmatrix}$$
$$D'_s = AD_sA^T \tag{7-37}$$

The stiffness matrix is a summation of those of concrete and steel as follows:

$$K = K_{concrete} + K_{steel}$$

$$K = t_c \int_{V(x,y)} B^T D_c B dxdy + t_s \int_{V(x,y)} B^T D'_s B dxdy$$

$$K = t_c \int_{V(x,y)} B^T \left(D_c + \frac{t_s}{t_c} D'_s \right) B dxdy \tag{7-38}$$

From the stress vector, the nodal force vector is calculated as:

$$F = F_{concrete} + F_{steel}$$

$$F = t_c \int_{V(x,y)} B^T \{\sigma_c\} dxdy + t_s \int_{V(x,y)} B^T \{\sigma_s\} dxdy$$

$$F = t_c \int_{V(x,y)} B^T \left(\{\sigma_c\} + \frac{t_s}{t_c} \{\sigma_s\} \right) dxdy \tag{7-39}$$

In general, we have two-direction reinforcing bars in a concrete element as is shown in Figure 7-11.

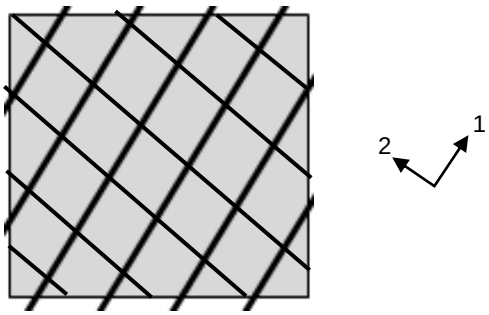

Figure 7-11 Two-direction smeared model

Similarly to Equations (7-38) and (7-39):

The stiffness matrix will be expressed as:

$$K = t_c \int_{V(x,y)} B^T \left(D_c + \frac{t_{s1}}{t_c} D'_{s,1} \frac{t_{s2}}{t_c} D'_{s,2} \right) B dxdy \tag{7-40}$$

And the nodal force vector is expressed as follows:

$$F = t_c \int_{V(x,y)} B^T \left(\{\sigma_c\} + \frac{t_{s1}}{t_c}\{\sigma_s\}_1 + \frac{t_{s2}}{t_c}\{\sigma_s\}_2 \right) dxdy \tag{7-41}$$

7.2.2 Menegotto-Pinto model

The Menegotto-Pinto model is adopted for the stress-strain relationship for reinforcing steel bars [1][34]. The envelope curve of the model is expressed as:

$$\sigma = R_s \varepsilon + \frac{(1 - R_s)\varepsilon}{(1 + \varepsilon^{R_b})^{1/R_b}} \tag{7-42}$$

$$\varepsilon = \frac{\varepsilon_s - \varepsilon_r}{\varepsilon_0 - \varepsilon_r} \tag{7-43}$$

$$\sigma = \frac{\sigma_s - \sigma_r}{\sigma_0 - \sigma_r} \tag{7-44}$$

$$R_s = \frac{E_{s2}}{E_s} \tag{7-45}$$

Where:

R_s: Strain stiffening factor.
R_b: Parameter for Baushinger effect.
E_s: Initial Young's modulus.
E_{s2}: Post yielding Young's modulus
σ_s, σ_s: Stress and strain at reversal point.
σ_0, ε_0: Stress and strain at intersection point between asymptotic lines.

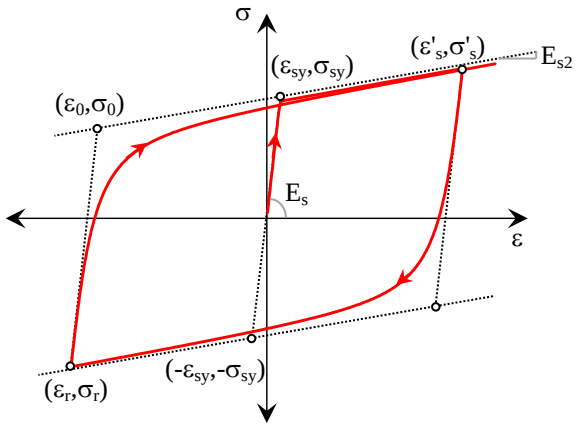

Figure 7-12 Menegotto-pinto model

Figure 7-12 shows the schematic representation of the Menegotto-Pinto model. This model uses two asymptotic lines to define the envelope curve, in which intersection as shown in Figure 7-13, defined by σ_0, ε_0 can be obtained from Equation (7-46).

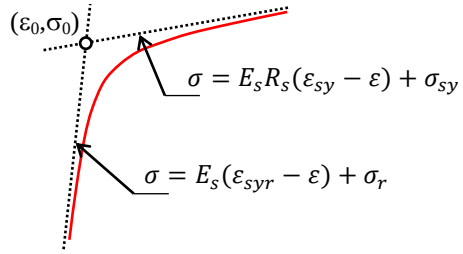

Figure 7-13 Asymptotic lines

$$\sigma_0 = E_s(\varepsilon_0 - \varepsilon_r) + \sigma_r$$

$$\varepsilon_0 = \begin{cases} \dfrac{\sigma_{sy} - \sigma_r + E_s(\varepsilon_r - R_s\varepsilon_{sy})}{E_s(1 - R_s)} & , \quad \dot{\varepsilon}_s \geq 0 \\ \dfrac{-\sigma_{sy} - \sigma_r + E_s(\varepsilon_r + R_s\varepsilon_{sy})}{E_s(1 - R_s)} & , \quad \dot{\varepsilon}_s < 0 \end{cases} \tag{7-46}$$

Where:

$\dot{\varepsilon}_s$: Strain increment.
$\sigma_{sy}, \varepsilon_{sy}$: Yielding stress and strain.

The parameter R_b can be obtained from:

$$R_b = R_{b0} - \frac{a_1\xi}{a_2 + \xi} \tag{7-47}$$

$$\xi = \frac{|\varepsilon_0 - \varepsilon'_r|}{\varepsilon_{sy}} \tag{7-48}$$

Where: $R_{b0} = 20$, $a_1 = 18.5$ and $a_2 = 0.15$ are usually adopted, and ξ is defined as the plastic strain ratio. In the calculation of ξ, in case of loading from elastic range to yielding range and loading in reversal direction, ε'_r is defined as follows:

$$\varepsilon'_r = \begin{cases} \varepsilon_{sy} & , \quad \dot{\varepsilon}_s \geq 0 \\ -\varepsilon_{sy} & , \quad \dot{\varepsilon}_s < 0 \end{cases} \tag{7-49}$$

7.3 Material model of CFS

CFS is considered to have a linear elastic behavior until it reaches the maximum tensile strength characteristic of the material, and then a brittle failure occurs suddenly as it was described in Section 2.1.3. (See Figure 7-14)

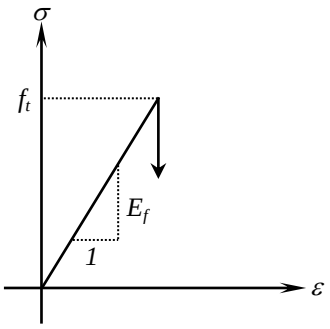

Figure 7-14 Linear-brittle model of CFS

7.4 Nonlinear finite element numerical simulation

7.4.1 STERA_FEM model

STERA_FEM Ver.3.3 [32] was used to carry out the numerical simulation. Figure 7-15 shows the element dimensions of specimens WF, RWF1 and RWF2 described in Section 4.1, defined by: X1=200mm, X2=240mm, X3=160mm, X4=300mm, Y1=200mm, Y2=250mm and Y3=300mm. Figure 7-16 shows the element dimensions of specimens WD, RWD1 and RWD2 described in Sections 4.2, defined by: X1=200mm, X2=300mm, Y1=190mm, Y2=215mm, Y3=2200mm, Y4=250mm and Y5=300mm. Also, Figure 7-15 and Figure 7-16 shows the boundary and loading conditions of the models, where B1 corresponds to a fix restrain in X and Y direction (Pin support), P1 and P2 represents the loading distribution in X-direction; and C is the control node for the load application.

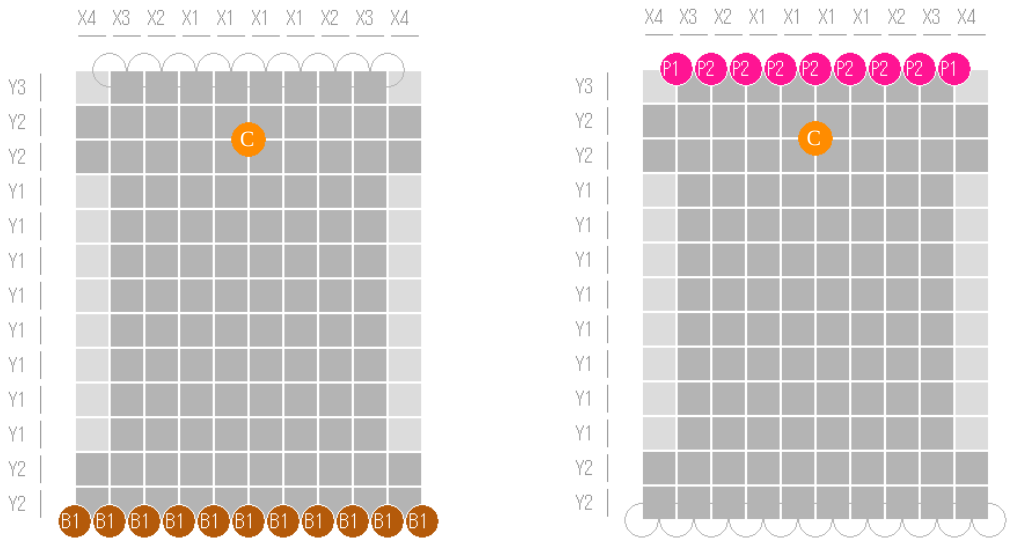

(a) Boundary Condition *(b) Loading Distribution*

Figure 7-15 Geometry, boundary and loading conditions (WF, RWF1 and RWF2)

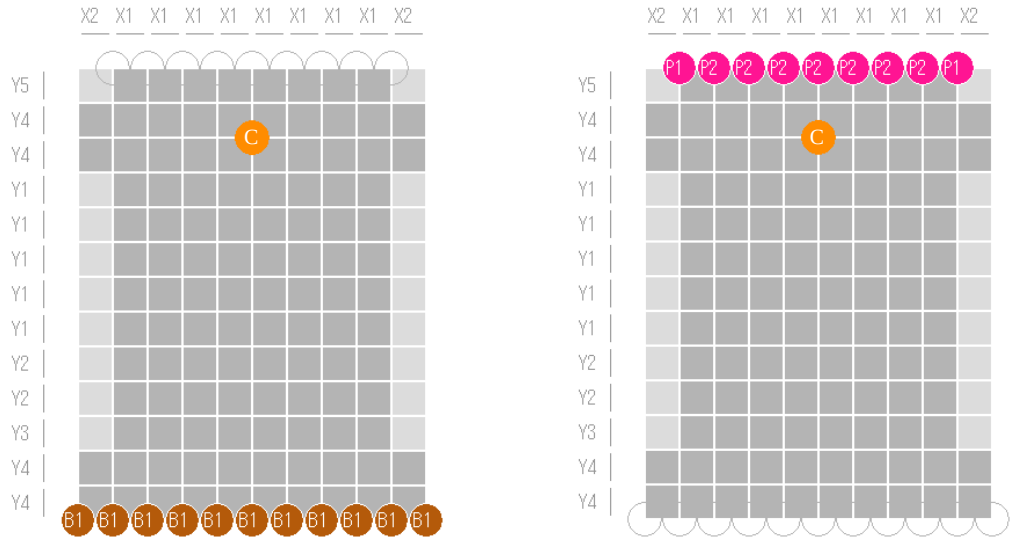

(a) Boundary Condition *(b) Loading Distribution*

Figure 7-16 Geometry, boundary and loading conditions (WD, RWD1 and RWD2)

The material types used in this model can be observed in Figure 7-17, where C1 and C2 correspond to the material properties of the concrete elements with 80mm and 700mm thickness respectively; and C3 is considered as a concrete type with high density to simulate the constant axial load and the additional moment applied during the test, as it is described in Sections 4.1 and 4.2. Moreover, the steel material S1 corresponds to the wire mesh used in the whole wall span, S2 corresponds to the additional longitudinal reinforcing bars at the boundary ends of the wall and S3 corresponds to the reinforcement of the footing and the upper beam.

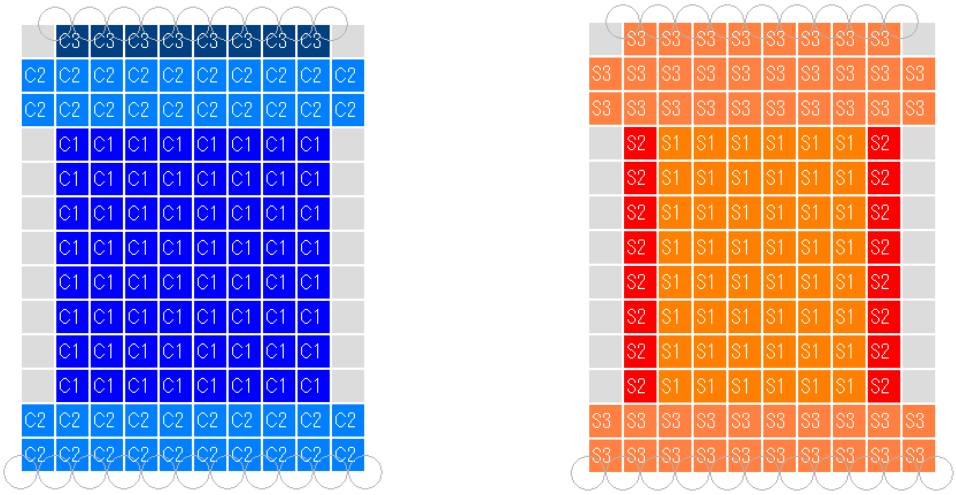

(a) Concrete Material *(b) Steel Material*

Figure 7-17 Material types model

LDRC shear walls retrofitted with full height of CFS is shown in Figure 7-18. Where F1 corresponds to the material properties of the CFS used in specimens RWF1 and RWF2, which are described in Section 4.1. This element is oriented in X-direction only.

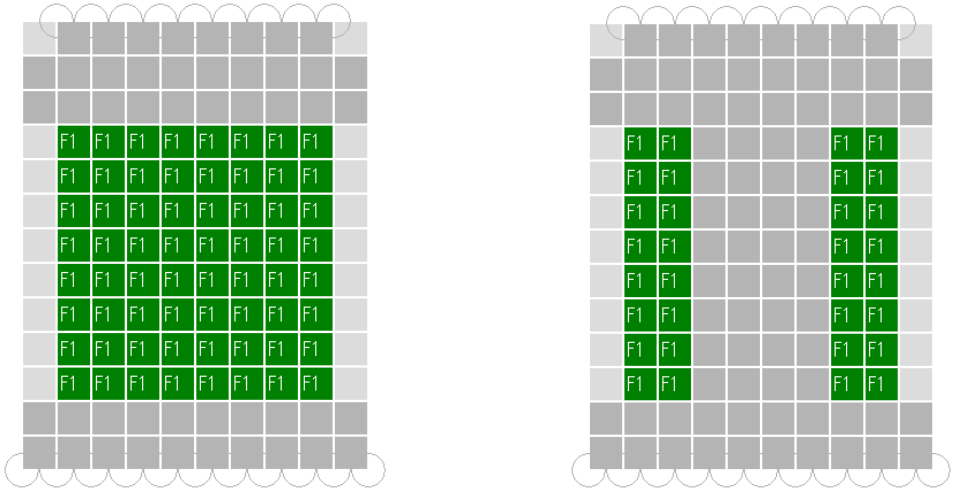

(a) RWF1 *(b) RWF2*

Figure 7-18 CFS retrofitting (RWF1 and RWF2)

LDRC shear walls retrofitted with full height of CFS is shown in Figure 7-19. Where F1 corresponds to the material properties of the CFS used in specimens RWD1 and RWD2, which are described in Section 4.2. This element is oriented in X-direction only.

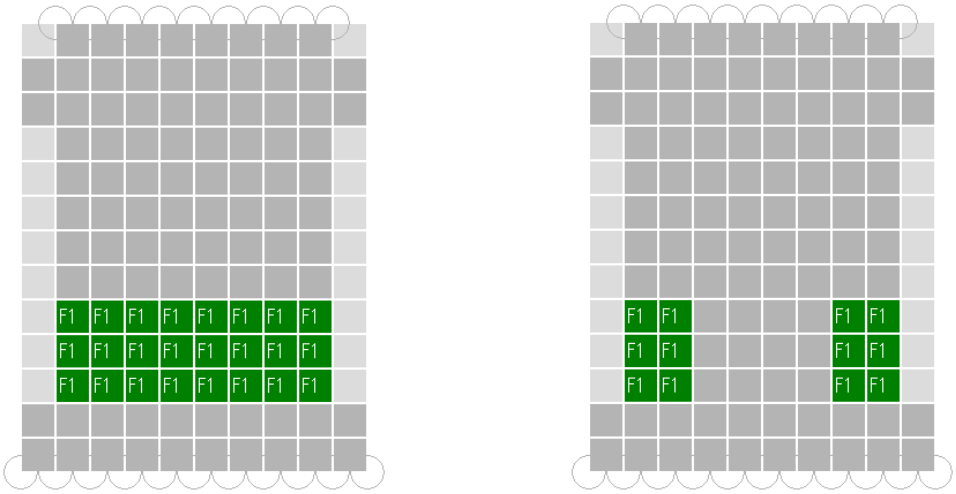

(a) RWD1 *(b) RWD2*

Figure 7-19 CFS retrofitting (RWD1 and RWD2)

7.4.1 Experimental wall test vs. numerical simulation

The numerical analysis conducted by using STERA_FEM was a pushover analysis until the strain deformation corresponding to the maximum strength capacity of each specimen.

7.4.1.1 WF, RWF1 and RWF2

Figure 7-20 shows the deform shape of the model under a pushover analysis for each specimen tested. Besides it can be observed the orientation and magnitude of the stress in each Gaussian point of the elements.

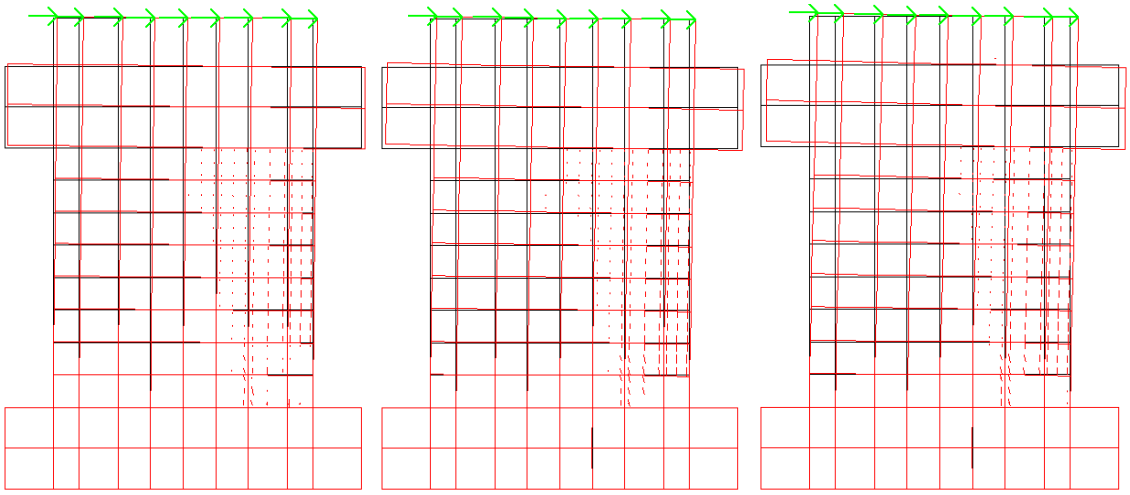

(a) WF *(b) RWF1* *(a) RWF2*

Figure 7-20 Deform shape (WF, RWF1 and RWF2)

The comparison between the experimental envelope curve and the pushover analysis carried out for specimens WF, RWF1 and RWF2 are shown in Figure 7-21, Figure 7-22 and Figure 7-23 respectively. The pushover analysis was conducted up to the strain at maximum strength of each specimen due to the lack to model the strength degradation.

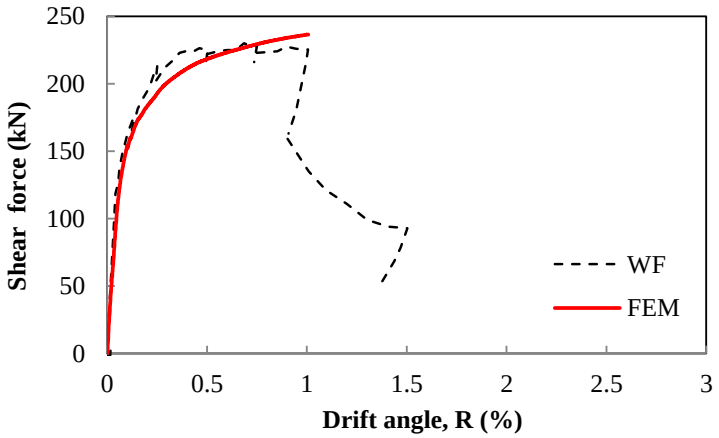

Figure 7-21 Experimental envelope curve WF vs. FEM analysis

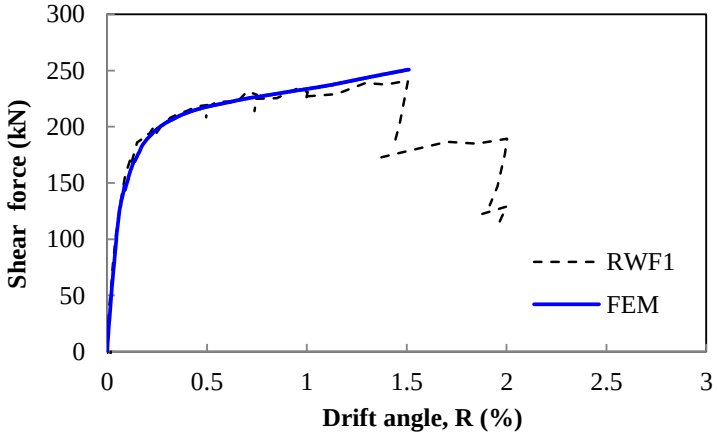

Figure 7-22 Experimental envelope curve RWF1 vs. FEM analysis

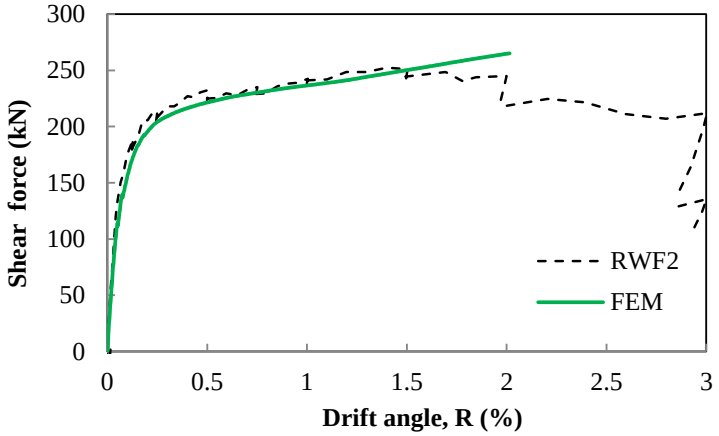

Figure 7-23 Experimental envelope curve RWF2 vs. FEM analysis

As it is described in Section 4.1.4, the envelope curve of the three specimens tested under pushover analysis remains about the same strength level (See Figure 7-24). Although the deformation capacity of the specimens got improved due to the retrofitting by CFS, from the analysis conducted, it cannot be confirmed due to STRERA_FEM is under development.

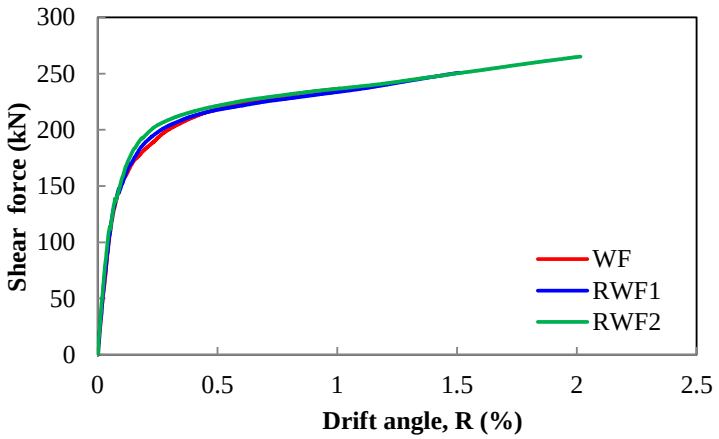

Figure 7-24 Comparison of the envelope curves (WF, RWF1 and RWF2)

7.4.1.2 WD, RWD1 and RWD2

Figure 7-25 shows the deform shape of the model under a pushover analysis for each specimen tested. Besides it can be observed the orientation and magnitude of the stress in each Gaussian point of the elements.

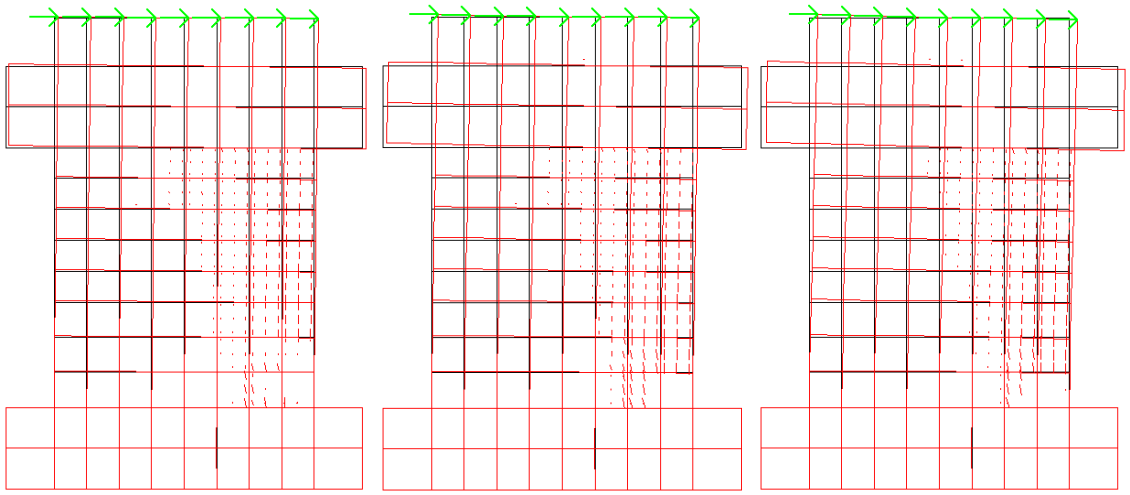

(a) WD *(b) RWD1* *(a) RWD2*

Figure 7-25 Deform shape (WD, RWD1 and RWD2)

The comparison between the experimental envelope curve and the pushover analysis carried out for specimens WD, RWD1 and RWD2 are shown in Figure 7-26, Figure 7-27 and Figure 7-28 respectively. The pushover analysis was conducted up to the strain at maximum strength of each specimen due to the lack to model the strength degradation.

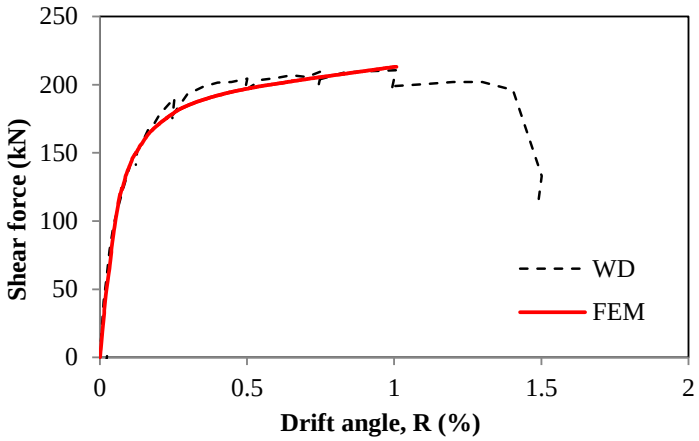

Figure 7-26 Experimental envelope curve WD vs. FEM analysis

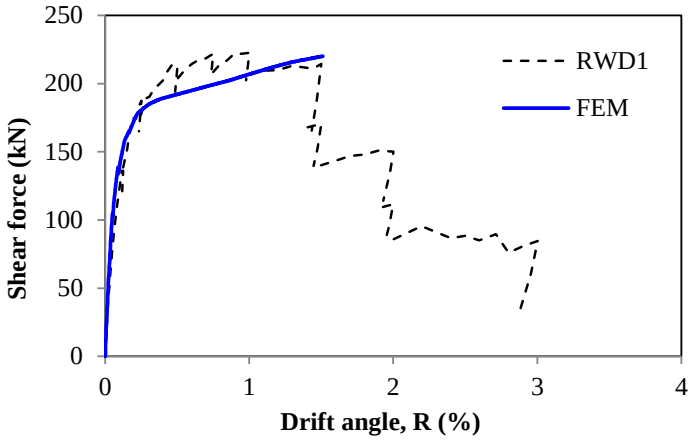

Figure 7-27 Experimental envelope curve RWD1 vs. FEM analysis

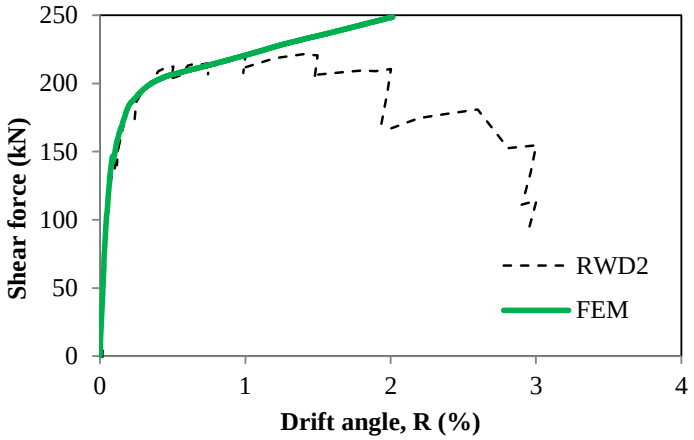

Figure 7-28 Experimental envelope curve RWD2 vs. FEM analysis

As it is described in Section 4.2.4, the envelope curve of the three specimens tested under pushover analysis remains about the same strength level (See Figure 7-29). Although the deformation capacity of the specimens got improved due to the retrofitting by CFS, from the analysis conducted, it cannot be confirmed due to STRERA_FEM is under development.

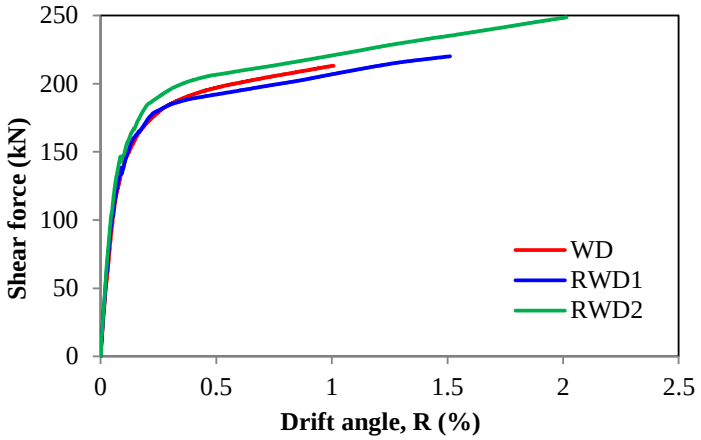

Figure 7-29 Comparison of the envelope curves (WD, RWD1 and RWD2)

CHAPTER 8

CONCLUSIONS AND RECOMMENDATIONS

CHAPTER 8 : CONCLUSIONS AND RECOMMENDATIONS

8.1 Conclusions

This investigation was conducted to assess the performance of low ductility reinforced concrete (LDRC) shear walls retrofitted by carbon fiber sheet (CFS) under cyclic loading. Two verification tests were conducted on LDRC wall retrofitted with CFS. From the test results, it can be verified that CFS improves the deformation capacity of the wall under cyclic loading, by delaying the crushing of the concrete at the base of the wall. Moreover, LDRC wall retrofitted with CFS does not have influence in the shear strength capacity of the wall, therefore the strength of remains about the same level as the non-retrofitted wall as it was expected. Degradation of the post-maximum strength was more gradual for both, LDRC wall retrofitted at the wall ends with full height and partial height of CFS. Ultimate limit deformation of both specimens, LDRC wall retrofitted at the wall ends with full height and partial height of CFS was larger than the specimens with CFS retrofitting along the wall span.

During the failure mode of the non-retrofitted walls, crushing of the concrete at the wall base corner of the wall and buckling of the steel occurs; so the wall fails in flexural mode as it was expected. Besides, LDRC wall retrofitted with full height of CFS and LDRC wall retrofitted with partial height of CFS also fails in flexural mode and shows a swelling at the base corners on the wall, as well as the sudden failure of the CFS, once the specimen cannot sustain the applied load. Therefore a third experimental test was conducted in order to study the confinement effect of concrete retrofitted by CFS.

The third experimental test was conducted over circular, square and rectangular shaped specimens retrofitted by CFS under compressive monotonic and cyclic loading. From the test results, stress on the CFS in circular shaped specimens is distributed similarly on the CFS, while for square and rectangular shaped specimens the stress on the CFS is concentrated at corners. Therefore it was observed that circular shaped specimens retrofitted with CFS improve its maximum strength. On the other hand, CFS helps to improve the deformation capacity of the circular, square and rectangular shaped specimens under monotonic and cyclic loading. In other words, the ductility and energy dissipation of concrete retrofitted with CFS is improved in comparison with the non-retrofitted samples. For square and rectangular shaped specimens, a larger chamfer radius helps to improve the maximum strain and the maximum strain of the specimens retrofitted with CFS is proportional to the ultimate strain of the CFS.

Two stress-strain relationship of concrete retrofitted by CFS were studied. Although Lam and Teng's and Nakatsuka's model gives a similar approach for circular shaped concrete con-fined with CFS, Lam and Teng's model does not give a good approach for square shaped concrete confined with CFS because the model uses only one slope after transition point, therefore it cannot reproduce the strength reduction. On the other hand, Nakatsuka's model provides a model for square shaped concrete with chamfer radius of 30mm. This model uses a two-slope model which can be used to model the strength reduction of the experimental results. Since the square and rectangular shaped specimens tested have a chamfer radius of 15mm, shaped coefficients must be modified.

Proposed modified Nakatsuka's model takes into consideration the chamfer radius and the ratio of effective area of confined concrete. From the analytical results, proposed modified Nakatsuka's model gives a better approach of the experimental envelope curves for circular and square shaped specimens retrofitted with CFS. Moreover, a stress-strain relationship for concrete with or without CFS confinement under cyclic loading was proposed, this model is based on Modified Darwin & Pecknold, Noguchi, Naganuma, Lam & Teng and Nakatsuka's Model. Proposed model gives a good approach in comparison with the experimental results of circular and square shaped specimens under cyclic.

As part of this investigation, a nonlinear finite element method was studied in order to develop STERA_FEM software, and to conduct a comparison with the experimental results. STERA_FEM takes into consideration: 4 nodes isoparametric planar element, incompatible element, 9 Gaussian points, the proposed model for concrete with or without CFS confinement, equivalent uniaxial strain of concrete for each principal direction considering the bi-axial stress-strain relationship of concrete by using the maximum stress surface of concrete, smeared crack model with the Menegotto-Pinto hysteresis model for reinforcing steel and an elastic-brittle model for CFS.

Finally, a pushover analysis were conducted and compared with the experimental results of the six walls (retrofitted with CFS and non-retrofitted). The analytical curves show a good approach in comparison with the experimental curves.

8.2 Recommendations

Based on the experiments, When using bolts for fixing the CFS to the concrete, even though it does not have an important contribution in terms of maximum stress, it must be very careful that the steel plates used to fix the CFS does not provide axial force in the direction of the applied load.

Further studies on the shape coefficients for circular, square and rectangular shaped are suggested to improve the non-linear hysteresis of concrete retrofitted with CFS, by increasing the data with a large range of concrete types, using different amount of CFS as a confinement method and considering effective confinement ratio of the section

Although the deformation capacity of the walls got improved due to the retrofitting by CFS as it is reported during the test, from the analysis conducted, it cannot be confirmed due to STRERA_FEM is under development. STERA_FEM works under compression-tension cyclic loading, giving a good approach as it was presented in this investigation, but not in case of lateral reversal loading. Therefore, further research is needed to improve STERA_FEM to consider the strength reduction and lateral reversal loading.

Finally, it is recommended to conduct further researches considering the bond mechanism between the reinforcing steel bars and concrete as well as between concrete and CFS.

REFERENCES

[1] Abanesi, T. and Nuti, C., "Reinforcing steel bar model", 2007.

[2] ACI 440.2R-08, *Guide for the design and construction of externally bonded FRP systems for strengthening concrete structures*, American Concrete Institute, 2008.

[3] Aktan, A., Karlsson, B.I. and Sozen, M.A., *Stress-strain relationships of reinforcing bars subjected to large strain reversals*, Report SRS No. 397, Civil Engineering Studies, University of Illinois, Urbana-Champaign, Illinois, 1973.

[4] Bathe, K.J., *Finite element procedures*, Klaus-Jurgen Bathe, 2006.

[5] Benzaid, R. and Mesbah, H.A., "Circular and square concrete columns externally confined by CFRP composite: Experimental investigation and effective strength models", INTECH, pp. 167-201, 2013.

[6] Cervanka, V., *Inelastic finite element analysis of reinforced concrete panels under in-plane loads*, Ph.D. Thesis, University of Colorado, Boulder, Colorado, 1970.

[7] Collins, M.P. and Mitchell, D., *Prestressed concrete structures*, Prentice-Hall, New Jersey, 1991.

[8] Cook, R.D., *Concepts and applications of finite element analysis*, John Wiley & Sons, 2007.

[9] Darwin, D. and Pecknold, D.A.W., *Inelastic model for cyclic biaxial loading of reinforced concrete*, Report SRS-409, Civil Engineering Studies, University of Illinois, Urbana-Champaign, Illinois, 1974.

[10] Hognestad E.A., *A study of combined bending and axial load in reinforced concrete members*, Bulletin No. 399, University of Illinois, Engineering Experiment Station, 1951.

[11] Hristovski, V. and Noguchi, H., "FEM progressive failure simulation of reinforced concrete members on shear", *Proceedings of Japan Concrete Institute Annual Convention*, Vol. 24, No. 2, 2002.

[12] Karsan, I.D. and Jirsa, J.O., "Behavior of concrete under compressive loadings", *Journal of the Structural Division*, ASCE, Vol. 95, No. ST12, 1969.

[13] Kawai, H., *Finite Element analysis of Reinforced concrete wall without boundary column retrofitted by carbon fiber sheet*, Master Thesis, Toyohashi University of Technology, Toyohashi, Japan, 2014, in Japanese.

[14] Kupfer, H. and Grestle, K.H., "Behavior of concrete under biaxial stresses", *Journal of the Engineering Mechanics Division*, Vol. 99, No. 4, pp. 853-866, 1973.

[15] Kupfer, H., Hilsdorf, H.K. and Rusch, H., "Behavior of concrete under biaxial stresses", *Journal ACI*, Proc. Vol. 66, No. 8, pp.656-666, 1969.

[16] Lam, L. and Teng, J.G., "Design-oriented stress–strain model for FRP-confined concrete", *Construction and Building Materials*, Vol. 17, No. 6, pp. 471-489, 2003.

[17] Lam, L. and Teng, J.G., "Design-oriented stress–strain model for FRP-confined concrete in rectangular columns", *Journal of Reinforced Plastics and Composites*, Vol. 22, No. 12, pp. 1149-1186, 2003.

[18] Lam, L. and Teng, J.G., "Stress-strain model for FRP-confined concrete under cyclic axial compression", *Engineering Structures*, Vol. 31, No. 2, pp. 308-321, 2009.

[19] Maekawa, K., Okamura, H. and Pimanmas, A., *Non-linear mechanics of reinforced concrete*, CRC Press, 2003.

[20] Matsui, T., Saito, T. and Reyna, R., "Basic study on reinforced concrete shear walls without boundary columns retrofitted by carbon fiber sheets", *Journal of Disaster Research*, Vol. 9, No. 6, pp. 1008-1014, 2014.

[21] Matsui, T. and Saito, T., "Structural performance of rectangular reinforced concrete walls retrofitted by carbon fiber sheets", Technical Paper No. 0004, *Proceedings of 16th World Conference on Earthquake Engineering*, Santiago, Chile, 2017.

[22] Naganuma, K., Yonezawa, K., Kurimoto, O. and Eto, H., "Simulation of nonlinear dynamic response of reinforced concrete scaled model using three-dimensional finite element method", Technical Paper No. 586, *Proceedings of 13th World Conference on Earthquake Engineering*, Vancouver, B.C., Canada, 2004.

[23] Nakatsuka, T., Kenichi, K. and Kinya, T., "Stress-strain characteristics of confined concrete with carbon fiber sheet", *Concrete Research and Technology*, Vol. 9, No. 2, pp. 65-78, 1998, in Japanese.

[24] Nelissen, L.J.M., "Biaxial testing of normal concrete", *Heron*, Netherlands, Vol. 18, No. 1, 1972.

[25] Noguchi, H. and Kashiwazaki, T., "FEM analysis of structural performance deterioration of RC elements subjected to seismic reversed cyclic shear", Technical Paper No. 672, *Proceedings of 13th world Conference on Earthquake Engineering*, Vancouver, B.C., Canada, 2004.

[26] Palermo, D. and Vecchio, F.J., "Compression field modeling of reinforced concrete subjected to reversed loading: Formulation", *ACI Structural Journal*, Vol. 100, No. 5 pp. 616-625, 2003.

[27] Reyna, R., Saito, T., Matsui, T. and Hayashi, K., "Confinement effect of concrete with carbon fiber sheet reinforcement under monotonic loading". *International Journal of Structural and Civil Engineering Research*, Vol. 5, No. 4, pp. 250-257, 2016.

[28] Reyna, R., Saito, T., Matsui, T. and Hayashi, K., "Monotonic stress-strain relationship of concrete with carbon fiber sheet confinement", Technical Paper No. 6029, *Proceedings of Japan Concrete Institute Annual Convention*, Hakata, Japan, 2016.

[29] Reyna, R., Saito, T., Matsui, T. and Hayashi, K., "Stress-strain relationship of concrete retrofitted with carbon fiber sheet under cyclic loading", Technical Paper No. 1796, *Proceedings of 16th World Conference on Earthquake Engineering*, Santiago, Chile, 2017.

[30] Saenz, L.P., "Discussion of equation for the stress-strain curve of concrete by Desayi and Krishman", *ACI Journal*, Vol. 61, pp. 1229-1235, 1964.

[31] Saito, T., *STERA_FEM Technical Manual*, 2016.
http://www.rc.ace.tut.ac.jp/saito/software-e.html.

[32] Saito, T., *STERA_FEM User Manual*, 2016.
http://www.rc.ace.tut.ac.jp/saito/software-e.html.

[33] Sakai, J. and Kawashima, K., "An unloading and reloading stress-strain model for concrete confined by tie reinforcements", *Proceedings of 12th World Conference on Earthquake Engineering*, pp. 1431-2000, 2000.

[34] Sakai, J. and Kawashima, K., "Modification of the Giuffre, Menegotto and Pinto model for unloading and reloading paths with small variations", *Proceedings of Japan Society of Civil Engineers*, pp. 159-170, 2003.

[35] Sakai, T., *Performance verification and material model of concrete confined by carbon fiber sheet*, Master Thesis, Toyohashi University of Technology, Toyohashi, Japan, 2016, in Japanese.

[36] Shima, H., *Micro and macro models for bond behavior in reinforced concrete*, Doctoral Dissertation, University of Tokyo, Japan, 1986

[37] Sima, J.F., Roca, P. and Molins, C., "Cyclic constitutive model for concrete", *Journal Engineering Structures*, Vol. 30, No. 3, pp. 695-706, 2008.

[38] Singh, A., Grestle, K.H. and Tulin, L.G., "The behavior of reinforcing steel under reversed loading", *Material Research and Standards*, ASTM, Vol. 5, No. 1, pp. 12-17, 1965.

[39] Sinha, B.P., Grestle, K.H. and Tulin, L.G., "Sress-strain relations for concrete under cyclic loading", *Journal ACI*, Proc. Vol. 61, No.2, pp. 195-211, 1964.

[40] Uchimura, K., *Deformation capacity of RC wall without boundary columns retrofitted by carbon fiber sheets*, Master Thesis, Toyohashi University of Technology, Toyohashi, Japan, 2014, in Japanese.

[41] Vecchio, F.J. and Collins, M.P., "The modified compression-field theory for reinforced concrete elements subjected to shear", *ACI Journal*, Vol. 83, No. 2, pp. 219-231, 1986.

[42] Yuzugullu, O. and Schonobrich, W.C., "A numerical procedure for the determination of the behavior of a shear wall frame system", *Journal ACI*, Proc. Vol. 70, No. 7, pp. 474-479, 1973.

[43] Zavala, C., et al., "Cyclic behavior of low ductility walls considering perpendicular action", *Journal of Disaster Research*, Vol. 8, No. 6, pp. 312-319, 2013.